5-5-2018

Near Field Mixing Characteristics of a Variable Density Non-Reacting Jet in a Hot Vitiated Crossflow

Kyle T. Linevitch Jr
University of Connecticut, linevitchjr.k@aol.com

Near Field Mixing Characteristics of a Variable Density Non-Reacting Jet in a Hot Vitiated Crossflow

Kyle T. Linevitch Jr.

B.S., University of Connecticut, 2016

A Thesis

Submitted in Partial Fulfillment of the

Requirements for the Degree of

Master of Science

At the

University of Connecticut

2018

APPROVAL PAGE

Master of Science Thesis

Near Field Mixing Characteristics of a Variable Density Non-Reacting Jet in a Hot Vitiated Crossflow

Presented by:

Kyle T. Linevitch Jr., B.S.

Major Advisor_____

Dr. Baki M. Cetegen

Associate Advisor_____

Dr. Claudio Bruno

Associate Advisor_____

Dr. Xinyu Zhao

University of Connecticut

2018

Acknowledgements

I would first like to thank Prof. Baki Cetegen for providing me with the opportunity to work with him to complete my thesis research. It has been a great privilege to have been provided with the guidance and insight of such a prestigious researcher. I would like to thank Prof. Jackie Sung for generously loaning several key pieces of lab equipment, without which this thesis could not be completed. I would also like to thank Prof. Claudio Bruno and Prof. Xinyu Zhao for their support as my advisory committee members.

I would like to thank my fellow experimentalist, James, for the unprecedented amount of guidance over these past two years. Most of the knowledge I have gained of setting-up and performing combustion research experiments and data analysis has come from our time together in the lab. You have also taught me the wonders of getting great deals on eBay and the secrets to saving big when couch shopping. I would also like to thank past and present lab members, Bikram and Rishi, for their help and input in performing multiple experiments, which helped made this thesis possible.

I would like to thank Pete and Mark of the school of engineering machine shop for their time and dedication to teaching me how to properly machine vital experimental apparatus. I would like to thank the department administrative staff, Tina, Laurie, Kelly, and Elizabeth for making sure all materials were ordered and received on time and for taking care of all administrative tasks.

Most important of all, I would like to thank my wife, Megan, and our daughter, Juliette, for their constant support, patience, and love throughout this endeavor. You are the source of my inspiration and without you I would have never completed this work.

Table of Contents

List of Tables

List of Figures

Abstract

The mixing characteristics in the “extreme” near field of a non-reacting jet in crossflow were experimentally investigated in an environment relevant to gas turbine combustors. A turbulent jet was injected into a hot vitiated crossflow of combustion products at 1500K. Different jet-to-crossflow momentum flux ratios and jet-to-crossflow density ratios were studied using three different jet exit velocity profiles; a fully developed turbulent pipe flow with 4% turbulence intensity (TI), a top-hat flow with 8% TI, and a turbulent pipe-like flow with 40% TI. Center-plane scalar mixing of the jet and crossflow were investigated using measured temperature fields from planar laser Rayleigh scattering. Jet trajectory, centerline concentration decay, scalar dissipation and mixing time scales were determined as a function of the above-mentioned jet parameters to characterize the jet-crossflow mixing characteristics.

The observed center-plane mixing metrics indicated that better near field mixing was exhibited for lower values of the momentum flux ratio and larger values of density ratio. As the momentum flux ratio increased, windward and leeward mixing decreased. The magnitude of scalar dissipation in the windward region decreased as the momentum flux increased, while the leeward dissipation region increased in size and magnitude as momentum flux ratio increased. When the density ratio was decreased, both the windward and leeward dissipation regions reduced in size and magnitude. The top-hat and turbulent pipe jet exit velocity profiles displayed similar mixing characteristics while the 40% TI profile exhibited deeper jet penetration, slower centerline concentration decay rates, and lower scalar dissipation.

1. Introduction

1.1 Background

A jet in crossflow (JICF), also referred to as a transverse jet, is a flow field in which fluid is ejected from a jet into a crossflowing fluid, as depicted in Fig. 1.1. Applications of JICF flow fields range from the injection of gas into a gas, the injection of a liquid into a liquid, or the injection of a liquid into a gas. Real-word examples of a JICF flow field include the primary air and dilution air injection in gas turbine combustors, gas turbine blade film cooling, fluidic thrust vectoring in gas turbine and rocket engines, plume dispersal, and liquid disposal in streams [1].

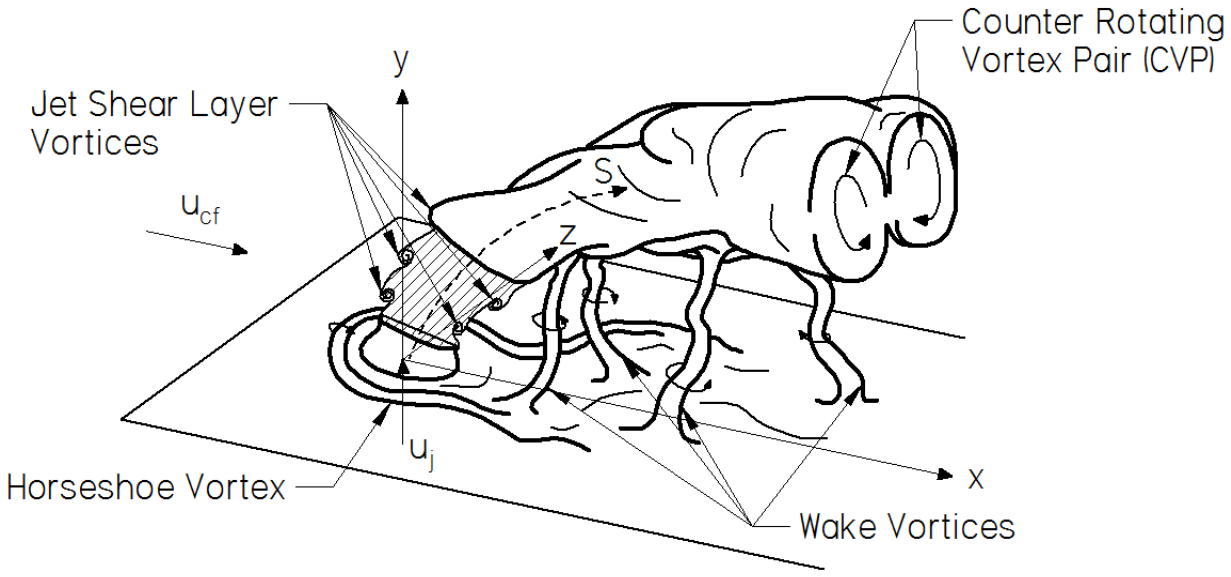

Fig. 1.1: 3D-drawing of the main vortical structures of a JICF, adapted from [2].

With such a variety of applications, involving reacting and non-reacting systems, the flow dynamics and mixing characteristics of a JICF have been, and continue to be investigated. The behaviors observed are often characterized using a non-dimensional parameter such as the jet-to-crossflow density ratio, s, velocity ratio, r, or momentum flux ratio J; mathematically defined in

Eqs. (1.1) - (1.3) where ρ_j is the jet density, ρ_{cf} is the crossflow density, u_j is the mean jet velocity, and u_{cf} is the mean crossflow velocity.

$$s = \frac{\rho_j}{\rho_{cf}} \tag{1.1}$$

$$r = \frac{u_j}{u_{cf}} \tag{1.2}$$

$$J = sr^2 = \frac{\rho_j u_j^2}{\rho_{cf} u_{cf}^2} \tag{1.3}$$

The remainder of the introduction includes a brief review of previous JICF studies (Section 1.2), focusing on the vortical structures (Section 1.2.1) and mixing characteristics (Section 1.2.2), as well as providing the motivation and objectives of the current research (Section 1.3).

1.2 Previous JICF Studies

1.2.1 Vortical Structures of a JICF

In the past several decades, the structures of non-reacting JICF flow fields have been studied extensively. The most referenced JICF research is that of Fric and Roshko [2], in which the main vortical structures of a JICF are described. As shown in Fig. 1.1, there are four main vortical structures associated with the interaction of a jet and crossflow: jet shear layer vortices, horseshoe vortices, wake vortices, and the counter rotating vortex pair (CVP) [2]. The jet shear layer vortices are attributed to the Kelvin-Helmholtz instability at the edge of the jet orifice and are found mainly on the windward jet-crossflow boundary, but also on the leeward jet edge [2]. The horseshoe vortices are formed upstream of the jet due to an adverse pressure gradient as a result of the jet acting as an obstacle to the crossflow, similar to the results of flow over a cylinder. The vortex system propagates downstream, wrapping around the jet, and forming the

horseshoe appearance [2]. The wake vortices are viewed as tornado-like structures downstream of the jet and are attributed to the separation of the crossflow boundary layer. These structures are formed by "separation events" that occur alternately on each side of the jet and propagate downstream, stretching and engulfing more of the crossflow boundary layer [2]. The CVP is formed as a result of the jet impulse on the crossflow. The formation begins in the near field, and continues to grow downstream, becoming the dominant mixing mechanism in the far field [2].

In theory, a JICF should be symmetric about the center-plane, especially when considering a round jet into a uniform crossflow. This concept is used in computational studies, such as in [3] where the DNS results of Muppidi & Mahesh show symmetry about the jet center-plane. However, in experimental studies, asymmetry has been observed. Smith & Mungal [4] observed asymmetric jet concentrations in downstream cross-sectional images that increased in asymmetry as velocity ratio, r, increased. These observations were noted to be possibly machining related, with the idea that machining tolerances could cause small experimental imperfections leading to asymmetric conditions. In the work of Gevorkyan [5], extensive measures were attempted to reduce possible experimental flaws to reduce asymmetry including flow straighteners, increased jet inlet lengths, and the use of a four-way injection system with the ability to be rotated, however no drastic change in asymmetry was observed. In [5], symmetric conditions were only observed for momentum flux ratios, $J \leq 8$ for flush jet injectors. Similar to [4], with increasing velocity ratio, r, asymmetry became more pronounced in [5], and for a constant value of J, as the density ratio, s decreased, the jet cross-section became more symmetric. Gevorkyan concluded that the jet asymmetry is related to unstable jet shear layers and rapid shear layer rollups, as well as a tertiary vortical structure below the main jet structure.

1.2.2 Mixing Characteristics of a JICF

With the majority of JICF applications being mixing related, the mixing characteristics of a JICF are at the center of most studies. These characteristics are most often investigated in the x-y plane (jet center plane) of Fig. 1.1, but are also investigated in the y-z plane in the far field or in the x-z plane in the near field. The x-y plane is used to characterize jet centerline trends including, but not limited to, trajectory and concentration decay. The y-z and x-z plane investigations look at downstream cross-sections of the jet and are regularly used to characterize the asymmetry of the jet and create probability density functions (PDFs) of jet concentration to quantify far field mixing.

1.2.2.1 Jet Centerline Trajectory

One of the most common mixing characteristics investigated in a JICF flow field is the jet centerline trajectory, with the objective of developing a general correlation between trajectory and flow parameters. The correlation most often used is of the form:

$$\frac{y}{d} = Ar^n \left(\frac{x}{d}\right)^m \tag{1.4}$$

where A, n, and m are experimentally or computationally determined constants, and d is the jet exit diameter. A list of some of these constants can be found in [1]. The length scale used in Eq. (1.4) does not rely on flow parameters and therefore numerous researchers have studied jet centerline trajectories in hopes of determining correlations based on more relevant length scales that include flow parameters, such as rd, r^2d, or $\sqrt{J}d$. The relevance of the use of different length scales has been found to be dependent on the definition of the jet centerline. For instance, Smith & Mungal [4] found that for a jet centerline defined based on concentration, trajectories collapse better with the length scale rd:

$$\frac{y}{rd} = A\left(\frac{x}{rd}\right)^{m} \tag{1.5}$$

where A = 1.5 and m = 0.27 for $5 \leq r \leq 25$ ($25 \leq J \leq 625$, s = 1.0) up to a distance of 5 rd [4], while Keffer & Baines [6] found that trajectories based on a jet centerline streamline collapse better with a scale of r^2d for $6 \leq r \leq 10$ ($36 \leq J \leq 100$, s = 1.0) up to a distance of 4 rd. Similar to [6], but for larger values of s, Wagner found that trajectories based on a jet streamline collapse better using scaling values of $\sqrt{J}d$ and $\frac{J^C}{d}$:

$$\frac{y}{\sqrt{J}d} = A\left[\frac{\left(\frac{xJ^C}{d}\right)^{B}}{\left(\frac{xJ^C}{d}\right)^{B} + E}\right] \tag{1.6}$$

where A = 1.69, B = 0.74, C = -0.015, and E = 1.2 for $5.2 \leq J \leq 22.7$ ($1.0 \leq r \leq 2.1$, s = 5.1). Building upon these scaling laws, using direct numerical simulation (DNS) results Muppidi & Mahesh [3] found that the jet trajectory scaled with rd also depends on another length scale, h which is defined as the height at which the jet remains vertical in the crossflow. This length scale was introduced by the observation that the boundary layers of both the jet and the crossflow affect the jet trajectory.

1.2.2.2 Jet Centerline Concentration Decay

Another commonly investigated centerline mixing metric is the jet centerline concentration decay, where a faster decay indicates better mixing. For an equidensity JICF (s = 1.0), Smith & Mungal [4] found that the jet concentration decayed exponentially in the centerline coordinate system, S, in both the near field and far field, but at different rates. The near field was found to decay at a rate of $S^{-1.3}$ while the far field decayed at a rate of $S^{-2/3}$, where the branching point depended on r. These results were observed for $5 \leq r \leq 25$ ($25 \leq J \leq 625$, s =

1.0) with a top-hat velocity profile associated with a flush nozzle jet. Su & Mungal [7] found that the concentration decayed at a rate of S^{-1} (the same rate as a free jet) in the near field and at an increased rate in the far field with a branching point at approximately S/rd = 2.5. These results were observed at a single velocity ratio, r = 5.7, for an assumed pipe profile (the velocity profile at the jet exit was not measured in their study) of a flush and elevated jet. The results of Su & Mungal are interesting in the sense that no effects of the crossflow boundary layer were observed, which contradict the findings in [3]. Gevorkyan et al. [8] bridged the gap between [4] & [7] by performing experiments using a flush nozzle, elevated nozzle, and flush pipe jet with $2.2 \leq r \leq 6.4$ ($5 \leq J \leq 41$, s = 1.0). Similar to [4], with a flush nozzle, [8] observed faster decay rates in the near field with branching to slower decay rates in the far field for $r > 5$, however the near field decayed faster in [8] compared to [4], with relatively similar decays in the far field starting at roughly the same branch point, S/rd = 0.3 in [4] and S/rd = 0.33 in [8]. For lower values of r with a flush nozzle, Gevorkyan et.al. found that the decay rate scaled between $S^{-1.3}$ and S^{-1}, with values of r = 5 & 8 being closer to S^{-1}. For an elevated nozzle, Gevorkyan found the decay rates to also be between $S^{-1.3}$ and S^{-1}, with the majority of cases being closer to S^{-1}. Unlike in [7], with a flush pipe, [8] observed faster decay rates scaling between $S^{-1.6}$ and $S^{-1.3}$, with faster decay rates being associated with larger values of r. Gevorkyan et.al. extended the evaluation of jet centerline decay of a flush nozzle to cases with lower density ratios. They observed that for $J \geq 12$ the jet core length decreased as s decreased, while for J = 5, the core length was independent of s. They also found that for J = 5, as s decreased the decay rate also decreased, while for J = 41, as s decreased the decay rate increased in the near field and branched to a slower decay in the far field.

1.3 Current Research Objectives

Much of the JICF research in the past several decades have focused on the mixing characteristics of equidensity (s = 1.0) flow fields such as in [4] - [7]. More recently, researchers have extended JICF studies to lower values of s such as in [8], where experiments were performed using a heated jet to obtain s = 0.35 & 0.55. Along with this, the majority of presented findings are within large viewing windows, up to 70 d × 70 d in [4] and down to 15 d ×15 d in [8], with large wind tunnels being used as the crossflow. In relation to real-world applications, the previous studies mentioned are more related to plume dispersion for pollution control, where far field characteristics are of most importance and jet temperatures are typically greater than the crossflow resulting in $s \leq 1$. However, for gas turbine applications, such as dilution air, crossflow temperatures exceed that of the jet, with crossflow temperatures on the order of 1500K resulting in $s > 1$. Gas turbine combustors are also much more confined than the large wind tunnels used in [4], [6] & [7], with shorter downstream distances, similar to that in [8]. While the test section used in [8] is more relevant dimensionally to a gas turbine combustor, the large viewing window has similar effects to the observations of the near field characteristics as in [4], [6] & [7], where interpretations are limited due to resolution. However, in combustor environments, mixing characteristics in the vicinity of the jet exit are very important. For instance, in the Rich Burn, Quick-Mix, Lean Burn (RQL) combustor [9], jet air is introduced to the combustor products of a rich flame to quickly reduce the mixture to a lean mixture for downstream burning. In the more recently investigated lean premixed combustors with axially controlled stoichiometry, a premixed reacting jet-in-crossflow system is used, such as that described in [10]. In applications such as these, the mixing characteristics in the "extreme" near field (within a 2 d × 4 d window near the jet exit) are critical, where the entire near field is

typically referred to downstream locations of $S < 0.3\, r^2 d$. This is the focus within the presented research.

The "extreme" near field mixing characteristics of a JICF are investigated within an environment similar to a gas turbine combustor. A single non-reacting jet is injected into a crossflow with a temperature of 1500K and Reynolds number of Re_{cf} = 1610. The jet temperature is varied to produce density ratio values of s = 3.19 & 5.32. The mean jet velocity was varied to produce three momentum flux ratio values of J = 7.0, 12.6, & 18.0, resulting in jet Reynolds numbers varying from Re_j = 2920 to 8850. Similar to [8] and [3], different jet velocity profiles are also investigated, including a fully developed turbulent pipe profile, nozzle top-hat profile, and a highly turbulent pipe-like profile. Jet center-plane scalar mixing characteristics including jet trajectory, centerline concentration decay, and scalar dissipation are explored. Due to the high crossflow temperature, the typical acetone planar laser induced fluorescence (PLIF) diagnostic could not be performed. Instead, a laser Rayleigh scattering diagnostic method was performed to measure the temperature field for mixing quantification.

The remainder of this thesis includes the theoretical foundation of the experimental methodology used (Section 2), an in-depth description of the experimental methodology used (Section 3), the processing methods incorporated (Section 4), and finally the results (Section 5) and conclusions (Section 6) of this study, including a brief description of future work.

2. Theoretical Basis of Methodology

2.1 Laser Rayleigh Scattering

Laser Rayleigh scattering (LRS) is a powerful diagnostic tool in the study of gas flow dynamics. LRS is a non-intrusive optical diagnostic and is therefore a popular method for measurements of dissipation and mixing, as performed by Feikema et al. [11] and Barlow et al. [12], density, as performed by Balla et al. [13], mixture fraction, as performed by Sutton [14] and Arndt et al. [15] , and temperature, as performed by Gordon et al. [16] and Barat et al. [17], in non-reacting and reacting flow fields.

2.1.1 Rayleigh Scattering Cross-Section

Rayleigh scattering describes the scattering of light from particles whose diameters are much smaller than the wavelength of the incident light (i.e. gas molecules) [18]. Originally investigated by Lord Rayleigh, Jean Cabannas, and others in the 19^{th} century, Rayleigh scattering was the resulting conclusions to the understanding of the origins of the intensity, color, and polarization of the atmosphere. In this application, the incident light was from the sun, a broadband, unpolarized source, resulting in the observation of full spectrum scattering in a large volume [18]. Lord Rayleigh concluded that the scattering intensity of light from air molecules is inversely proportional to the wavelength of the incident light to the fourth power and dependent on the number of particles being excited [18]. In LRS applications, a single wavelength light source is used and large volume integration is not necessary, however, the research of Lord Rayleigh can be applied.

Miles et al. [19] reviewed the use of Rayleigh scattering in laser diagnostics, presenting multiple methods of deriving the scattered light intensity by the treatment of the scattered light as

radiation from an infinitesimally small oscillating dipole and the use of a differential Rayleigh scattering cross-section. With lasers, the Rayleigh scattering signal is a summation of the coherent Cabannas lines, the rotational Raman lines, and the vibrational Raman lines [19]. Including all components, Miles et al. expresses a total scattering cross-section, σ (cm^2), and total differential scattering cross-section for linearly, vertically polarized incident light, $\frac{\partial^V \sigma_0}{\partial \Omega}$ (cm^2 sr^{-1}) as:

$$\sigma = \frac{32\pi^2(n-1)^2}{3N^2\lambda^4}\left(\frac{6+3\rho_0}{6-7\rho_0}\right) \quad \textbf{(2.1)}$$

$$\frac{\partial^V \sigma_0}{\partial \Omega} = \frac{3\sigma}{8\pi}\frac{2}{2+\rho_0} \quad \textbf{(2.2)}$$

where n is the gas index of refraction, N is the number density of scatterers (cm^{-3}), λ is the incident laser wavelength (cm), and ρ_0 is the depolarization ratio of unpolarized (natural) light. In most laser applications, the incident light is polarized, and therefore, the depolarization ratio of linearly polarized incident light must be used in determining the differential scattering cross-section. Long [20] expresses the unpolarized and linearly polarized depolarization ratios (ρ_0 and ρ respectively) as:

$$\rho_0 = \frac{6\gamma^2}{45a^2+7\gamma^2} \quad \textbf{(2.3)}$$

$$\rho = \frac{3\gamma^2}{45a^2+4\gamma^2} \quad \textbf{(2.4)}$$

where $\gamma^2$and a^2 are the traditional invariants of the anisotropy and mean polarizability of the polarizability tensor respectively. Rearranging Eq. (2.4) to solve for $45a^2$, substituting into Eq. (2.3) and simplifying, yields an expression for the depolarization ratio of unpolarized light in terms of the depolarization ratio of linearly polarized light:

$$\rho_0 = \frac{2\rho}{1+\rho} \tag{2.5}$$

Substituting Eqs. (2.1) and (2.5) into Eq. (2.2) yields the expression for the total differential Rayleigh cross-section for vertically polarized incident light used in the current work:

$$\frac{\partial\sigma}{\partial\Omega} = \frac{4\pi^2(n-1)^2}{N^2\lambda^4}\left(\frac{6+6\rho}{6-8\rho}\right) \tag{2.6}$$

2.1.2 Rayleigh Thermometry

In LRS, the power of a collected signal, P_D (W), is dependent on the integral of the effective differential Rayleigh scattering cross-section over a collection angle, $\Delta\Omega$ (sr), the number density of scattering particles (scatterers), N (mol cm^{-3}), the probe volume, V (cm^3), the incident laser intensity, I_L (W cm^{-2}), and the efficiency of all collection optics, η [19]:

$$P_D = \eta I_L N V \int_{\Delta\Omega}\left(\frac{\partial\sigma}{\partial\Omega}\right)_{eff}\partial\Omega \tag{2.7}$$

For most laser diagnostic applications, Rayleigh scattered light is typically detected by a collection lens over a small collection angle, with which Eq. (2.7) can be approximated as [14]:

$$I_D = \eta I_L n l \Omega\left(\frac{\partial\sigma}{\partial\Omega}\right)_{eff} \tag{2.8}$$

where the detected signal intensity, I_D (W cm^{-2}), is dependent on the concentration of scatterers in the probe volume, n (cm^{-3}), the length of the probe volume on the detector, l (cm), the solid angle of the collection optics, Ω (sr), and the effective differential Rayleigh scattering cross-section of the scatterers, $\left(\frac{\partial\sigma}{\partial\Omega}\right)_{eff}$ (cm^2 sr^{-1}). In applications where the scattering media consists of multiple molecules, such as gas mixtures, the effective differential Rayleigh scattering cross-section is the molar-averaged value of all molecules:

$$\left(\frac{\partial\sigma}{\partial\Omega}\right)_{eff} = \sum_{i=1}^{K} X_i \left(\frac{\partial\sigma}{\partial\Omega}\right)_i \qquad i = 1,2,3,\dots,K \tag{2.9}$$

where X_i and $\left(\frac{\partial\sigma}{\partial\Omega}\right)_i$ are the mole fraction and differential Rayleigh scattering cross-section of the i-th molecule, respectively, and K is the total number of molecules in the mixture.

When gas mixtures are investigated using LRS, and the pressure is known, the concentration of molecules in the probe volume can be related to temperature by the ideal gas law:

$$n = \frac{pN_A}{RT} \tag{2.10}$$

where p is the gas pressure (atm), N_A is Avogadro's number (6.022 x 10^{23} mol^{-1}), R is the universal gas constant (82.057 cm^3 atm K^{-1} mol^{-1}), and T is the gas temperature (K). When this correlation is used, the LRS application is often referred to as laser Rayleigh thermometry. In experiments, a photodetector is often used to measure the incident laser pulse energy, E_P (mJ), which is related to laser intensity by:

$$E_P = \int_{\Delta t} I_L A \, dt = I_L A \Delta t = \frac{I_L A}{f_P} \tag{2.11}$$

where A is the laser beam area (cm^2) and f_P is the pulse frequency (Hz). Inserting Eqs. (2.9) – (2.11) into Eq. (2.8) the LRS signal for Rayleigh thermometry is expressed as:

$$I_D = \frac{\eta f_P p N_A l \Omega}{AR} \frac{E_P}{T} \sum_{i=1}^{K} X_i \left(\frac{\partial\sigma}{\partial\Omega}\right)_i \qquad i = 1,2,3,\dots,K \tag{2.12}$$

In most experiments, Eq. (2.12) is simplified to:

$$I_D = C\frac{E_P}{T}\sum_{i=1}^{K} X_i\left(\frac{\partial\sigma}{\partial\Omega}\right)_i \quad i = 1,2,3,\dots,K \tag{2.13}$$

where C is a constant that encompasses all of the constants related to the experimental set-up:

$$C = \frac{\eta f_P p N_A l \Omega}{AR} \tag{2.14}$$

and is frequently referred to as a calibration constant. Upon rearrangement of Eq. (2.13), the temperature of a gas mixture is determined using the non-intrusive Rayleigh thermometry LRS diagnostic tool:

$$T = C\frac{E_P}{I_D}\sum_{i=1}^{K} X_i\left(\frac{\partial\sigma}{\partial\Omega}\right)_i \quad i = 1,2,3,\dots,K \tag{2.15}$$

2.2 Scalar Dissipation and Mixing Time Scales

In turbulent flows, the mixing of scalar quantities such as temperature and species concentrations is of great importance. A common measure of the mixing rate of a scalar in a turbulent flow field is the scalar dissipation rate. Scalar dissipation can be measured using LRS, as explained by Feikema et al. [11], planar laser induced fluorescence (PLIF) as performed by Soulopoulos et al. [21], or a combination of LRS, Raman scattering and laser-induced fluorescence (LIF) as performed by Barlow et al. [12].

The transport of a scalar quantity, ϕ, is governed by the equation:

$$\rho\frac{\partial\phi}{\partial t} + \rho\boldsymbol{v}\cdot\nabla\phi = \nabla\cdot\left(\rho D_\phi\nabla\phi\right) + \rho S_\phi \tag{2.16}$$

where D_ϕ is the molecular diffusivity of the scalar quantity and ρS_ϕ is the chemical source term. Similar to the analysis of vector quantities in a turbulent flow field, a scalar in a turbulent flow

field $\phi(\boldsymbol{x},t)$ is decomposed into average $\tilde{\phi}(\boldsymbol{x},t)$ and fluctuating components $\phi''(\boldsymbol{x},t)$ as expressed in Eq. (2.17).

$$\phi(\boldsymbol{x},t) = \tilde{\phi}(\boldsymbol{x},t) + \phi''(\boldsymbol{x},t) \tag{2.17}$$

However, in the turbulent scalar analysis implemented here, Favre-average decomposition is used, rather than the common Reynolds-averaged decomposition. The major difference between these two methods is that Favre-averaging uses a density-weighted time average and Reynolds decomposition uses classical time averaging. The premise of Favre-averaging is that the average of the product of the density, ρ, and the fluctuations, ϕ'', goes to zero, rather than the average of ϕ'' only, as in Reynolds-averaging [22]:

$$\overline{\rho\phi''} = 0 \tag{2.18}$$

The Favre-average quantity, $\tilde{\phi}$, can be determined by multiplying Eq. (2.17) by ρ, averaging, and using the definition in Eq. (2.18) [22]:

$$\tilde{\phi} = \frac{\overline{\rho\phi}}{\bar{\rho}} \tag{2.19}$$

The advantage of using Favre-averaging is that when averaging terms containing the product of the dependent variable and density, the influence of density fluctuations does not appear, ultimately simplifying the averaged equations in variable density flows [22].

In [22], Peters derives the Favre-averaged scalar transport equation:

$$\bar{\rho}\frac{\partial\tilde{\phi}}{\partial t} + \bar{\rho}\tilde{\boldsymbol{v}}\cdot\nabla\tilde{\phi} = \nabla\cdot\overline{\left(\rho D_{\phi}\nabla\phi\right)} - \nabla\cdot\left(\bar{\rho}\widetilde{\boldsymbol{v}''\phi''}\right) + \bar{\rho}\widetilde{S_{\phi}} \tag{2.20}$$

Similar to Reynolds-average analysis, a closure problem exists with the turbulent transport term, $\nabla\cdot\left(\bar{\rho}\widetilde{\boldsymbol{v}''\phi''}\right)$. Peters presents a method to model this term by deriving an equation for the

average scalar variance, $\widetilde{\phi''^2}$. A result of this derivation is the Favre-average scalar dissipation rate, $\tilde{\chi}_\phi$ [22]:

$$\tilde{\chi}_\phi = 2D_\phi\left(\widetilde{\nabla\phi''}\right)^2 \quad \textbf{(2.21)}$$

This definition for $\tilde{\chi}_\phi$ is similar to the turbulent kinetic energy dissipation rate, ε, in the turbulent kinetic energy closure model of Reynolds-averaged Navier-Stokes analysis; $\tilde{\chi}_\phi$ is the rate at which the variance of scalar fluctuations declines at the molecular level, and ε is the rate at which the variance of velocity fluctuations (turbulent kinetic energy) dissipates at the molecular level. Since $\tilde{\chi}_\phi$ is a rate, a mixing time scale, τ_ϕ, can be defined as [22]:

$$\tau_\phi = \frac{\widetilde{\phi''^2}}{\tilde{\chi}_\phi} \quad \textbf{(2.22)}$$

By use of $\tilde{\chi}_\phi$ & τ_ϕ, a scalar field can aid the analysis of the mixing processes in a turbulent flow field, where large values of $\tilde{\chi}_\phi$ indicate large scale fast mixing and small values indicate either no mixing or that the flow field is well mixed at the molecular level.

Similar to the use of ε in the analysis of a turbulent velocity field, experimental resolution is key for validity. In order for a resolution to be sufficient in the investigation of a turbulent flow field, the smallest possible length scale of the measured quantity must be defined. The smallest length scale for a scalar is defined as the Batchelor scale, η_B [23]:

$$\eta_B = \left(\frac{\nu D^2}{\varepsilon}\right)^{\frac{1}{4}} = \frac{\eta}{\sqrt{Sc}} \quad \textbf{(2.23)}$$

where η is the Kolmogorov length scale (the smallest length scale of turbulent kinetic energy), $Sc = \frac{\nu}{D}$ is the Schmidt number, ν is the kinematic viscosity ($m^2\ s^{-1}$), D is the mass diffusivity (m^2

s^{-1}), and ε is the turbulent kinetic energy dissipation rate ($m^2\ s^{-3}$ = W kg^{-1}). For experimental measurements of scalar dissipation, the resolution must be no larger than $2\eta_B$ or $3\eta_B$ in order to fully capture scalar fluctuations [24].

3. Experimental Methodology

3.1 Experimental Test Rig

The experimental test rig used for the JICF experiments was similar to that described in [10]. The test rig consisted of four sections: a swirl burner, a transition section, a test section, and an exhaust section, as shown in Fig. 3.1.

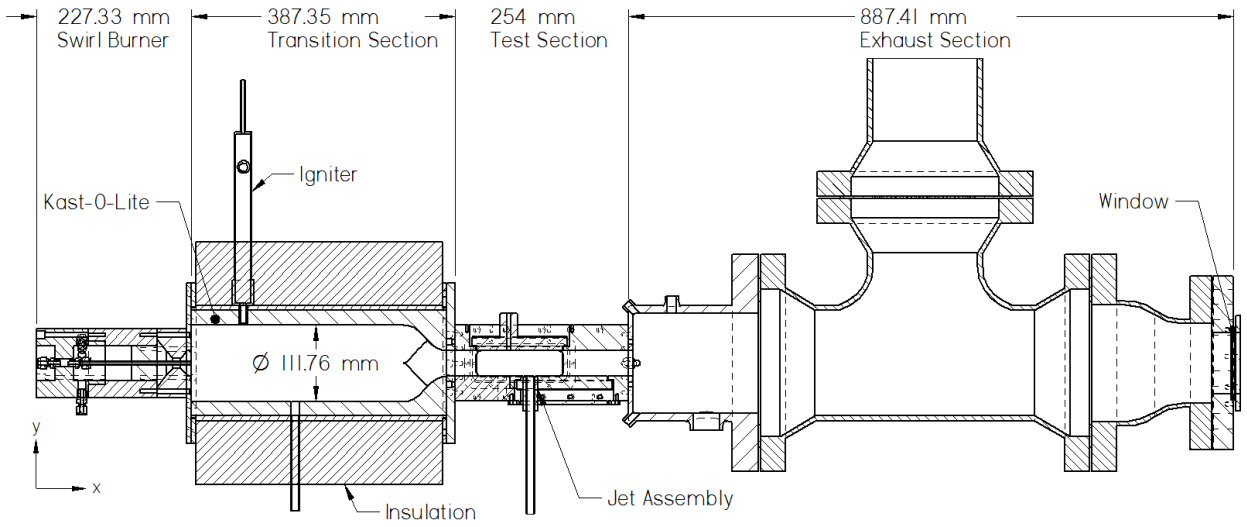

Fig. 3.1: 2D CAD drawing of experimental test rig. View shown with flush pipe jet assembly.

The swirl burner used was the same as described in [10] and generated the hot, vitiated crossflow using a premixed propane-air flame with an equivalence ratio of $\varphi = 0.865$. A propane-air torch was used to ignite the swirl-stabilized flame, labeled as igniter in Fig. 3.1, and was deactivated once a flame was stabilized on the swirl burner. The flame extended into the transition section immediately after the swirl burner exit.

The transition section was constructed of a stainless-steel body and lined with Kast-O-Lite 97L refractory to reduce heat losses. The inner flow area transitioned from a 112 mm diameter cross-section to a 38.1 mm tall, 76.2 mm wide rectangular cross-section. The circular-to-

rectangular transition followed a 5th order polynomial line developed by Bell & Mehta in [25] to produce a top-hat velocity profile. When pouring the Kast-O-Lite, a tube and 3D-printed part consisting of the polynomial line were centered in the outer stainless-steel body, providing a smooth surface on the inner wall of the transition section after the Kast-O-Lite cured. The outer body of the transition section was wrapped in a ceramic fiber insulation to further reduce heat losses. The size of the transition section was chosen such that the swirl-stabilized flame did not extend into the test section.

A detailed cross-section of the test section is shown in Fig. 3.2.

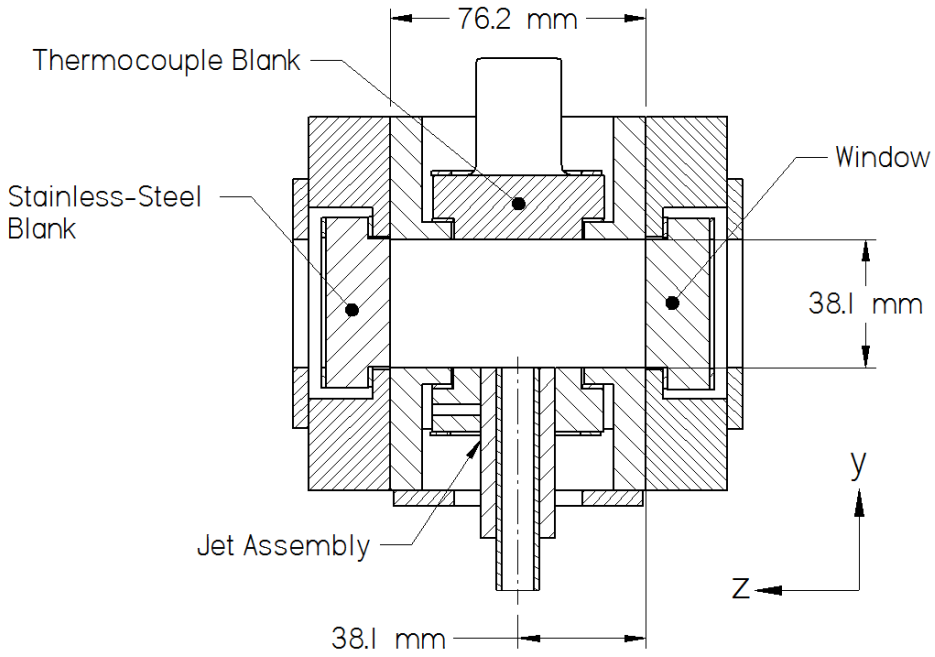

Fig. 3.2: Detailed cross-section view of test section. Cross-section shown with flush pipe jet assembly.

The test section walls were constructed of stainless-steel with an inner flow area of 38.1 mm x 76.2 mm. For optical access, a 127 mm x 38.1 mm x 19.05 mm UV-Fused Silica window was inserted in one of the test section walls. In the opposite wall of the window, a stainless-steel blank was inserted, and in the top wall, a stainless-steel blank with a 6.35 mm hole, located 78.43

mm downstream of the transition section was inserted for thermocouple access. The stainless-steel blanks and window were held in place in the same manner as described in [26]. Two jet assemblies were used; a flush pipe, shown in Fig. 3.3, and a flush nozzle, shown in Fig. 3.4. Both assemblies were held in place in the same manner as the window and stainless-steel blanks and centered in the Z-direction.

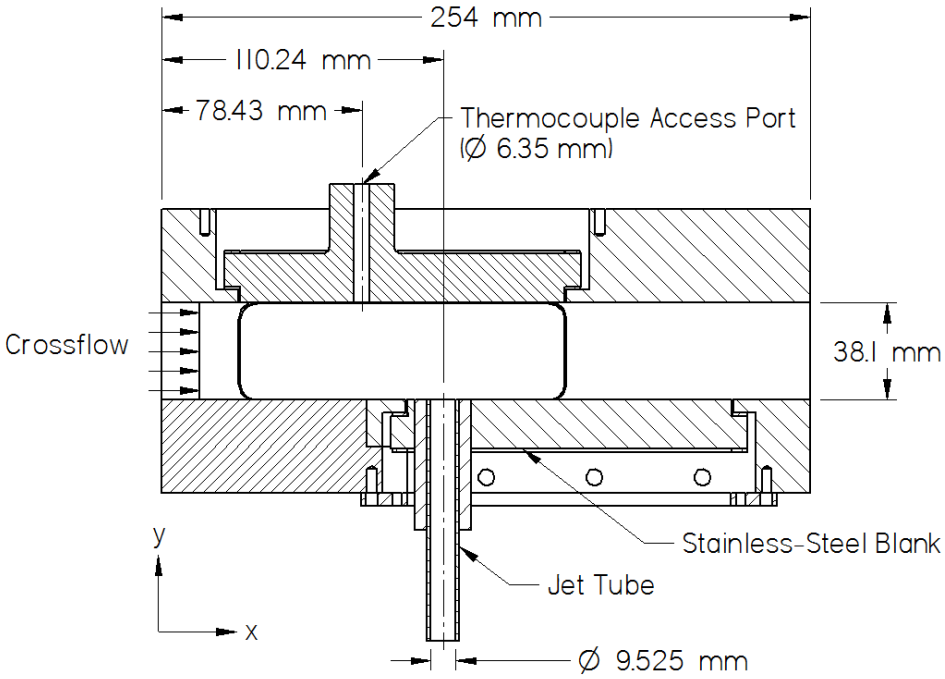

Fig. 3.3: Section view of flush pipe jet assembly in test section.

The flush pipe jet was a stainless-steel tube with an inner diameter of 9.525 mm, and was press-fit into a stainless-steel blank. The jet tube centerline was located 110.24 mm downstream of the transition section exit and centered in the flow (z-direction). The tube length was 558.8 mm, ensuring fully-developed flow.

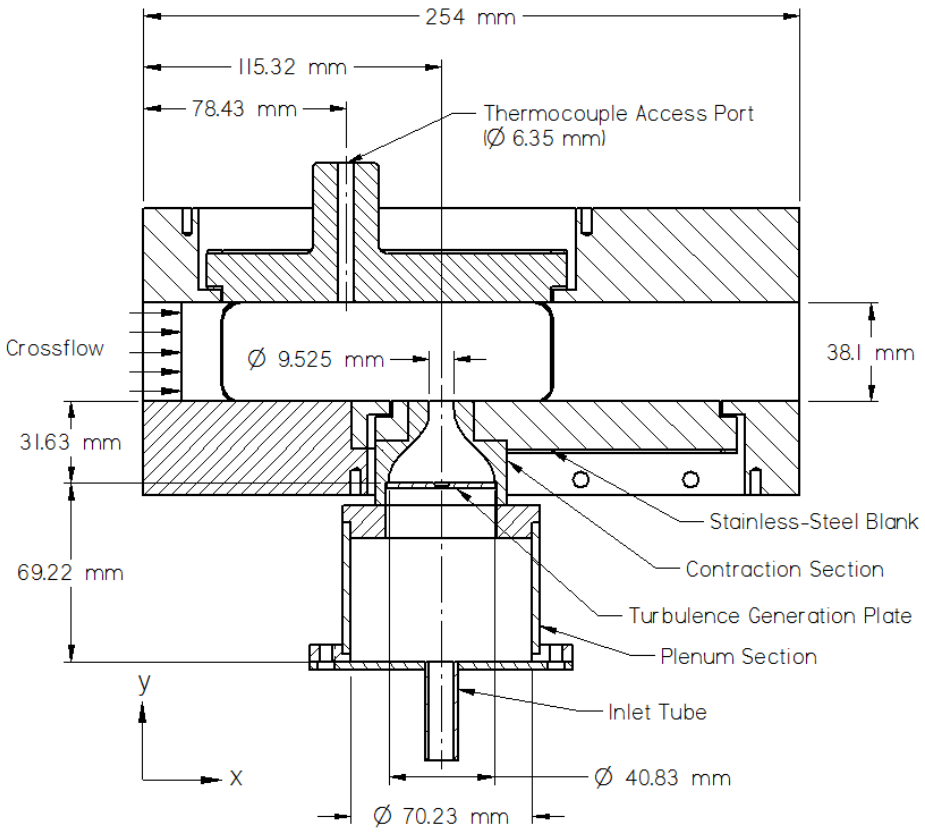

Fig. 3.4: Section view of flush nozzle jet assembly in test section.

The flush nozzle jet was constructed of three main components: a plenum section, a contraction section, and a stainless-steel blank. All sections were made of stainless-steel. The plenum section consisted of a 70.23 mm inner diameter pipe with a removable bottom flange, acting as an access port to the contraction section. A 9.525 mm inner diameter inlet tube was welded to the bottom flange for jet mixture flow. The contraction section was bolted to the top of the plenum section and press-fit into the stainless-steel blank. The contraction followed a 5^{th} order polynomial line derived in [25] from a diameter of 40.83 mm to 9.525 mm and was 31.63 mm long and 69.22 mm from the inlet tube in the y-direction. The center of the contraction exit was located 115.32 mm downstream of the transition section exit and centered in the flow (z-direction). The inner surface was sanded to a smooth finish. Just before the start of the

contraction, a step was machined into the contraction block to allow a honeycomb piece or a turbulence generating plate to be bolted in place.

The jet flow rates were controlled using a mass flow controller and a choked orifice with pressure regulator. The mixture was passed through a Sylvania 038826 hot air threaded inline heater, which was turned on only for the heated cases, before entering the jet pipe or jet plenum section.

The exhaust section was downstream of the test section and all flows were vented to the atmosphere. At the end of the exhaust section, a window assembly was attached for laser access. A 101.6 mm diameter UV-Fused Quartz window was used and held in place in a similar manner to the test section windows.

3.2 Crossflow Characterization

Particle image velocimetry (PIV) was used to characterize the velocity profile. The PIV set-up was similar to that explained in [10] with the exception that the laser sheet was passed through the window in the exhaust section. PIV measurements were performed along the test section centerline (z-direction). Fig. 3.5 shows the resulting time average velocity profile at the jet centerline (x-direction). The measured crossflow mean velocity used for all calculations of J was u_{cf} = 7.5 m s^{-1}.

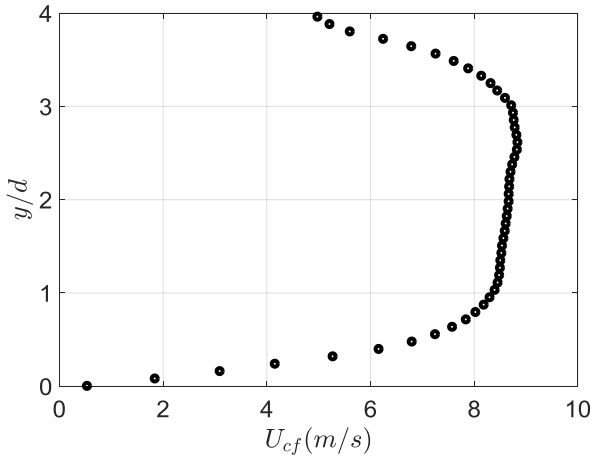

Fig. 3.5: Crossflow velocity profile.

To characterize the thermal profile, an R-type thermocouple attached to a micrometer was placed in the thermocouple access port shown in Fig. 3.3 and Fig. 3.4, which was rotated 180°, aligning the thermocouple access port with the jet center in the x-direction. The thermocouple was moved up from the jet floor (y-direction) in 2.54 mm increments to the top wall using the micrometer. At each point, the temperature was recorded for a few seconds, ensuring a steady value was recorded. This process was performed multiple times, and the resulting profile, Fig. 3.6, was taken as the average of the measurements. All temperatures were corrected for radiation.

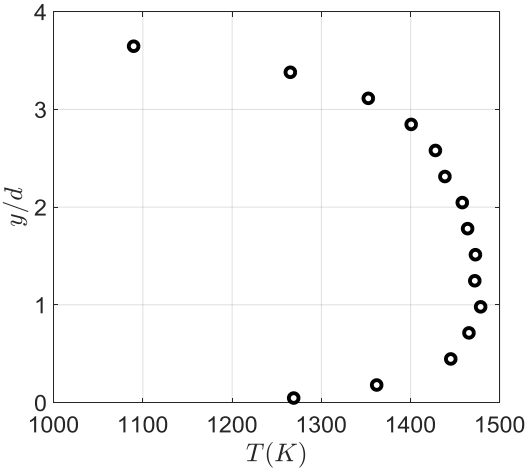

Fig. 3.6: Crossflow temperature profile.

The composition of the crossflow was determined by a computational model performed using CANTERA [27] within MATLAB. All model calculations used the thermodynamic, transport, and chemical kinetic data from the USC-II chemical mechanism [28]. The crossflow was modeled as two parts: a 1-D burner-stabilized flame to represent the swirl burner and a constant pressure reactor system representing the transition section. A premixed propane-air mixture at standard temperature and pressure (STP), *P=1atm, T=300K*, with φ = 0.865 was fueled into the burner-stabilized flame (BSF). The products of the flame were then fed into the reactor system that consisted of a constant pressure reactor (CPR) with heat loss to an ambient air reservoir (AAR) at STP. The heat flux, $\dot{q}$, was chosen such that the reactor exit temperature was equal to 1500 K to match measured experimental values after a residence time equal to that of the swirl burner products in the transition and test section of the experimental rig. A schematic of the crossflow model can be seen in Fig. 3.7. Species with calculated mole fractions greater than 10^{-6} are listed in Table 3.1.

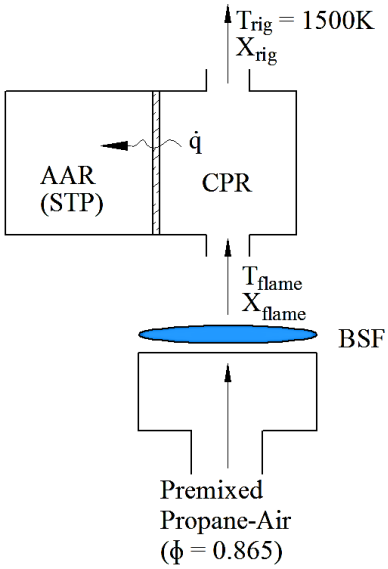

Fig. 3.7: Schematic of CANTERA crossflow model

Table 3.1: Crossflow species mole fractions, as calculated by CANTERA model.

Species	Mole Fraction
N_2	0.7315
H_2O	0.1315
O_2	0.0289
CO_2	0.0994
Ar	8.64×10^{-3}
H_2	1.60×10^{-6}
CO	3.18×10^{-6}
OH	6.66×10^{-5}

Using the CANTERA calculated mixture composition, the crossflow Reynolds number was calculated to be Re_{cf} = 1610 based on the hydraulic diameter of the rectangular test section.

3.3 Jet Characterization

The jet velocity profile was measured using PIV with the same laser and camera as the crossflow PIV. The jet assembly was removed from the test section, and set-up on a separate table with the laser sheet being passed over the jet center directly from the laser head. This set-up allowed the jet exit velocity profile to be measured without confinement.

The flush pipe jet had a fully developed turbulent pipe velocity profile with a turbulence intensity of 4%. The flush nozzle jet, without any turbulence generating plates, had a top-hat velocity profile with a turbulence intensity of 8%. To avoid a Helmholtz resonance observed in the turbulent jet assembly without a turbulence generating plate, an aluminum hexagonal honeycomb was fit into the contraction section step to keep the volume the same as when a turbulence generating plate was used. The honeycomb consisted of 1.5875 mm hexagons with wall thickness of 0.127 mm and was 12.7 mm thick. To generate a jet flow with high levels of

turbulence, a turbulence generating plate was used. The plate was made of 1.93 mm thick stainless steel and consisted of a 4.76 mm diameter hole centered in the plate with a 60° counter-sink and a 0.51 mm thick landing, resulting in a 99% blockage ratio. The plate generated 40% turbulence intensity (TI) with a Gaussian-type velocity profile. Section views of the honey-comb and turbulence generating plate can be seen in Fig. 3.9 (a) and (b) respectively. Fig. 3.8 (a) shows all velocity profiles normalized to their respective mean velocity. Fig. 3.8 (b) shows all turbulence intensity profiles. The shown profiles expand past the diameter of the jet due to the expansion of the free jet at the location at which the PIV data was taken.

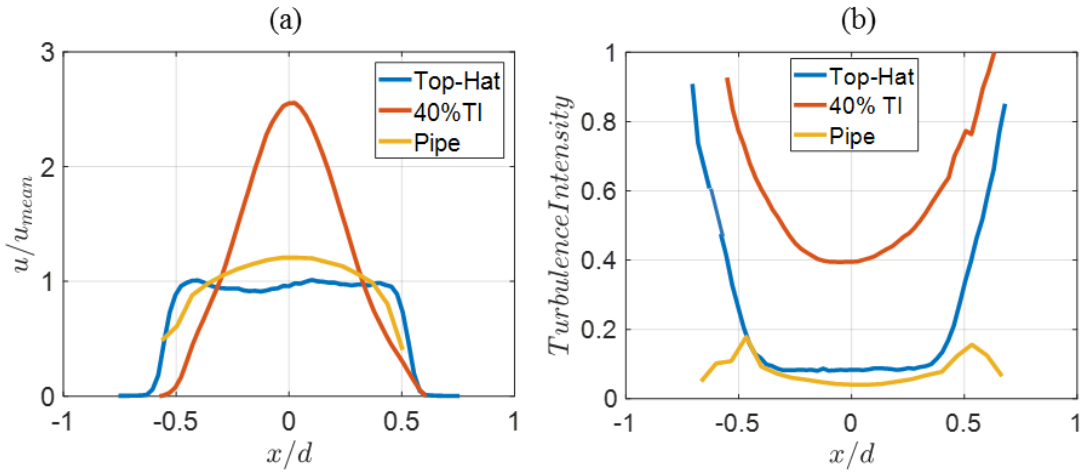

Fig. 3.8: (a) Jet velocity profiles normalized by mean velocity (b) Jet turbulence intensity profiles. Profiles are results of PIV measurements.

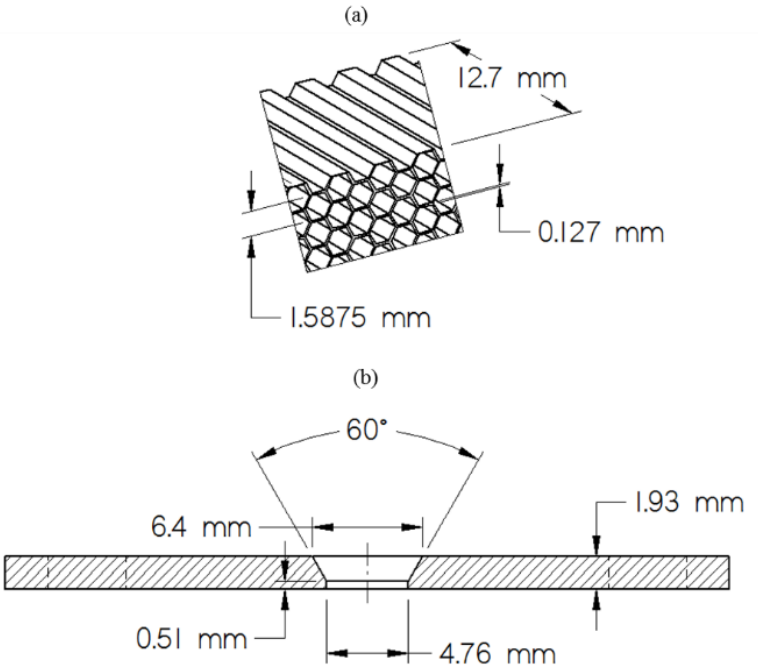

Fig. 3.9: Section views of (a) honeycomb (b) turbulence generating plate.

It should be noted that this turbulence generation plate design was chosen due to the complexity of generating high levels of symmetric turbulence on a small scale. During preliminary tests, it was noticed that quality of manufacturing is key for symmetry. When using multiple holes, a concentricity deviation of 0.025mm from the center of the plate resulted in skewed velocity profiles. In addition, to obtain a 99% blockage ratio for high levels of turbulence, much smaller holes would be needed, which would be difficult to manufacture perfectly. It was noticed that if a hole was slightly non-round, the velocity profile was skewed.

To simplify the correlation between the LRS signal and temperature, the composition of the jet was chosen such that the effective Rayleigh scattering cross-section of the jet mixture was equal to that of the crossflow. The resulting jet mixture was 91.33% Air and 8.67% CO_2 on a molar basis. The species mole fractions of the jet mixture are listed in Table 3.2.

Table 3.2: Jet species mole fractions

Species	Mole Fraction
N_2	0.7131
O_2	0.1913
CO_2	0.0870
Ar	8.495×10^{-3}

Experimental runs with a variety of jet cases were performed. Multiple momentum flux ratios, J, and density ratios, s, were investigated for each velocity profile. Density ratio differences was achieved by varying the jet temperature, T_j. The jet Reynolds number ranged from Re_j = 2920 to 8850. Table 3.3 is a summary of all cases tested.

The Batchelor scale for each test case was calculated by assuming a mass diffusivity, D, based on N_2 into N_2 and the kinematic viscosity, ν, of the jet mixture at the jet inlet temperature. The turbulent kinetic energy dissipation rate, ε, was approximated using the integral length scale determined from hotwire anemometry, using methods described in [29], of the free jet for each test case. From Eq. (2.23), the Batchelor scale is proportional to $(\nu D^2)^{1/4}$, and so by determining the values of ν and D at the jet inlet temperature, the calculated values of the Batchelor scale are conservatively small, due to T_j being the minimum mixture temperature in each test case.

Table 3.3: Summary of LRS test cases performed

J	T_j (K)	s	r	Re_j	Velocity Profile	η_B (μm)
7.0	300	5.32	1.15	5520	Pipe	92
12.6	300	5.32	1.54	7400	Pipe	74
18.0	300	5.32	1.84	8850	Pipe	64
7.0	500	3.19	1.48	2920	Pipe	147
12.6	500	3.19	1.99	3920	Pipe	118
7.0	300	5.32	1.15	5520	Top-Hat	64
12.6	300	5.32	1.54	7400	Top-Hat	52
18.0	300	5.32	1.84	8850	Top-Hat	45
7.0	500	3.19	1.48	2920	Top-Hat	104
12.6	500	3.19	1.99	3920	Top-Hat	83
7.0	300	5.32	1.15	5520	40% TI	24
12.6	300	5.32	1.54	7400	40% TI	19
18.0	300	5.32	1.84	8850	40% TI	17
7.0	500	3.19	1.48	2920	40% TI	38
12.6	500	3.19	1.99	3920	40% TI	31

3.4 Laser Rayleigh Imaging

3.4.1 Laser and Optical Set-Up

The Rayleigh thermometry laser and optical set-up is shown in Fig. 3.10.

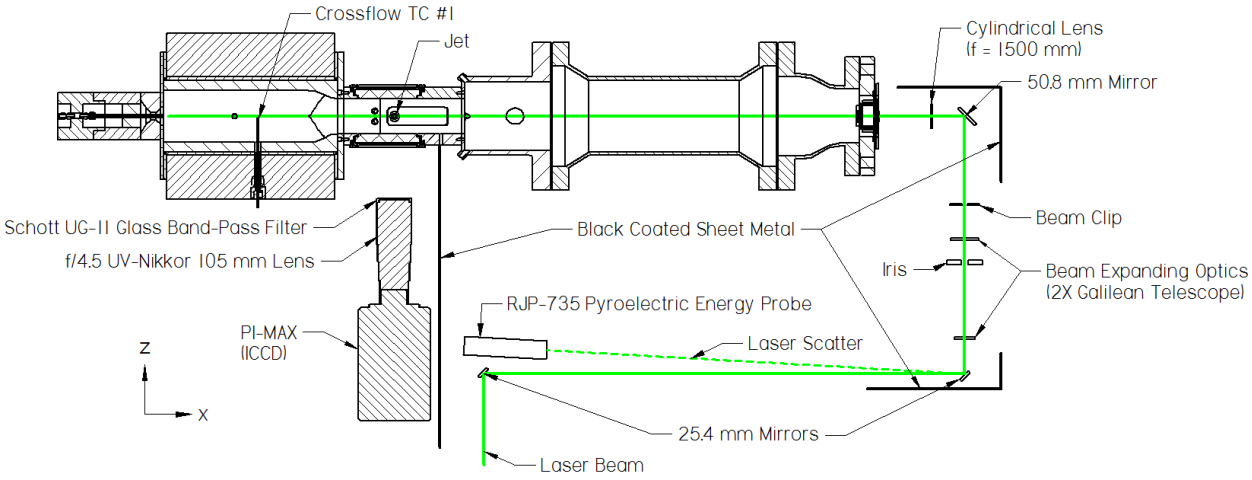

Fig. 3.10: Rayleigh thermometry laser and optical set-up.

The frequency-tripled 355 nm output beam of a Spectra Physics Pro-230 Nd:YAG laser with an average pulse energy of 250 mJ and repetition rate of 10 Hz, was used as the incident light source for the Rayleigh scattering. To reduce scattering and background noise in the images, the laser was set in a separate room from the experimental rig and passed through a 25.4 mm hole in a wall separating the rooms. In the experimental rig room, the beam was reflected 90° twice using 25.4 mm diameter mirrors. Following the second mirror, the beam passed through a 2X Galilean telescope with an iris between the two lenses to remove unwanted beam edges. After the telescope, the beam passed through a beam clip to remove additional unwanted beam edges. The beam was then reflected 90° and formed into to a 25 mm tall x 200 μm sheet at the jet exit using a 1500 mm cylindrical convex lens, passing through the downstream window assembly.

The scattering signal was acquired using a Princeton PI-MAX ICCD camera equipped with an f/4.5 UV-Nikkor 105 mm lens and a Schott UG-11 glass band-pass filter. The band-pass filter allowed over 75% transmission at 355 nm, with a transmission cutoff wavelength of 390 nm. The camera resolution was limited to 1024 x 781 pixels, incorporating a 25.9 mm x 19.8 mm region, resulting in a resolution of 25.3 μm/pixel. Compared to the Batchelor scale, the resolution ranged from $0.2\eta_B$ to $1.5\eta_B$. The bottom of the region was set to 1.5 mm, $0.16d$, above the jet exit to avoid burning intensifier pixels with laser light scatter from the bottom of the test section. An intensifier gain of 255 was used for all images. The camera was triggered by a DG535 delay generator to coincide the camera gate with every 10^{th} laser pulse. The LRS images were recorded at a frequency of 1 Hz with a total of 400 images for each test case. To correct the scattering images for laser sheet intensity, an additional 40 images, with crossflow only, were taken immediately before (IC) and after (ENDIC) each set of test images.

The crossflow temperature was monitored using two R-type thermocouples, one in the transition section, as shown in Fig. 3.10, and one in the thermocouple access port in the test section, shown in Fig. 3.3 and Fig. 3.4. The thermocouple in the access port was slightly bent away from the test section centerline (z-direction) to avoid being hit by the laser sheet. Image taking was not conducted until the crossflow reached steady state on both thermocouple readings, approximately 50 minutes after swirl burner ignition. The jet temperature was monitored using an R-type thermocouple placed in the jet tube for the turbulent pipe jet and immediately before the plenum section for the turbulent contraction jet. All temperatures were corrected for radiation. Laser energy was monitored using a Laser Precision Corp. RJ-7620 energy meter with a RJP-735 pyroelectric energy probe. Using a camera-triggered LabVIEW

program, the crossflow temperature, jet temperature, and laser energy were recorded at each camera frame.

3.4.2 Laser Scatter Noise Reduction

To reduce laser light scatter noise in the images, three flat black paint coated sheet metal pieces were used to contain laser scatter near the beam optics, as shown in Fig. 3.10. One piece was placed next to the camera, preventing laser scatter from entering the field of view. In the test section, laser scatter noise was reduced by painting the jet floor, side walls, and top wall with Superior Industries, Inc. Thermal-Kote High Temperature flat black paint. All lights in the rig room were turned off as well to further reduce ambient light noise. A signal-to-noise ratio (SNR) of 6.2 was measured in the crossflow region, and a SNR of 13.7 was measured in the jet region. To eliminate large particles entering the field of view, the jet mixture was passed through an Arrow Pneumatics F500-02 coalescing filter with a 0.03 μm element.

4. Image Processing and Computational Methods

4.1 Calculation of Differential Rayleigh Scattering Cross-Section

From Eq. (2.6), the differential Rayleigh scattering cross-section is dependent on the number density, N (cm^{-3}) of the scatterers. For a gas, the number density can be related to temperature using the ideal gas law. By doing so, there would be an implication that the differential Rayleigh scattering cross-section is dependent on gas temperature. However, Sutton et al. [30] showed that temperature dependence of the scattering cross-section is slight, resulting in scattering cross-section increases of 2-8% for temperatures up to 1525 K at 355 nm. Therefore, the Loschmidt number (n_0 = 2.6867805 x 10^{19} cm^{-3}) at standard temperature and pressure (STP = 0°C, 1 atm) was used to calculate all differential Rayleigh scattering cross-sections. The index of refraction for each species in the crossflow and the jet was determined using the constants and dispersion formula presented by Gardiner et al. [31] at 355 nm:

$$(n-1)\times 10^{6} = \frac{a}{b-\lambda^{-2}} \qquad \textbf{(4.1)}$$

where n is the index of refraction at STP, a and b are constants determined by Gardiner et al., and λ is the laser wavelength (Å). The constants presented were determined using a least squares fit program on Eq. (4.1) with values of n from other literature [31]. An accuracy of 1/10^4 is reported for the dispersion formula predictions and cited data [31]. The depolarization ratio for each species in the crossflow and the jet was extrapolated from the values presented by Bogaard et al. [32] to 355 nm. The index of refraction, depolarization ratio for linearly polarized incident light, and differential Rayleigh scattering cross-section for each species in the jet and crossflow at 355 nm are listed in Table 4.1.

Table 4.1: Index of refraction, depolarization ratio for linearly polarized incident light, and differential Rayleigh scattering cross-section for all species considered in flow at 355 nm.

Species	$(\boldsymbol{n-1})$ x 10^6	$\boldsymbol{\rho}$ x 10^3	$\frac{\partial\sigma}{\partial\Omega}$ x 10^{27} ($cm^2\ sr^{-1}$)
N_2	294.52	10.960	3.0639
H_2O	245.58	0.299	2.0778
O_2	265.36	28.084	2.5894
CO_2	437.60	42.957	7.2938
Ar	277.24	0	2.6463
H_2	136.06	10.890	0.6538
CO	327.28	5.310	3.7337
OH	329.57	N/A	3.7395

Using Eq. (2.9), the effective differential Rayleigh scattering cross-section of the crossflow and jet was 3.3376 x 10^{-37} ($cm^2\ sr^{-1}$).

4.2 Image Processing

4.2.1 Image Filtering and Laser Correction

All LRS images were filtered to remove Gaussian (amplifier) noise and corrected for laser intensity profile changes during the image taking process. Prior to filtering for amplifier noise, the images were scanned for bad pixels (values above a standard deviation threshold) and replaced these values using an inpainting function [33]. The images were then filtered using a bilateral filter [34] and a mean filter. The bilateral filter was used to smooth the images, while maintaining gradients, the mean filter was used to slightly blur the images. The test images were filtered using smaller standard deviation values for the Gaussian bilateral filter window to further preserve gradients. Values of 4 and 0.5 were used for the spatial-domain and intensity-domain standard deviations, respectively, for the test images, while values of 8 and 1 were used for the laser sheet correction images.

An image-to-image laser correction was performed on the test images prior to performing the filtering process. Images were corrected for laser intensity profile using the filtered IC and ENDIC image sets. Both sets were averaged over their acquisition time, t_{IC} and t_{ENDIC}, and normalized based on the maximum intensity of the time averaged image, $\overline{I_{IC}(x,y,t_{IC})}$ and $\overline{I_{ENDIC}(x,y,t_{ENDIC})}$, creating a normalized starting laser profile, $I_{IC,norm}$, and ending laser profile, $I_{ENDIC,norm}$. Eqs. (4.2) and (4.3) describe this process mathematically. Fig. 4.1 (a) and Fig. 4.1 (b) show the filtered, normalized IC and ENDIC laser profiles.

$$I_{IC,norm} = \frac{\overline{I_{IC}(x,y,t_{IC})}}{\max(\overline{I_{IC}(x,y,t_{IC})})} \tag{4.2}$$

$$I_{ENDIC,norm} = \frac{\overline{I_{ENDIC}(x,y,t_{ENDIC})}}{\max(\overline{I_{ENDIC}(x,y,t_{ENDIC})})} \tag{4.3}$$

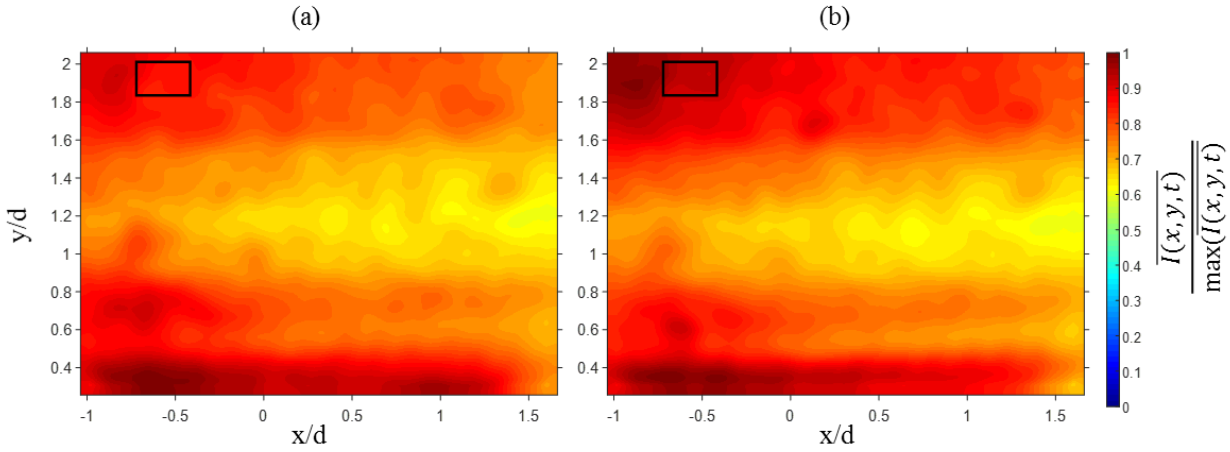

Fig. 4.1: (a) Normalized IC laser profile. (b) Normalized ENDIC laser profile.

Looking at the normalized intensities in the outlined area, there is a clear change in intensity from the IC to ENDIC images. This difference is due to slight beam steering as a result of the test section environment throughout a test image set. Taking the average pixel intensity in this area over a test image set, a linear trend is seen in the laser profile intensity, as shown in Fig. 4.2.

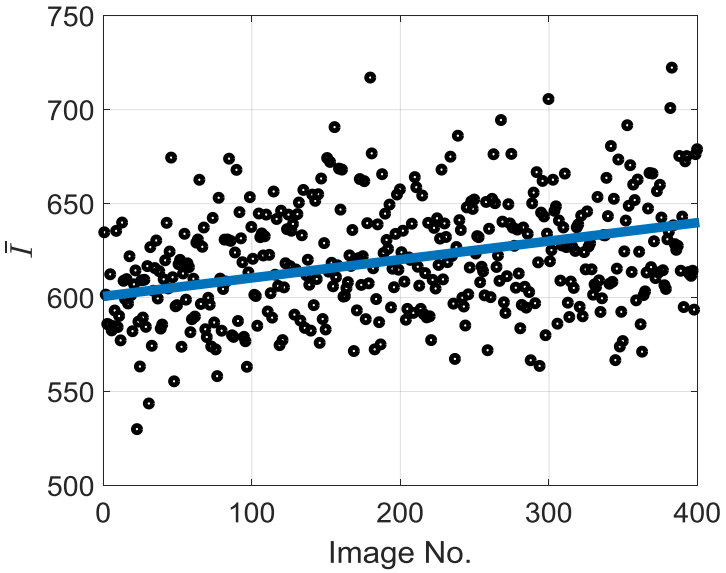

Fig. 4.2: Average pixel intensity in an area over a full test image set.

Using this linear shift of laser intensity from the IC to ENDIC image sets, a correction factor was determined for each test image, K_i (index i indicates test image number in a 400-image set):

$$K_i = \frac{i-1}{399}\left(I_{ENDIC,norm} - I_{IC,norm}\right) + I_{IC,norm} \quad \textbf{(4.4)}$$

Each test image was divided by the corresponding correction factor from Eq. (4.4). Fig. 4.3 (a) shows a raw LRS image and Fig. 4.3 (b) shows a laser corrected and filtered LRS image.

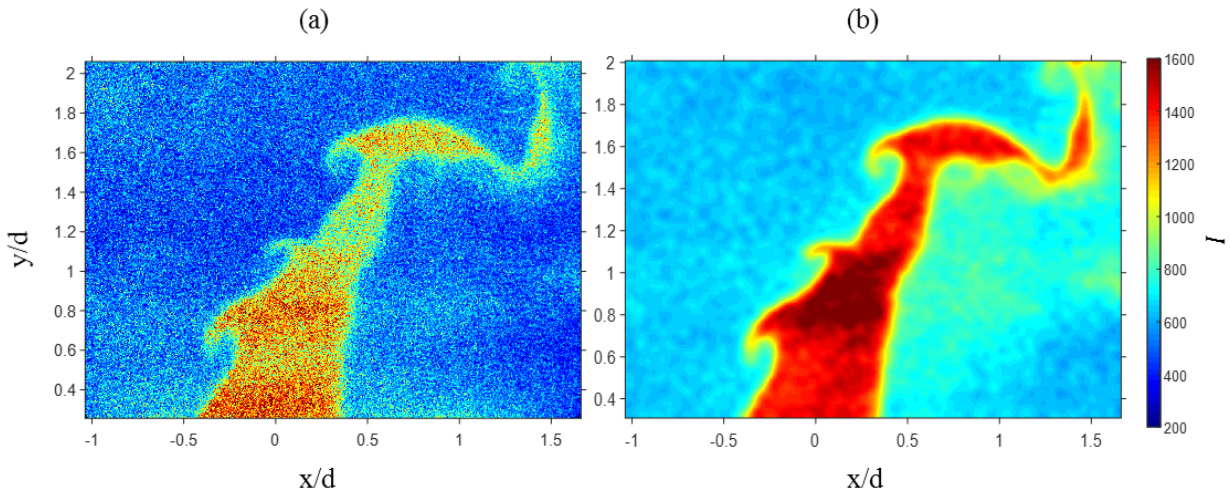

Fig. 4.3: (a) Raw LRS image. (b) Laser corrected and filtered LRS image.

4.2.2 Calculation of Temperature from LRS Images

To obtain temperature from a LRS signal using Eq. (2.15), the calibration constant, C, needs to be determined. Classical methods for determining C include performing reference experiments with known gas compositions and temperatures. From these reference experiments, either C is directly calculated, such as done by Barat et al. in [17], or is canceled out by normalizing the desired Rayleigh signal by the reference signal, such as done by Sutton in [14]. While these methods have proven to be effective, for the calculated value of C or the normalization to be accurate, all aspects of the reference experiment must be exactly the same for the true experiment. As explained in Section 4.2.1, a linear shift in laser power intensity was observed in the presented LRS experiments. Along with this shift, the observed shot-to-shot laser energy was sporadic over a test image set. Fig. 4.4 shows the pulse energy, E_P, normalized with the average pulse energy, $\overline{E_P}$, for a full LRS image set.

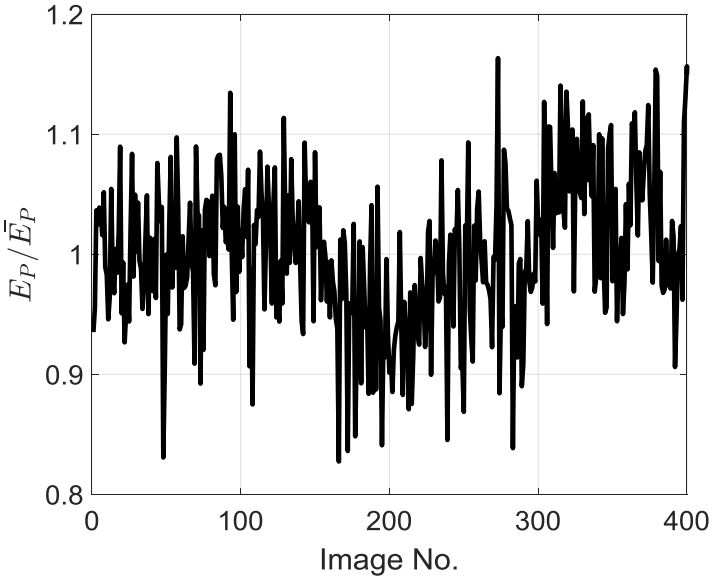

Fig. 4.4: Normalized pulse energy for a full LRS image set.

Based on these observations, an image-to-image value of C was required for the present LRS experiments.

To calculate C for a given test image, a baseline background intensity level, I_{BG}, was calculated using the average detected intensity of the crossflow region, I_{cf}, the average detected intensity of the jet core region, I_j, and the measured temperature of the jet, T_j, and crossflow, T_{cf}. Eq. (4.5) is the mathematical expression used to calculate I_{BG} and is derived from Eq. (2.13) with the "true" intensity from the gas scattering, I_{true}, being equal to the detected Rayleigh scattering signal minus the background intensity: $I_{true} = I_D - I_{BG} = \frac{C}{T}\left(\frac{\partial\sigma}{\partial\Omega}\right)$.

$$I_{BG} = \frac{I_{cf} - I_j\left(\frac{T_j}{T_{cf}}\right)}{1 - \left(\frac{T_j}{T_{cf}}\right)} \tag{4.5}$$

The differential Rayleigh scattering cross-section does not appear in Eq. (4.5) since the jet mixture was chosen to match the scattering cross-section of the crossflow, and therefore cancels

out with the T_j/T_{cf} ratio. I_{cf} and I_j were calculated by taking the averaging pixel intensity in an area, as shown in Fig. 4.5; the black line and white line indicates the area for I_{cf} and the area for I_j respectively.

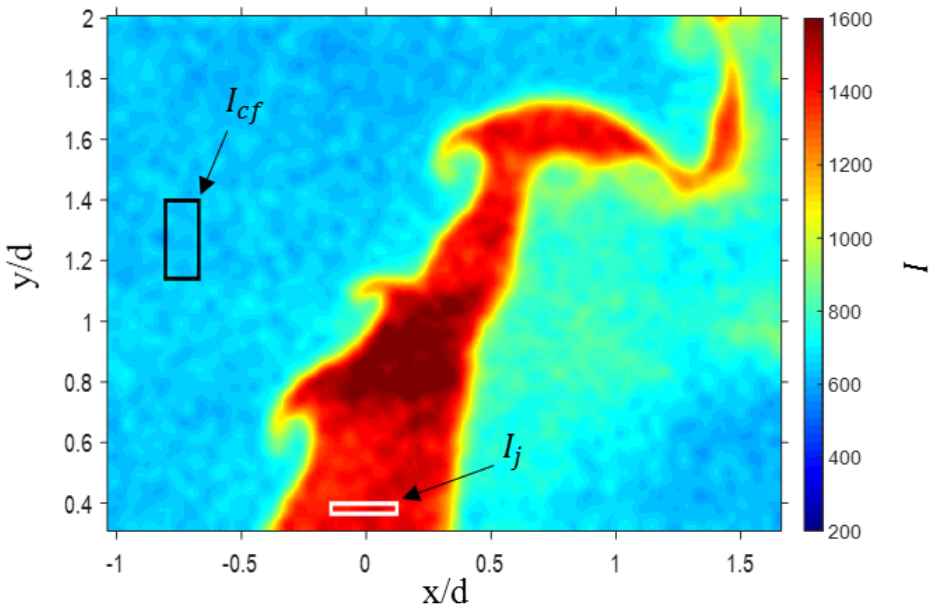

Fig. 4.5: Intensity window locations for I_{cf} (black line) and I_j (white line).

Using the thermocouple measured temperature data, the calculated average intensity for I_{cf} and I_j were set to have the corresponding temperature values of T_{cf} and T_j respectively in Eq. (4.5) since the ratio eliminates C, similar to as done by Sutton in [14]. Once the background intensity level was determined, the value of C for the given image was calculated using Eq. (4.6).

$$C = \left(I_j - I_{BG}\right)\frac{T_j}{\left(\partial\sigma/\partial\Omega\right)} \tag{4.6}$$

Using the calculated value of C, the temperature of each pixel was calculated using a variation of Eq. (2.15), with C incorporating the laser pulse energy and the subtraction of I_{BG} being the differences.

$$T = \frac{C}{I_D - I_{BG}}\left(\frac{\partial\sigma}{\partial\Omega}\right) \tag{4.7}$$

This process was performed for each image in a LRS test image set. Fig. 4.6 shows the value of C over a given test image set. Compared to the use of a constant value for C, as done in [14] and [17], the method presented here is novel, and from Fig. 4.6, it is evident that this method of calculating an image-to-image value of C is of great importance.

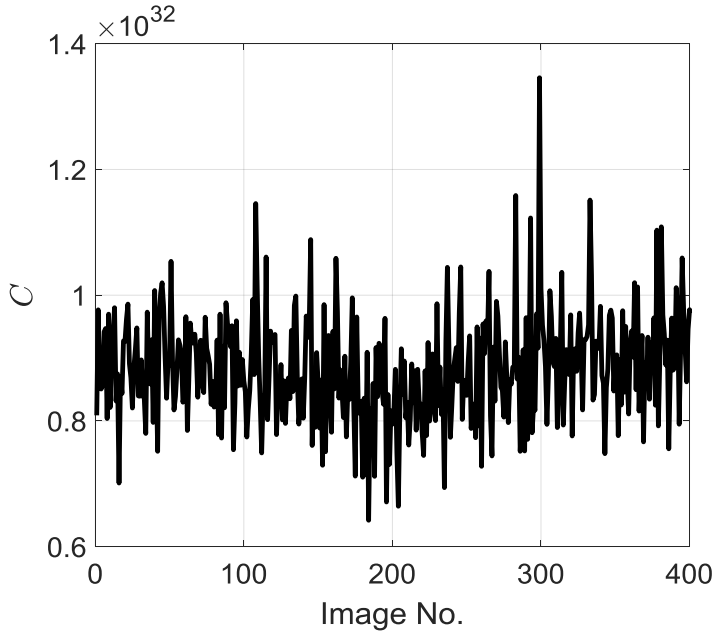

Fig. 4.6: Calculated value of C over a full test image set.

4.3 Crossflow Mixture Fraction at a Given Mixture Temperature

From the Rayleigh temperature images, the extent of crossflow-jet mixing was determined using a crossflow mixture fraction, x, defined by:

$$x = \frac{\dot{m}_{cf}}{\dot{m}_{mix}} = \frac{\dot{m}_{cf}}{\dot{m}_{cf} + \dot{m}_j} \tag{4.8}$$

where $\dot{m}_{cf}$ is the crossflow entrainment mass flow rate, $\dot{m}_{mix}$ is the crossflow-jet mixture mass flow rate, and $\dot{m}_j$ is the jet mass flow rate. The mixture fraction was calculated using the governing equations for mass and energy conservation of two mixing streams with a single outlet, mathematically described by Eqs. (4.9) and (4.10) respectively.

$$\dot{m}_{cf} + \dot{m}_j = \dot{m}_{mix} \tag{4.9}$$

$$\dot{m}_{cf} h_{cf} + \dot{m}_j h_j = \dot{m}_{mix} h_{mix} \tag{4.10}$$

where h_{cf} is the enthalpy of the crossflow, h_j is the enthalpy of the jet, and h_{mix} is the enthalpy of the crossflow-jet mixture. Rearranging Eq. (4.8) to express $\dot{m}_{cf}$ in terms of x, and using Eq. (4.9) allows for Eq. (4.10) to also be expressed in terms of x:

$$\dot{m}_{cf} = \left(\frac{x}{1-x}\right)\dot{m}_j \tag{4.11}$$

$$x h_{cf} + (1-x) h_j = h_{mix} \tag{4.12}$$

Similar to Eq. (4.12), the species mass fractions of the crossflow-jet mixture, Y_{mix}, can be expressed in terms of x and the species mass fractions of the crossflow, Y_{cf}, and the jet, Y_j:

$$x Y_{cf} + (1-x) Y_j = Y_{mix} \tag{4.13}$$

For a given temperature value in a Rayleigh image, Eqs. (4.9) and (4.11) - (4.13) were solved with an initial value of x = 0. Using CANTERA, the crossflow-jet mixture gas object was

defined using the corresponding calculated Y_{mix} and h_{mix}. Within the CANTERA gas object functionality, the gas temperature, T_{mix}, was determined from the specified h_{mix} using the polynomial constants for each species provided in the USC-II mechanism. This process was iteratively performed using MATLAB's root finding function, *fsolve*, changing the value of x at each iteration until the determined T_{mix} was equal to the input Rayleigh temperature, T_{ray}, satisfying:

$$\frac{T_{mix}}{T_{ray}} - 1 = 0 \qquad \textbf{(4.14)}$$

with function and step tolerances of 1e-6. After determining x, a CANTERA gas object was created using the corresponding mass fractions and Rayleigh measured temperature, allowing for calculations of mixture properties using the USC-II mechanism.

4.4 Scalar Dissipation Rates and Mixing Time Scales from LRS Images

For each LRS image in a given image set, the instantaneous density field was calculated using the determined pixel-to-pixel mixture properties from the method described in Section 4.3. By use of Eq. (2.19), the Favre averaged temperature field for the given image set was calculated. Each LRS image was then converted to a fluctuation image using Eq. (2.17). Using a 2nd order central differences method, the x- and y-direction gradients of each instantaneous temperature fluctuation image were calculated, and then Favre averaged. The Favre averaged scalar dissipation rate field was then calculated using Eq. (2.21), with the molecular diffusivity, D_{ϕ}, being the pixel-local thermal diffusivity, α, determined by the same methods used for the pixel-local density. Fig. 4.7 is a visualization of the scalar dissipation calculation steps. Fig. 4.7 (a) shows the density field calculated based on the procedure outlined above. Fig. 4.7 (b) shows the ensemble averaged pixel-by-pixel product of density and temperature from instantaneous

images, averaged over 400 images. In Fig. 4.7 (c) the Favre averaged mean temperature field is shown after dividing the image of Fig. 4.7 (b) by that of Fig. 4.7 (a). Fig. 4.7 (d) shows the ensemble averaged temperature fluctuation field. Fig. 4.7 (e) shows the ensemble averaged product of the instantaneous density and temperature fluctuation gradient field. The Favre averaged temperature fluctuation gradient field and Favre averaged scalar dissipation rate field are shown in Fig. 4.7 (f) and (g) respectively.

The Favre averaged mixing time scale field was then calculated using Eq. (2.22). Fig. 4.8 is a visualization of the mixing time scale calculation process. The Favre averaged temperature variance field, shown in Fig. 4.8 (b), was calculated by squaring each fluctuation image, and then Favre averaging. The method of using the pixel-to-pixel value of density and thermal diffusivity is crucial due to an 81.16% decrease in density and a 1344.89% increase in thermal diffusivity from a 100% 300 K jet mixture to a 100% 1500 K crossflow mixture.

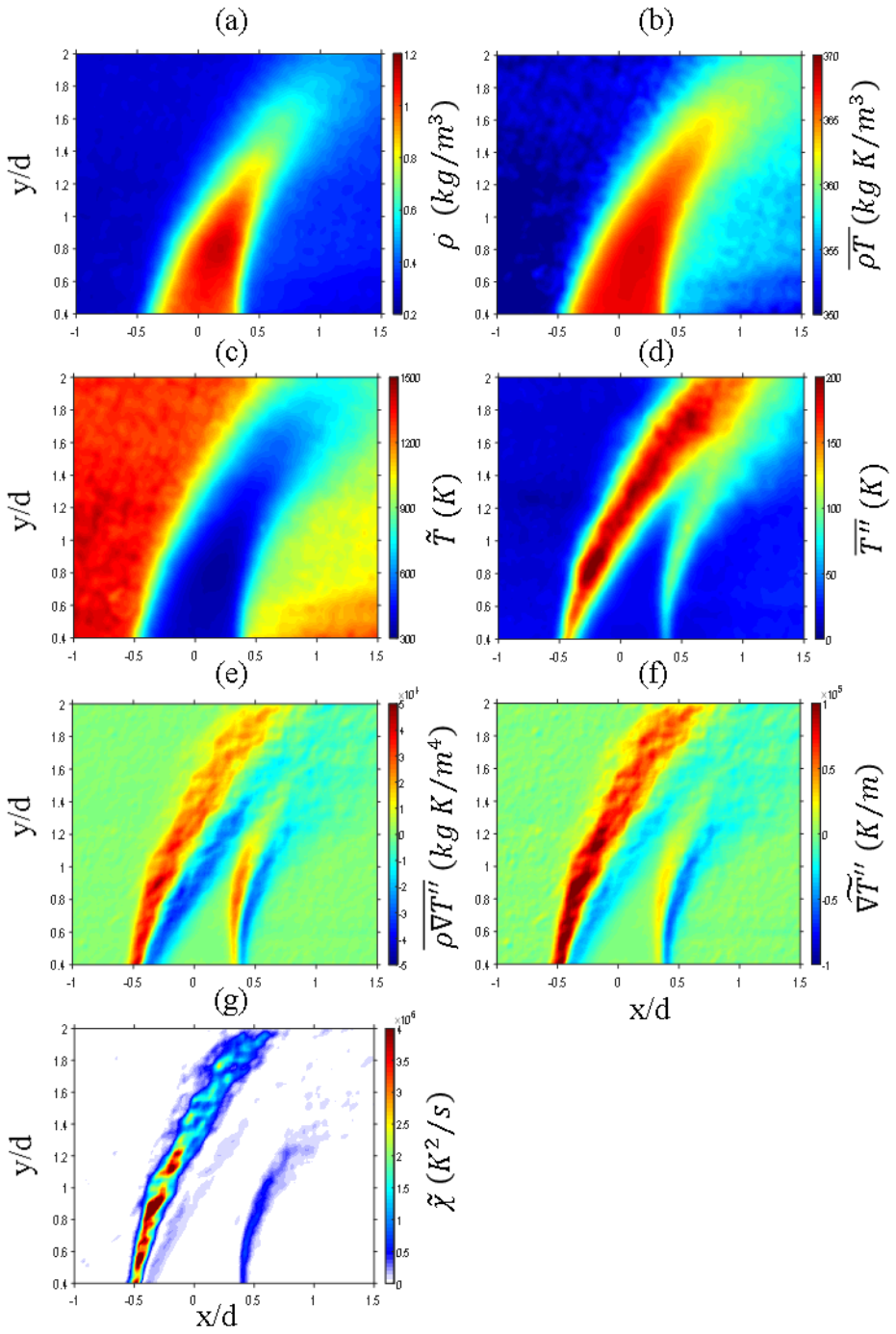

Fig. 4.7: Scalar dissipation calculation process. (a) Ensemble averaged density field. (b) Ensemble average of product of instantaneous density and temperature fields. (c) Favre averaged temperature field. (d) Ensemble averaged temperature fluctuation field. (e) Ensemble average of the product of the instantaneous density and fluctuation gradient fields. (f) Favre averaged temperature fluctuation field. (g) Favre averaged scalar dissipation field.

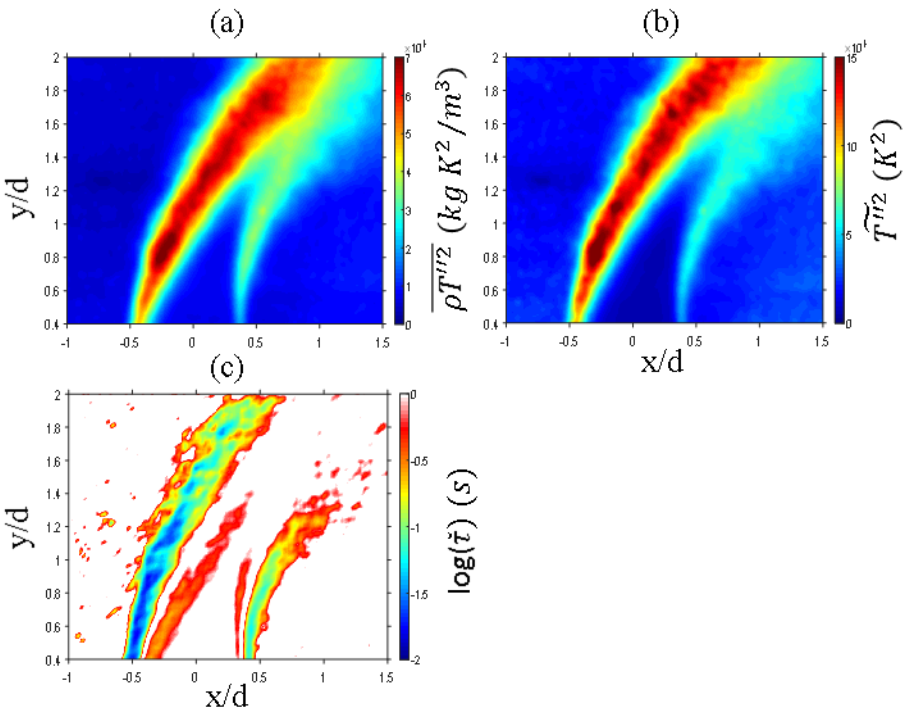

Fig. 4.8: Mixing time scale calculation process. (a) Ensemble average of the product of the density and temperature fluctuation variance fields. (b) Favre averaged temperature fluctuation variance field. (c) Favre averaged mixing time scale, shown in log scale.

4.5 Determination of Jet Centerline

A common method of defining the jet centerline is using the locus of points at which the maximum jet concentration value occurs on the local jet-normal line, as done by Smith and Mungal [4]. Adaptations of this method have been performed, as the one presented by Gevorkyan et al. [8], where the maximum jet concentration values along an image column are first fit to a power law and then iteratively processed to find the maximum jet concentration along the local-normal line. While these methods have been proven to be successful for view windows of 0 - 70d [4] and -5 – 15d [8] in the x-direction, issues of trajectory divergence from centerline when iterating for local-normal maximum points arise in the view window presented here (-1 – 1.7d). To mitigate these issues, a geometric method of determining the jet centerline was implemented.

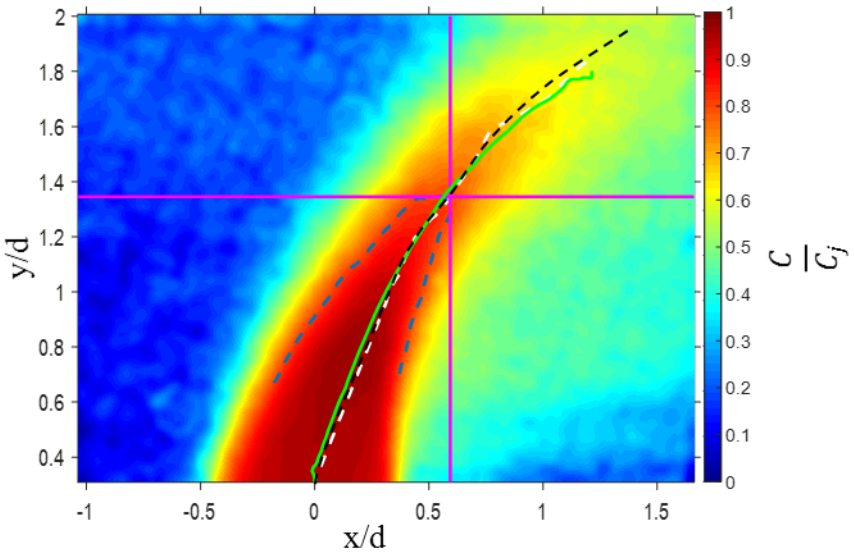

Fig. 4.9: Geometric method for determination of jet centerline trajectory.

As discussed in Section 4.3, the crossflow mixture fraction was determined from the LRS images to obtain temperature. By the definition used for crossflow mixture fraction, a calculated normalized jet concentration, C/C_j, can be determined by the subtracting the crossflow mixture fraction from one, resulting in $C/C_j \approx Y_j/Y_{j,0}$ where Y_j is the local mass fractions of jet fluid species in the mixture and $Y_{j,0}$ is the mass fractions of jet fluid species at the jet exit. Upon investigation of a calculated average jet concentration field as shown in Fig. 4.9, the jet trajectory imagined would be along the jet center and through the center of the profiles of the concentration contours, depicted as the dotted black line in Fig. 4.9. However, since the jet is bent, the center of the profiles are on the local-normal plane, as already stated in [4] and [8], and cannot be directly determined. When looking at the contour of a specific concentration percentage, calculated by binarizing the calculated concentration field using a concentration threshold, C, (% < C = 0, % > C = 1), the profile was noticed to resemble an elliptic arc. The contour of C = 80% is highlighted as a blue dotted line in Fig. 4.9. By using the horizontal and vertical tangents of the arc, defined

as the tangents to the maximum x- and y-coordinates on the contour, the center of the profile was estimated as the intersection of the two tangent lines. The tangent lines for the C = 80% contour are depicted as the pink lines in Fig. 4.9. This process was performed for concentration values of 60-95% in steps of 1%. The lower bound was chosen due to the mixing noise at values lower than 60%, resulting in shapes not applicable to this method. To mitigate further errors due to the jet being less bent at higher J values, resulting in wide contours near the jet exit in the x-direction, the edges closer to the jet exit in the y-direction of the binarized contours were ignored. The resulting line of the tangent method is shown in Fig. 4.9 as the white dotted line. While this method produces results very close to the imagined jet trajectory, it is not related to the definition of jet centerline trajectory used by other researchers. Therefore, the resulting line from the tangent method was used as the baseline to determine the local-normal planes along the jet center. The true jet centerline trajectory was then determined by taking the maximum jet concentration point on each local-normal plane calculated from the tangent method line, similar to that done in [8], however, only a single iteration for the local-normal plane was needed for convergence of the jet centerline trajectory. The final trajectory is shown as the lime green line in Fig. 4.9.

5. Near Field JICF Mixing Characteristics

As discussed in Section 1.3, laser Rayleigh scattering was used to visualize the temperature field of the non-reacting jet in the hot, vitiated crossflow. Using the recorded temperature fields, center-plane mixing characteristics of a JICF are investigated. In Section 5.1, the obtained temperature fields for various momentum flux ratios, density ratios, and jet velocity profiles are shown. Sections 5.2 and 5.3 use the jet centerline to evaluate different mixing characteristics. In Section 5.4, the mixing intensity and timescale are investigated using the concepts of scalar dissipation described in Section 2.2.

5.1 LRS Temperature Fields

Fig. 5.1 and Fig. 5.2 show the ensemble averaged temperature fields, averaged over 400 LRS images, for each velocity profile: turbulent pipe (Pipe), top-hat (TH), and 40% turbulent intensity (40% TI). The resulting temperature fields for three momentum flux ratios of J = 7.0, 12.6, and 18.0, at a density ratio of s = 5.32 are shown in Fig. 5.1. Temperature fields for J = 12.6 at two density ratios of s = 5.32, and 3.19 are shown in Fig. 5.2.

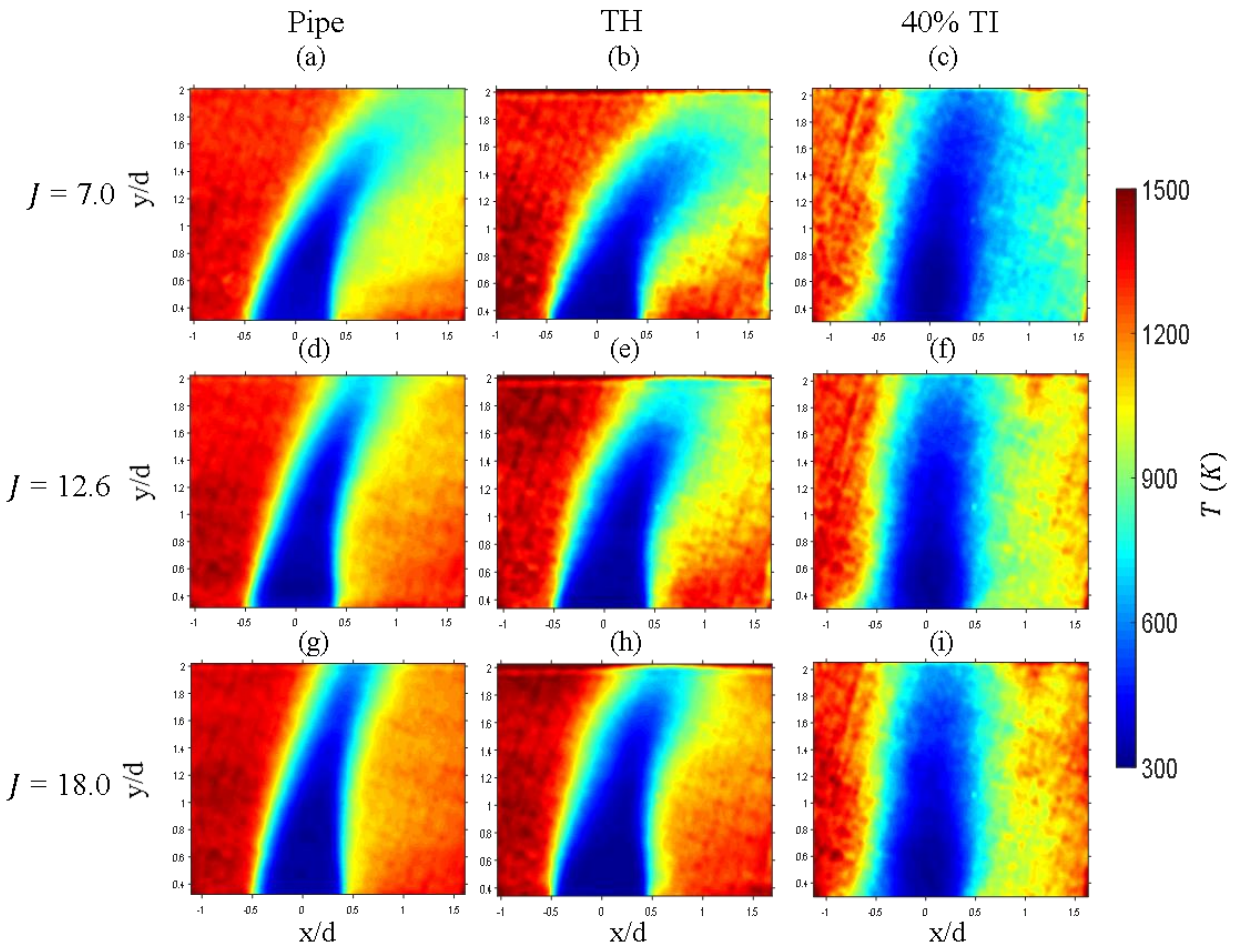

Fig. 5.1: Ensemble averaged temperature fields for density ratio *s* = 5.32. Data shown for varying momentum flux ratios *J* = 7.0 (a-c), 12.6 (d-f), and 18.0 (g-i) for varying jet velocity profiles; Pipe profile shown in (a), (d), and (g), Top-Hat (TH) profile shown in (b), (e), and (h), and 40% Turbulent Intensity (40% TI) profile shown in (c), (f), and (i).

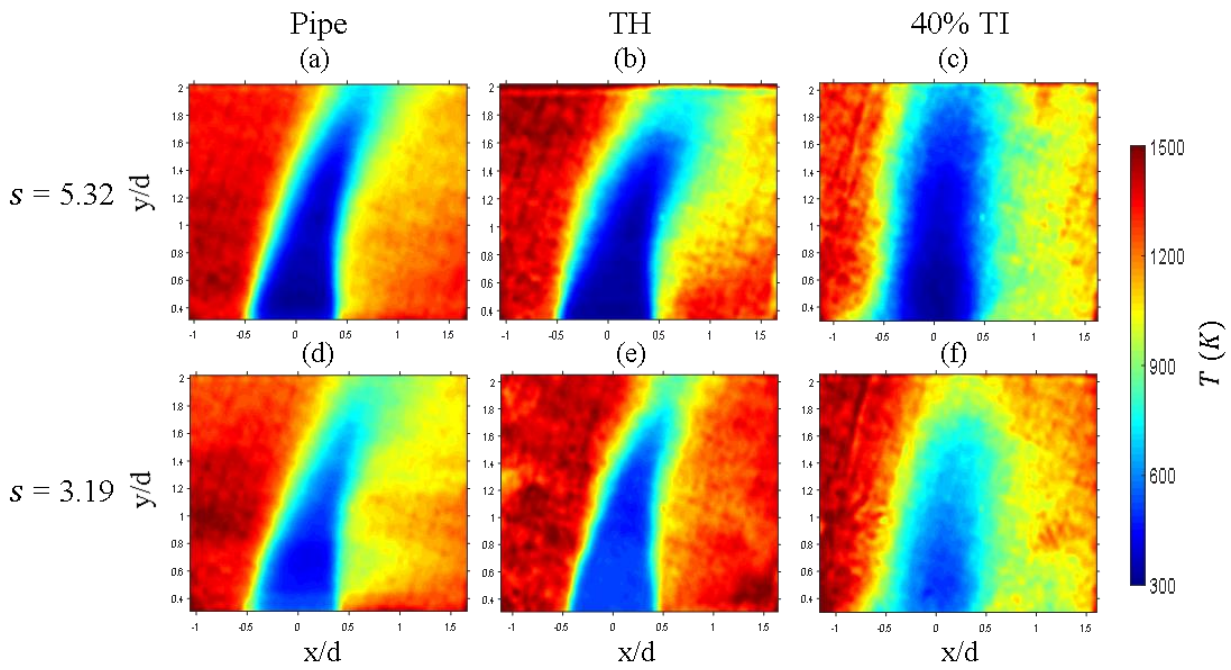

Fig. 5.2: Ensemble averaged temperature fields for momentum flux ratio J = 12.6. Data shown for two density ratios of s = 5.32 (a-c) and 3.19 (d-f) for different jet velocity profiles; Pipe profile shown in (a) and (d), Top-Hat (TH) profile shown in (b) and (e), and 40% Turbulent Intensity (40% TI) profile shown in (c) and (f).

As can be seen in Fig. 5.1, as the momentum flux J is increased, jet bending in the direction of the crossflow decreases and the jet core concentrations persist to longer downstream distances for the pipe and top-hat profiles and to a lesser extent for the 40% turbulence case, which shows less trajectory sensitivity to J. In general, the top-hat profile exhibits a similar trajectory to the pipe profile, but with a wider potential jet core region. Windward mixing layer temperatures appear to be similar for the pipe and top-hat profiles for the three momentum flux ratios, however, the leeward region of the jet exhibits variations with increasing J values, with more mixing between jet and the crossflow being present for the lower J values, as indicated by the lower temperatures. This effect is attributed to the decrease in near field vortex shedding at higher values of J. The leeward mixing of the top-hat profile appears to be less sensitive to the change in momentum flux ratio, indicated by the lower temperatures downstream compared to

those of the pipe profile. The mixing characteristics of the 40% turbulence case are significantly different than the pipe and top-hat profiles. The mixing layers on both windward and leeward sides are wider indicating more vigorous mixing due to higher degree of turbulence in the jet. However, similar to the pipe and top-hat profiles, the 40% turbulence case exhibits a decrease in downstream mixing with increasing values of J.

As can be seen in Fig. 5.2, for a constant momentum flux ratio, as the density ratio s is decreased, the jet core length also decreases, as well as the downstream mixing. An exception to this is the pipe profile, where the lower value of s shows increased downstream mixing, indicated by the lower temperatures in the x = 0.5 - 1.5d downstream region. Looking at the different velocity profiles, an interesting observation is made that with a lower value of s, the top-hat temperature field begins to resemble a pipe temperature field in terms of jet core shape and mixing, indicating that the lower density ratio suppresses the effects of the stronger shear layer of the top-hat profile.

To gain a better understanding of the reasoning behind the observed differences in the temperature fields, Fig. 5.3 shows various instantaneous temperature fields at different instances in time for all jet velocity profiles at a momentum flux ratio of J = 12.6 and different density ratios. Images were chosen at random from each relevant data set. Images in Fig. 5.3 (a-f) are at density ratio of s = 5.32. Images in Fig. 5.3 (g-j) are at density ratio of s = 3.19. A selection of more instantaneous images from each test case can be found in the Appendix.

As can be seen in Fig. 5.3, the dynamics induced by the different velocity profiles are much different. Looking at the different velocity profiles at a density ratio of s = 5.32, the pipe profile induces a relatively smooth jet-to-crossflow interface with large-scale vortex rollups,

while the top-hat and 40% TI profiles induce small-scale vortices that entrain crossflow deeper into the jet core, visualized by the small pockets of heated jet fluid in the jet core, as well as inducing large-scale vortices that separate large portions of the jet from the jet core. As seen in Fig. 5.3 (c), the 40% TI velocity profile occasionally causes the jet to bend in the windward direction, an aspect of the flow dynamics not observed for the pipe or top-hat velocity profiles in any cases presented in this thesis.

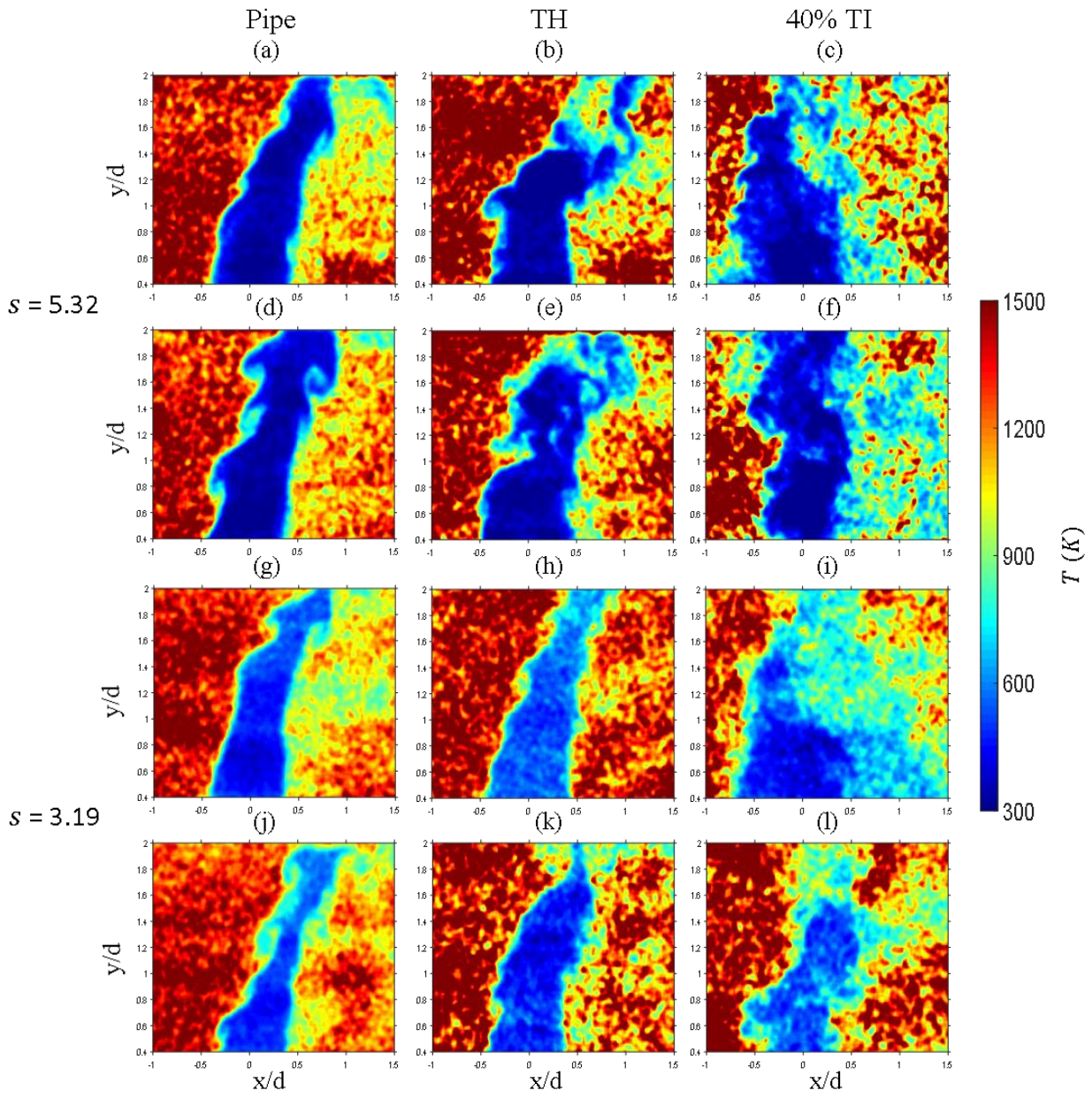

Fig. 5.3: Instantaneous temperature field for momentum flux ratio J = 12.6. Data shown for varying density ratios s = 5.32 (a-f) and 3.19 (g-l) for varying jet velocity profiles; Pipe profile shown in (a), (d), (g), and (j), Top-Hat (TH) profile shown in (b), (e), (h), and (k), and 40% Turbulent Intensity (40% TI) profile shown in (c), (f), (i), and (l).

Looking at the lower density ratio images in Fig. 5.3, the effect of a lower value of s is to reduce the strength of the vortical roll-ups as compared to the higher density ratio images. As mentioned above, at a lower value of s, the ensemble averaged temperature profile for top-hat profile resembles that of the pipe profile. Looking at Fig. 5.3 (h) and (k), the effect of lowering s for the

top-hat profile is that the flow dynamics appear to change drastically as compared to the s = 5.32 images. The instantaneous jet images resemble that of the pipe profile, where a smoother jet-to-crossflow interface is observed, with vortex rollups being visible along the windward edge.

5.2 Concentration Trajectory

While qualitative observations were made on the jet trajectory from the ensemble averaged temperature fields, the jet centerline trajectory was determined using the ensemble average calculated concentration field, as described in Section 4.5. The resulting trajectories were smoothed for plotting and are shown in Fig. 5.4, Fig. 5.5, and Fig. 5.6 with the comparison of jet trajectories between the three different jet velocity profiles at different momentum flux ratios being shown in Fig. 5.4, the comparison of jet trajectories at a momentum flux ratio of J = 12.6 at different density ratios being shown in Fig. 5.5, and the comparison of different scaling of the trajectories shown in Fig. 5.6. The x-scale in Fig. 5.4 and Fig. 5.5 are not the same for each velocity profile to show the differences between each case for that specific jet exit velocity profile. All trajectories shown only extend to vertical and downstream distances within the experimetnal viewing window.

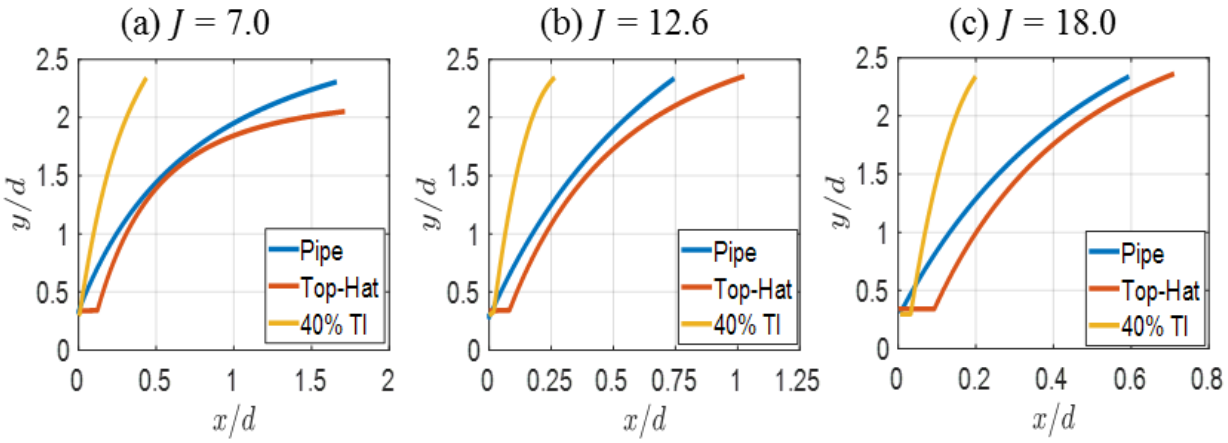

Fig. 5.4: Jet concentration trajectories for density ratio s = 5.32 with multiple jet velocity profiles. Data shown for various momentum flux ratios (a) J = 7.0, (b) J = 12.6, (c) J = 18.0. Trajectories are scaled with the jet diameter d.

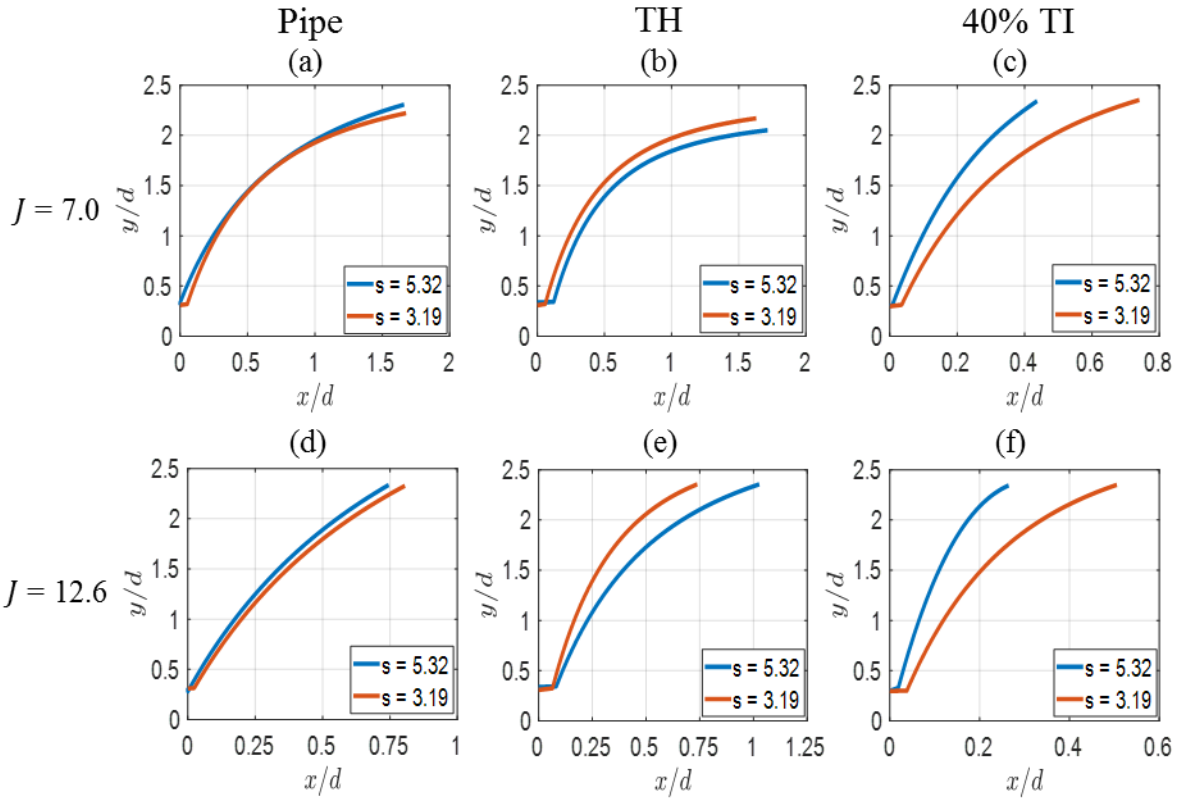

Fig. 5.5: Jet concentration trajectories with various density ratios. Data shown for varying momentum flux ratios J = 7.0 (a-c) and 12.6 (d-f) for varying jet velocity profiles; Pipe profile shown in (a) and (d), Top-Hat (TH) profile shown in (b) and (e), and 40% Turbulent Intensity (40% TI) profile shown in (c) and (f). Trajectories are scaled with the jet diameter d.

As can be seen in Fig. 5.4, and mentioned previously, the pipe and top-hat jet exit flows produce very similar jet trajectories for all values of momentum flux ratios, with the top-hat profile exhibiting a more downstream bending, particularly at a momentum flux ratio of J = 7.0, indicating a shorter penetration. Unlike the pipe and top-hat profiles, the 40% TI profile results in a less bent trajectory for all values of J. As can be seen in Fig. 5.5, for the pipe velocity profile, the change in density ratio does not affect the jet trajectory tremendously. For the top-hat and 40% TI profiles, some differences are observed as the density ratio is increased. For instance, the top-hat jet trajectory for a lower value of s shows a slightly deeper penetration, which is more visible at a momentum flux ratio of J = 12.6. Interestingly, this observation is a contradiction to the findings of Gevorkyan et al. [8] where the observation was made that as the density ratio increased, the penetration also increased. As for the 40% TI profile, as s decreases, the penetration also decreases.

As discussed in Section 1.2.2.1, many studies have been performed to determine the best scaling quantity for JICF trajectories. Fig. 5.6 illustrates the different scaling methods often used for JICF studies. The major difference in the scaling methods presented here is that most trajectories are scaled using the velocity ratio, r, due to an equidensity jet, as in [4] and [6], however, due to the non-unity density ratios used in this thesis, the trajectories are scaled using the momentum flux ratio, J, as in [5] and [8]. The $\sqrt{J}d$ scaling is similar to the rd scaling used by Smith and Mungal [4], since by definition $\sqrt{J}d = \sqrt{s}rd$. The difference here is the density ratio within the scaling, which is necessary here since as observed in Fig. 5.5 the trajectory is altered with increasing s for the top-hat and 40% TI velocity profiles. As can be seen in Fig. 5.6, a single scaling quantity did not provide adequate collapse of all data for all velocity profiles. In the figure, it is observed that the $\sqrt{J}d$ scaling is relatively sufficient to collapse the data for the

top-hat, Fig. 5.6 (h), velocity profile, with only a slight variation for increasing values of J. However, for the pipe and 40% turbulence intensity profiles, the use of a $\sqrt{J}d$ scaling seems to show more divergence from a perfect collapse; the trajectories for J = 12.6 and 18.0, a collapse is observed, however, the J = 7.0 trajectory deviates downstream. Looking at Fig. 5.6, the best scaling to collapse the pipe data is the Jd scaling, Fig. 5.6 (g). A good collapse of data is not seen for the 40% turbulence intensity profile with any of the scales presented here. The Jd scaling is consistent with the observations of Gevorkyan et. al. [8] and Keffer and Baines [6], for an equidensity JICF. In [8], the trajectories were defined by concentration as presented here, while in [6] the trajectories were defined by center streamlines. It should be noted that the view window presented here is much smaller than that in [8] and [6], and therefore the observation of better scaling with Jd for the pipe profile and $\sqrt{J}d$ for the top-hat profile is only valid within this small observation window.

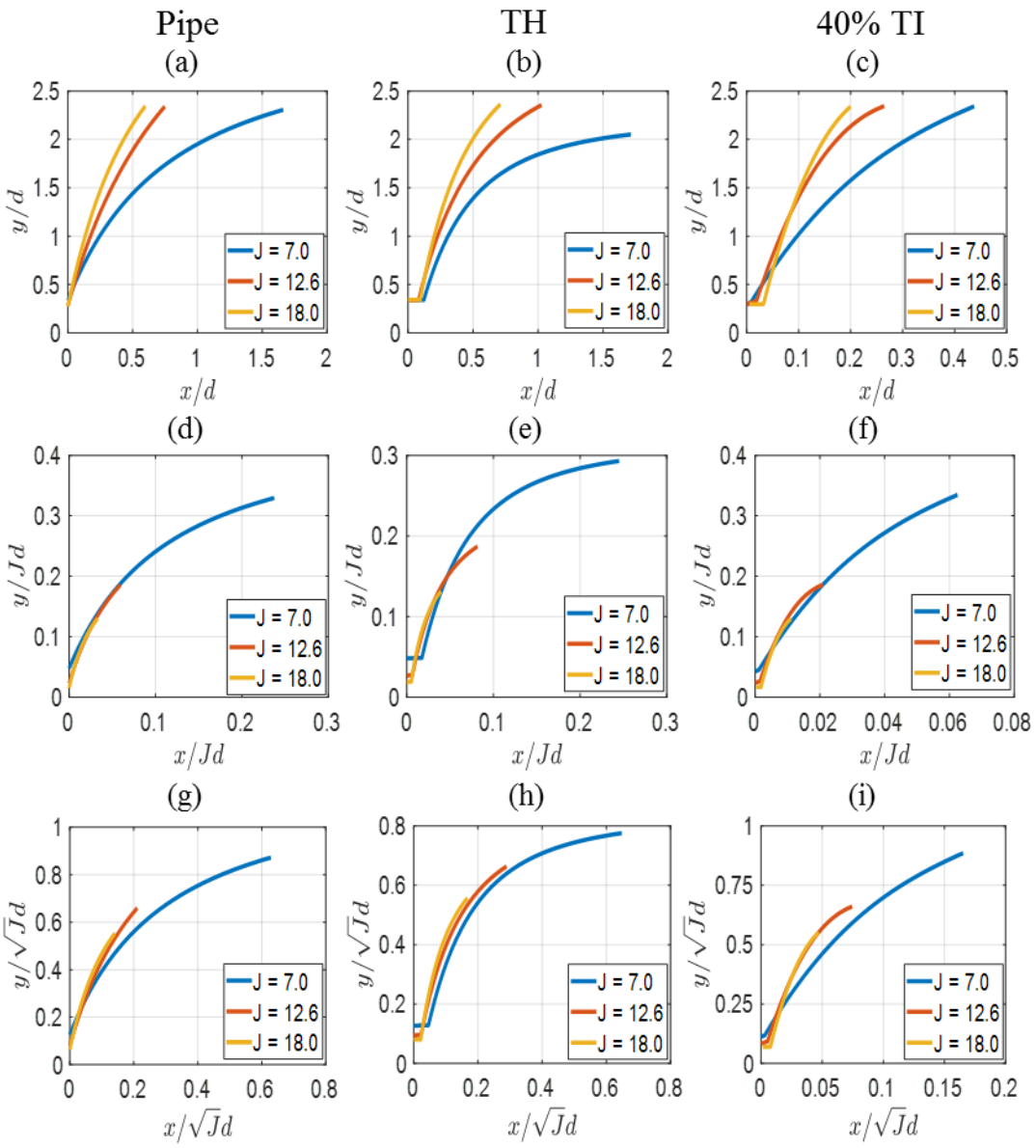

Fig. 5.6: Jet concentration trajectories for density ratio s = 5.32 with various momentum flux ratios. Data shown for varying jet velocity profiles; Pipe profile shown in (a), (d), and (g), Top-Hat (TH) profile shown in (b), (e), and (h), and 40% Turbulent Intensity (40% TI) profile shown in (c), (f), and (i). Trajectories are scaled using multiple length scales; d (a-c), Jd (d-f), and $\sqrt{J}d$ (g-i).

In Fig. 5.6 (a-c), the effect of momentum flux ratio on jet trajectory is best observed. In general, as the momentum flux ratio J is increased, the jet penetrates deeper into the crossflow. This is consistent with the findings of Smith and Mungal [4], Keffer and Baines [6], and Gevorkyan et al. [8], as well as the qualitative observations made in Section 5.1 from the

ensemble averaged temperature fields. Also consistent with the observations made in Section 5.1, is that for the 40% TI velocity profile, the jet trajectory for different momentum flux ratios is relatively the same, with only a slight increase in penetration as J increases.

For the top-hat velocity profile, a very interesting observation can be seen in Fig. 5.6 (b). For all momentum flux ratios presented, it is observed that the concentration trajectory is offset from the center of the jet exit by approximately $0.1d$. This phenomenon would indicate that crossflow fluid is entrained into the jet exit on the windward edge. Megerian et al. [35] observed strong shear layer instabilities near the jet exit for a flush and elevated nozzle with a similar velocity profile to the one used here. Their conclusions were that a negative flow into the nozzle is produced by a hovering vortex structure that exists above jet the exit [35].

5.3 Mean Centerline Concentration Decay

To aid in quantify mixing differences between different jet velocity profiles, momentum flux ratios, and density ratios, the centerline decay of the calculated jet concentration is investigated. The centerline concentration decay is a simplistic measure of crossflow entrainment. As the jet entrains crossflow fluid, the mean jet concentration decreases along the jet centerline.

Lines with slopes of $S^{-1.6}$, S^{-1}, $S^{-1.3}$, and $S^{-2/3}$ are shown on all centerline concentration decay plots, representing the trends in centerline decay observed by Gevorkyan et. al. [8], Su and Mungal [7], and Smith and Mungal [4] respectively. The differences of centerline concentration decay between each jet velocity profile for various momentum flux ratios, J, is shown in Fig. 5.7.

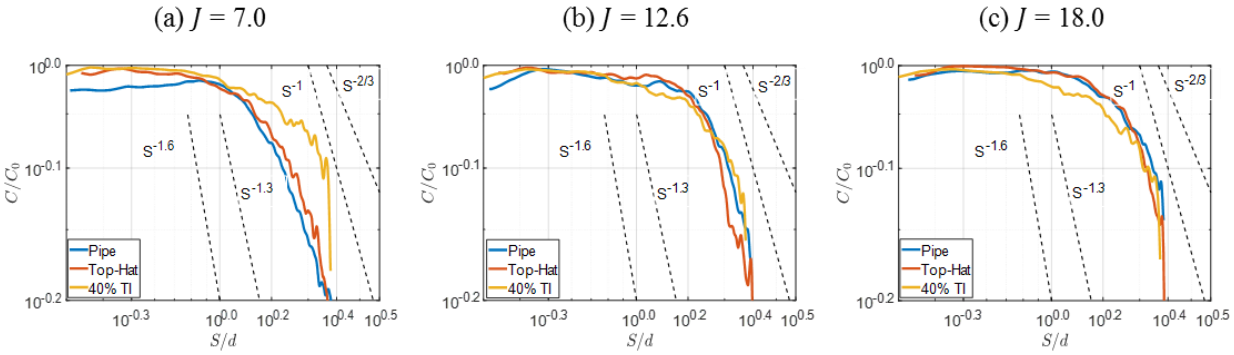

Fig. 5.7: Jet centerline concentration decay for density ratio s = 5.32 with multiple jet velocity profiles. Data shown for various momentum flux ratios (a) J = 7.0, (b) J = 12.6, (c) J = 18.0. The jet centerline concentration decays are scaled with the jet diameter d.

As can be seen in Fig. 5.7, the top-hat and pipe velocity profiles exhibit similar centerline concentration decays for all values of momentum flux ratio, J, with the top-hat having slightly faster decay rates. This is the opposite of the results found in [8]. However, these differences can be attributed to the "extreme" near field view presented here, while the view field in [8] was up to 15d downstream. The 40% TI velocity profile exhibited a much slower concentration decay rate as compared to the pipe and top-hat velocity profiles for J = 7.0.

Similar to the jet trajectories presented in Section 5.2, the centerline concentration decay was scaled using d, Jd, and $\sqrt{J}d$ in an attempt to collapse all decay lines. Fig. 5.8 shows the centerline concentration decay for various momentum flux ratios at a constant density ratio of s = 5.32 for all three velocity profiles with various scaling. As can be seen in Fig. 5.8, no single scaling provided adequate data collapse for any of the concentration decays.

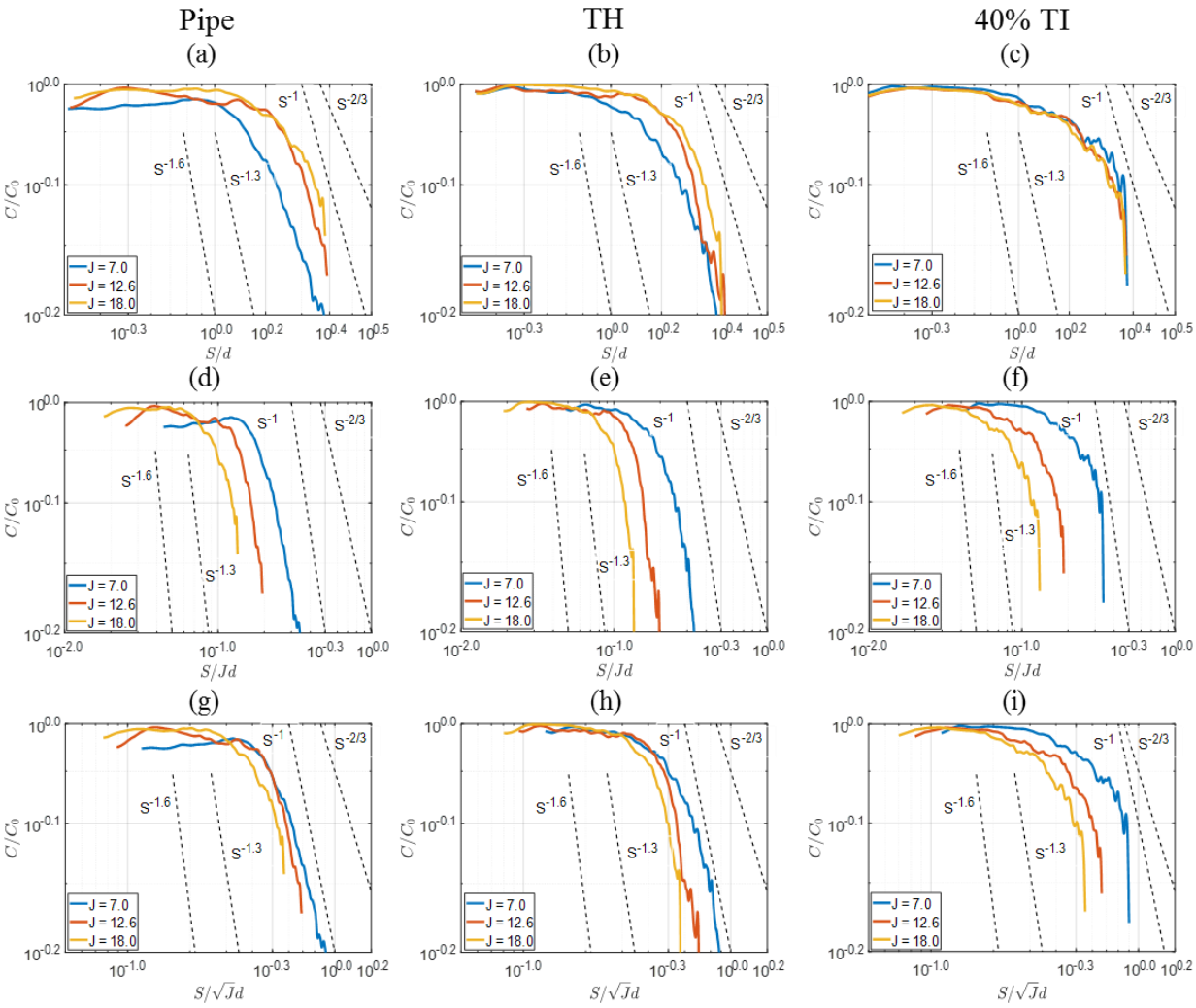

Fig. 5.8: Jet centerline concentration decay for density ratio s = 5.32 with various momentum flux ratios. Data shown for varying jet velocity profiles; Pipe profile shown in (a), (d), and (g), Top-Hat (TH) profile shown in (b), (e), and (h), and 40% Turbulent Intensity (40% TI) profile shown in (c), (f), and (i). The jet centerline concentration decays are scaled using multiple length scales; d (a-c), Jd (d-f), and $\sqrt{J}d$ (g-i).

The pipe velocity profile exhibited a decay between S^{-1} and $S^{-2/3}$, with larger values of momentum flux decaying slower. The top-hat velocity profile also exhibited a decay between S^{-1} and $S^{-2/3}$, with larger values of momentum flux decaying slower. As for the 40% TI profile, the centerline concentration decays close to $S^{-2/3}$ for all momentum flux ratios presented here. The observations of the decrease in concentration decay rate with increasing momentum flux ratio is in agreement with the findings in [8], [4], and [7]. In Fig. 5.9, the concentration decay for

various density ratios at a momentum flux ratio of J = 7.0 and 12.6 for all three velocity profiles are shown.

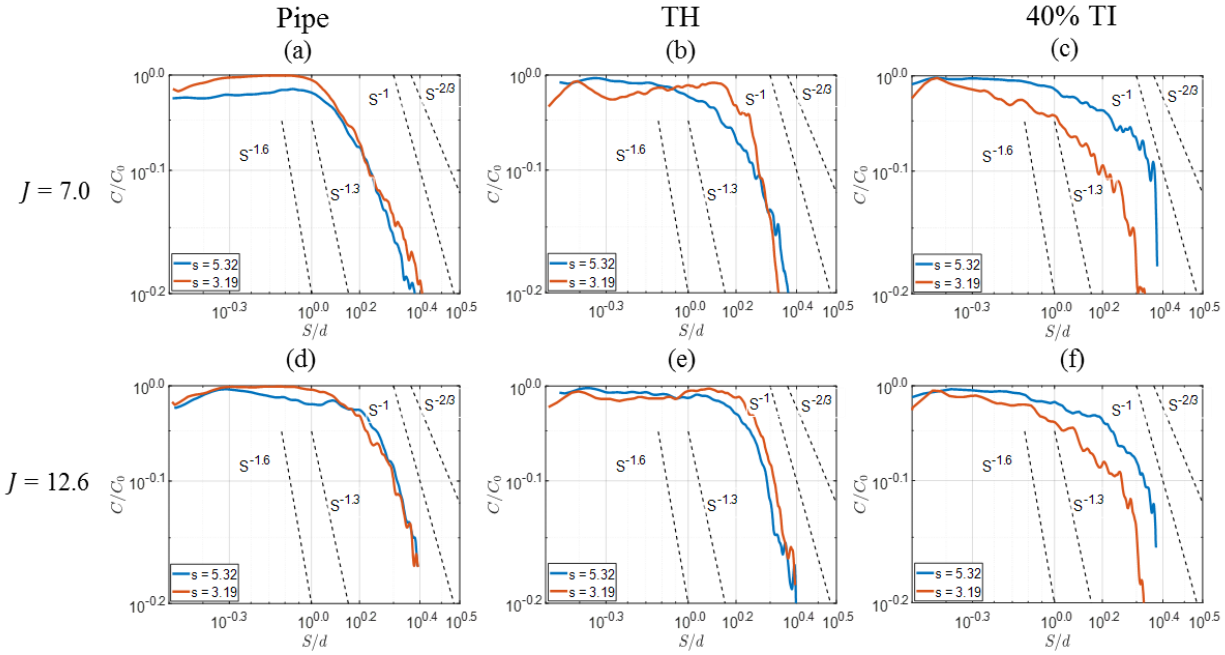

Fig. 5.9: Jet centerline concentration decay with various density ratios. Data shown for varying momentum flux ratios J = 7.0 (a-c) and 12.6 (d-f) for varying jet velocity profiles; Pipe profile shown in (a) and (d), Top-Hat (TH) profile shown in (b) and (e), and 40% Turbulent Intensity (40% TI) profile shown in (c) and (f). The jet centerline concentration decays are scaled with the jet diameter d.

As can be seen in Fig. 5.9, in general, for all velocity profiles, the centerline concentration decays faster as the density ratio increases. This observation is consistent with the findings in [8], however, the decay rates described above are slower than those presented in [8] with the density ratios here being greater than those in [8]. This difference is most likely due to the "extreme" near field view presented here as compared to [8]. An interesting observation is that the top-hat profile shows a faster decay rate at a lower density ratio, s, at a lower momentum flux ratio. Looking at the 40% TI profile, a longer jet core is seen for larger values of s; an artifact not seen with the pipe or top-hat profiles.

5.4 Scalar Dissipation and Mixing Timescale

To further investigate the mixing characteristics of the JICF, the temperature field data was used to determine a Favre average scalar dissipation rate, $\tilde{\chi}$, and mixing timescale, $\tilde{\tau}$, field. Similar to turbulent kinetic energy dissipation, scalar dissipation is a measure of the speed of destruction of scalar "energy" with large and small values of $\tilde{\chi}$ indicating large-scale, fast mixing and well mixed at the molecular level respectively. Small values of $\tilde{\chi}$ can also be an indication of a laminar flow field, since $\tilde{\chi}$ is dependent on scalar fluctuations, as described in Section 2.2. The differences in the Favre averaged scalar dissipation field for different momentum flux ratios at a density ratio of s = 5.32 for all three jet velocity profiles is shown in Fig. 5.10. The differences in the Favre averaged scalar dissipation field for different density ratios at a momentum flux ratio of J = 12.6 for all three jet velocity profiles is shown in Fig. 5.11. It should be noted that the use of the density-weighted Favre averaging scales the $\tilde{\chi}$ field such that the mixing between the jet and crossflow is emphasized while the gradients within the crossflow are minimized.

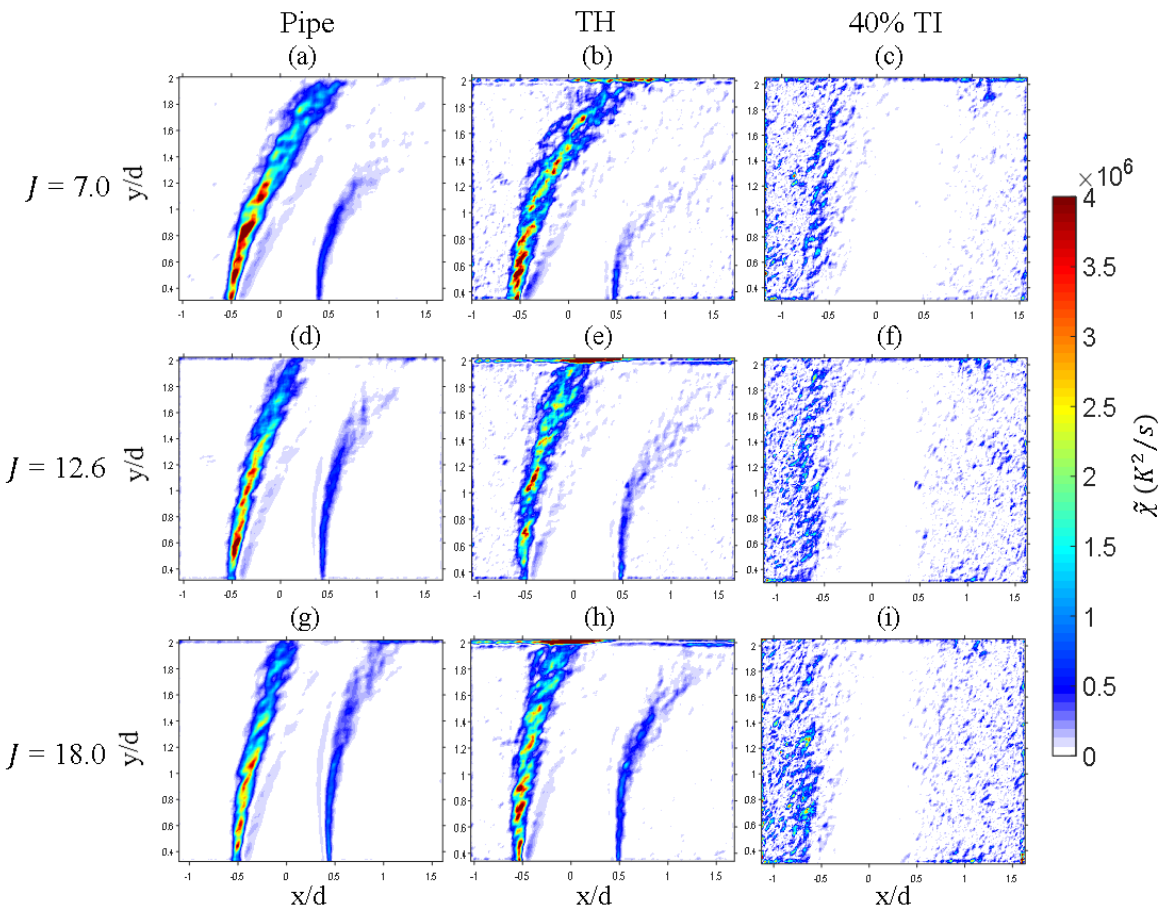

Fig. 5.10: Favre averaged scalar dissipation fields $\tilde{\chi}$ for density ratio s = 5.32. Data shown for varying momentum flux ratios J = 7.0 (a-c), 12.6 (d-f), and 18.0 (g-i) for varying jet velocity profiles; Pipe profile shown in (a), (d), and (g), Top-Hat (TH) profile shown in (b), (e), and (h), and 40% Turbulent Intensity (40% TI) profile shown in (c), (f), and (i).

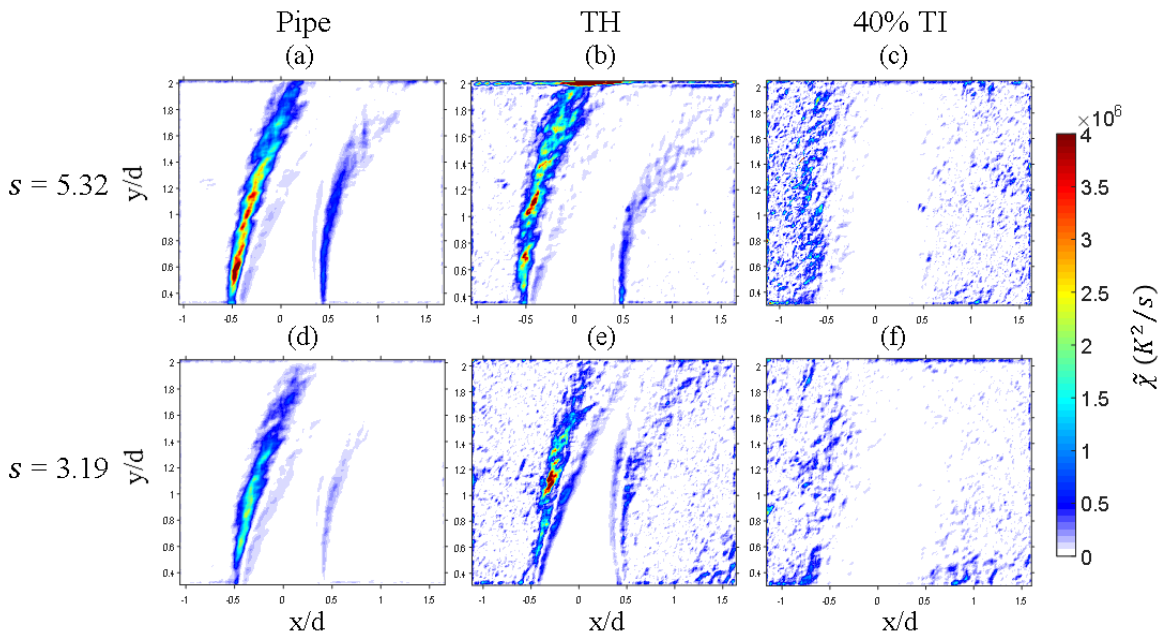

Fig. 5.11: Favre averaged scalar dissipation fields $\tilde{\chi}$ for momentum flux ratio J = 12.6. Data shown for varying density ratios s = 5.32 (a-c) and 3.19 (d-f) for varying jet velocity profiles; Pipe profile shown in (a) and (d), Top-Hat (TH) profile shown in (b) and (e), and 40% Turbulent Intensity (40% TI) profile shown in (c) and (f).

As can be seen in both Fig. 5.10 and Fig. 5.11, large values of $\tilde{\chi}$ are observed on the shear layer on the windward edge and relatively lower values of $\tilde{\chi}$ on the leeward shear layer for the pipe and top-hat velocity profiles. This is to be expected since for these two velocity profiles, for instantaneous temperature field images showed a clear jet-to-crossflow boundary that exhibit large-scale and small-scale vortex rollups and temperature gradients. Smaller areas of low scalar dissipation are also observed on the inside of the shear layers. These smaller areas are due to the negative temperature fluctuation gradient shown in Fig. 4.7 (g). Directly comparing the pipe and top-hat velocity profiles for each value of momentum flux ratio J, the windward scalar dissipation region is greater in size for the top-hat velocity profile. This can be attributed to the stronger shear layer exhibited by the top-hat velocity profile which causes larger temperature fluctuation gradients. The top-hat velocity profile also exhibits smaller patches of large values in

the scalar dissipation field of the windward dissipation region. These patches can be attributed to the lack of large scale vortex rollups for this profile compared to the pipe profile.

Unlike the pipe and top-hat velocity profiles, the 40% TI profile results in a scalar dissipation field with small regions of low magnitude scattered upstream and downstream of the jet. This is not surprising based on the observations of the instantaneous temperature field, where no clear jet-to-crossflow boundary is present and jet fluid is shed from the jet core in all directions into the crossflow.

Looking at the scalar dissipation fields for different momentum flux ratios at a constant density ratio of s = 5.32 shown in Fig. 5.10, some noticeable differences are observed. For instance, the intensity of scalar dissipation in the windward dissipation region decreases as the momentum flux, J increases. As mentioned in Section 5.1, the near field shear layer vortex rollups are suppressed with increasing J. This flow dynamics effect in turn decreases the magnitude of scalar dissipation in the windward side. When looking at the leeward dissipation region, an interesting trend appears. As J increases, the leeward dissipation region increases in size and intensity. A possible explanation for this trend is that as J increases, the leeward shear layer becomes stronger, leading to less interaction between the jet and wake vortices, creating a larger temperature gradient between the jet and crossflow. The effect of density ratio on the scalar dissipation field for a constant momentum flux J = 12.6, is shown in Fig. 5.11. As can be seen in the figure, as density ratio, s, decreases, the dissipation region area and dissipation intensity decrease. As discussed in Section 5.1, as s decreases a suppression of large-scale shear layer vortices is observed. In [36], Brown and Roshko note that in a turbulent mixing layer, entrainment is a process of "entanglement" of large-scale structures, and so a decrease in shear layer vortices would decrease the overall mixing in the dissipation layer.

Fig. 5.12 and Fig. 5.13 are visualizations of the Favre averaged scalar mixing time scale. In Fig. 5.12, the scalar mixing time scale field is shown for different momentum flux ratios with a constant density ratio of s = 5.32 for all three jet velocity profiles. In Fig. 5.13, the scalar mixing time scale field is shown for different density ratios for a constant momentum flux ratio J = 12.6 for all three jet velocity profiles. Both figures are shown in logarithmic scale.

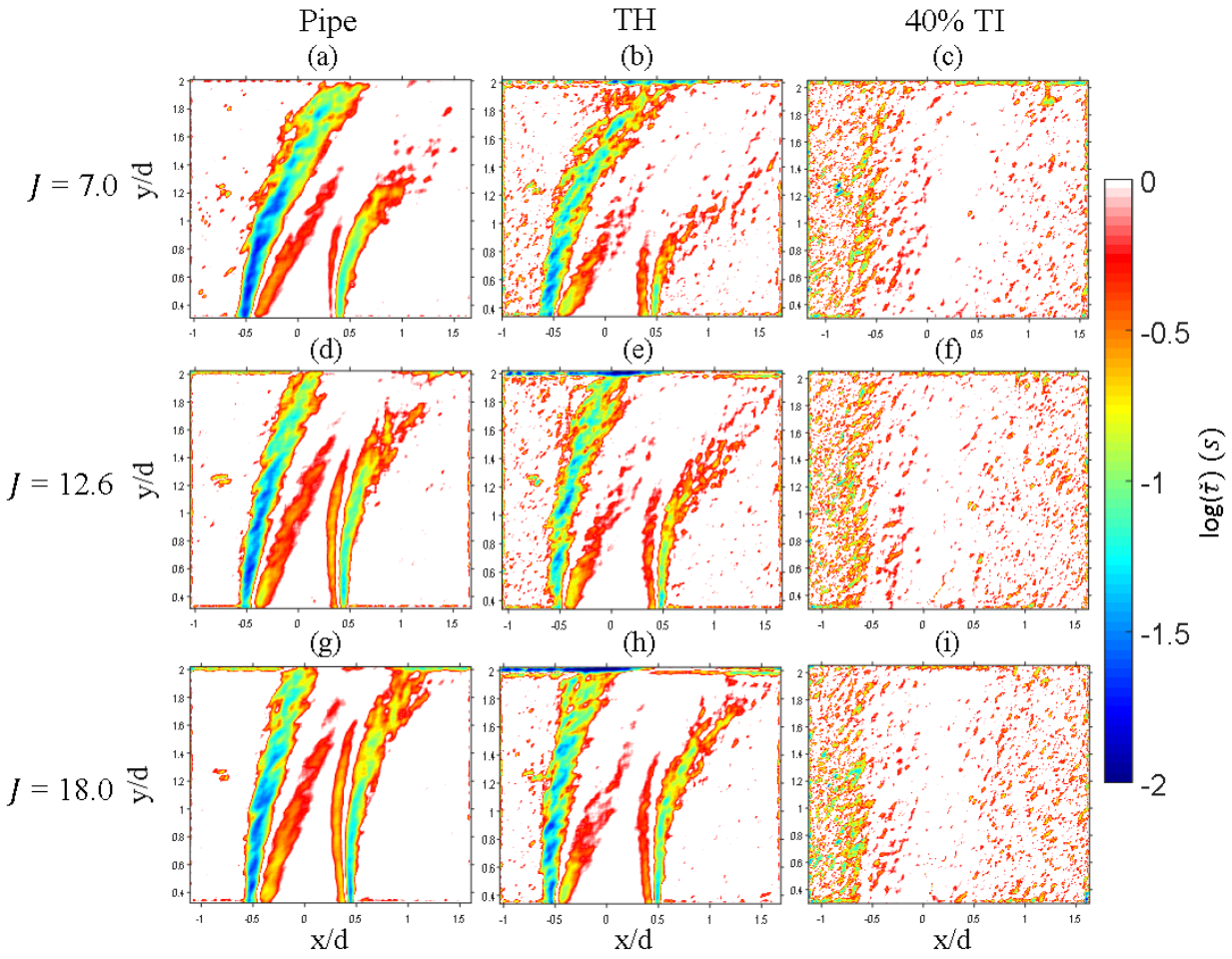

Fig. 5.12: Favre averaged mixing time scale fields $\tilde{\tau}$ for density ratio s = 5.32. Data shown for varying momentum flux ratios J = 7.0 (a-c), 12.6 (d-f), and 18.0 (g-i) for varying jet velocity profiles; Pipe profile shown in (a), (d), and (g), Top-Hat (TH) profile shown in (b), (e), and (h), and 40% Turbulent Intensity (40% TI) profile shown in (c), (f), and (i). Values are log scaled.

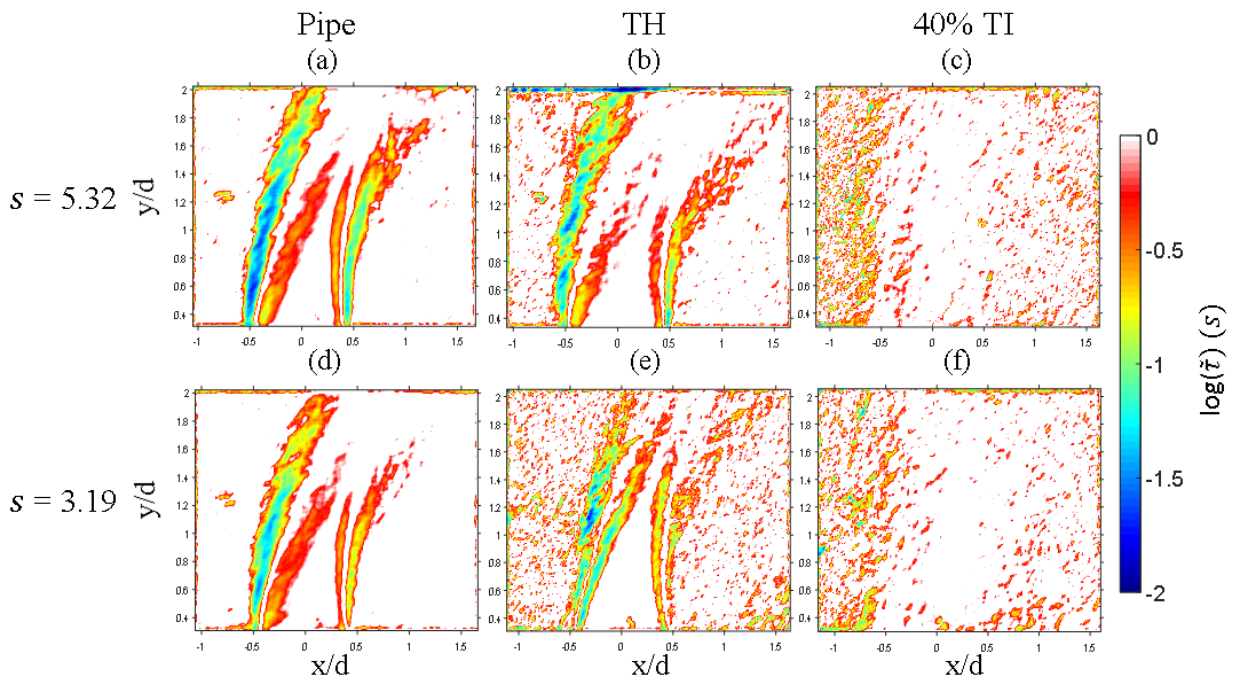

Fig. 5.13: Favre averaged mixing time scale fields $\tilde{\tau}$ for momentum flux ratio J = 12.6. Data shown for varying density ratios s = 5.32 (a-c) and 3.19 (d-f) for varying jet velocity profiles; Pipe profile shown in (a) and (d), Top-Hat (TH) profile shown in (b) and (e), and 40% Turbulent Intensity (40% TI) profile shown in (c) and (f). Values are log scaled.

As defined in Section 2.2, the Favre average mixing time scale, $\tilde{\tau}$, is inversely proportional to Favre average scalar dissipation, $\tilde{\chi}$, and therefore the trends discussed for the $\tilde{\chi}$ fields are directly related to the $\tilde{\tau}$ fields. Even though the scalar mixing time fields are essentially the equivalent of the inverse of the scalar dissipation fields, Fig. 5.12 and Fig. 5.13 are included to provide a visualization of the order of magnitude of the mixing time for each case. Looking at the pipe and top-hat velocity profiles, the scalar mixing time in the windward and leeward dissipation regions are on the order of 10ms and 100ms respectively. The presented scalar timescale for the 40% TI velocity profile is on the order of 1s, indicating slower mixing as compared to the pipe and top-hat velocity profiles. This is primarily a consequence of the low temperature and highly distributed gradients as seen in instantaneous temperature fields for this case. This low magnitude of scalar dissipation is connected with the high mixedness in this case.

6. Conclusions and Future Work

In the past several decades, research has been conducted on the injection of air into the crossflowing combustion products of a rich flame to rapidly quench the stream to a lean mixture for secondary burning in an attempt to reduce NO_x formation. More recently investigators have turned their focus to the study of utilizing premixed reacting jet-in-crossflow systems for the development of lean premixed combustors with axially controlled stoichiometry [10]. In these applications, the understanding of the mixing processes of the jet and crossflow is vital. For instance, in [10], for a rich premixed ethylene-air jet injected into a 1500K crossflow, flame branches were observed on both the windward and leeward jet edges, with the leeward flame remaining attached to the jet exit for a range of momentum flux ratios $J < 23$, while the windward flame base was consistently lifted for $J > 5$ [10]. The conclusions of this study were that the mechanism for flame stabilization was a result of the mixing between the premixed jet and the crossflow. In this thesis, the effect of jet-to-crossflow momentum flux ratio, J, jet-to-crossflow density ratio, s, and jet exit velocity profiles on scalar mixing of a jet in a hot vitiated crossflow were investigated using laser Rayleigh scattering (LRS) near the jet exit. Jet trajectory, centerline concentration decay, scalar dissipation, and scalar mixing time scales were explored to characterize these mixing characteristics.

To replicate a jet in a gas turbine combustor, a single non-reacting jet was ejected into the crossflow products of a lean propane-air swirl burner in a confined test section. The focus of the experimental set-up was on the mixing characteristics in the "extreme" near field, within two jet diameters, d, from the jet exit, with the intent on capturing the mixing characteristics close to the jet exit. From the acquired LRS images, the temperature field of the jet-in-crossflow (JICF) was obtained and used to determine all mixing metrics.

The ensemble averaged temperature fields obtained suggest that as the momentum flux ratio is increased at a constant density ratio, the downstream mixing of the jet and crossflow decreases in the "extreme" near field and the jet penetration increases. For a constant momentum flux ratio, as the density ratio is decreased, downstream mixing in the near field is also decreased, as well as the jet penetration. When comparing jet exit velocity profiles, the top-hat velocity profile exhibited similar mixing to the pipe velocity profile, with a slight increase in downstream mixing and a wider jet core. However, as the density ratio decreased, the top-hat profile resulted in a temperature field more closely resembling the pipe profile. When observing the instantaneous temperature field, the top-hat profile at a density ratio of s = 5.32 exhibited both small-scale and large-scale vortex structures throughout the flow field, that entrained crossflow fluid deep into the jet core, while also shedding large portions of jet fluid into the downstream crossflow. However, as the density ratio was decreased, the instantaneous top-hat temperature field more closely resembled the pipe profile with more large-scale shear layer vortex rollups being observed. The 40% turbulent intensity velocity profile exhibited a temperature field with deeper penetration than the pipe and top-hat velocity profiles as well as greater downstream and upstream mixing, especially close to the jet exit. When observing the instantaneous temperature field, the 40% turbulent intensity profile demonstrates jet ejection in the windward direction, an aspect not observed for the pipe or top-hat profiles. However, similar to the top-hat profile, the 40% turbulent intensity profile exhibited small-scale vortex structures that entrain crossflow fluid deep into the jet core and shed jet fluid in all directions.

In general, when comparing center-plane mixing metrics, better near field mixing is observed for lower values of the momentum flux ratio, J and larger values of density ratio, s. As the momentum flux ratio J is increased, the jet penetrates deeper in to the crossflow, reducing the

interaction between the jet shear layer rollups and the wake vortices in the "extreme" near field. This reduction in jet-to-crossflow mixing at larger momentum flux ratios results in a slower centerline concentration decay rate. When comparing different jet exit velocity profiles on mixing characteristics, the top-hat and pipe velocity profiles exhibit similar mixing, while the 40% turbulent intensity profile exhibited deeper jet penetration and slower centerline concentration decay rates. The similarities between the pipe and top-hat velocity profiles are believed to be due to the similar velocity profile shape, with the pipe having a shallow arc across the core, but with a similar boundary layer thickness to the top-hat velocity profile.

The Favre averaged scalar dissipation fields suggest that the intensity of scalar dissipation in the windward dissipation region decreases as the momentum flux, J, increases, while the leeward dissipation region increases in size and intensity as J increases. When the density ratio, s, is decreased, the windward and leeward dissipation regions decrease in size and magnitude. Observations of mixing regions on the inside of the shear layer as well as the outside were present. The inner mixing region was attributed to the negative temperature fluctuation gradient on the inner edge of the shear layer as the jet velocity decreases closer to the shear layer. When comparing the different velocity profiles, the windward scalar dissipation region was observed to be greater in size with small patches of large scalar dissipation values for the top-hat velocity profile, as compared to the pipe profile. As for the 40% turbulent intensity profile, the scalar dissipation field exhibited small regions of low magnitude scattered upstream and downstream of the jet with no clear dissipation region along the jet-to-crossflow interface as seen with the pipe and top-hat profiles. Looking at the Favre averaged scalar mixing time, the mixing in the windward and leeward dissipation regions are on the order of 10ms and 100ms respectively for the pipe and top-hat profiles, while the timescale for the 40% turbulence

intensity profile is on the order of 1s in the entire viewing field. The low mixing time and scalar dissipation of the 40% turbulence intensity profile are a consequence of the high mixedness in this case. In relation to the lean premixed combustor investigated in [10], these results would indicate that the regions of high scalar dissipation could potentially be too strong for flame stabilization, however, a reacting jet in crossflow mixing study would need to be performed to verify this.

The observations of the mixing characteristics presented here help provide a better insight into the mixing of a non-reacting jet in a hot vitiated crossflow. However, more in-depth studies should be performed to completely understand some of the observations made here. For instance, the use of laser Rayleigh scattering and particle image velocimetry (PIV), performed separately, along cross-sectional slices of the jet very close to the jet exit could potentially provide better insight into the mechanism behind the crossflow entrainment into the jet exit for the top-hat velocity profile, as well as provide insight into the overall crossflow entrainment since the majority of jet fluid is located out of the plane investigated here. Along with cross-sectional PIV, center-plane PIV should also be explored in this "extreme" near field view of the jet to provide more understanding of the velocity and vorticity fields, especially for the 40% turbulent intensity velocity profile, where jet fluid is ejected upstream into the crossflow periodically. Another potentially useful diagnostic would be high-speed laser Rayleigh scattering. With the current experimental set-up, an image taking frequency of 1Hz eliminates the connection of the observed temperature fields between images. By use of high-speed LRS, the formation and dissipation of some of the vortical structures observed here could potentially be characterized. Finally, as with any study, a different array of test cases, such as a wider band of momentum flux ratios and density ratios would also be useful in providing better trends and scaling of jet trajectories.

References

[1] R. J. Margason, "Fifty Years of Jet in Cross Flow Research," in *AGARD-CP-534*, Winchester, UK, 1993.

[2] T. F. Fric and A. Roshko, "Vortical Structure in the Wake of a Transverse Jet," *Journal of Fluid Mechanics,* vol. 279, pp. 1-47, 1994.

[3] S. Muppidi and K. Mahesh, "Study of Trajectories of Jets in Crossflow Using Direct Numerical Simulations," *Journal of Fluid Mechanics,* vol. 530, pp. 81-100, 2005.

[4] S. H. Smith and M. G. Mungal, "Mixing, structure and scaling of the jet in crossflow," *Journal of Fluid Mechanics,* vol. 357, pp. 83-122, 1998.

[5] L. Gevorkyan, "Structure and Mixing Characterization of Variable Density Transverse Jet Flows," Ph.D. Dissertation, Dept. of Mechanical and Aerospace Engineering, University of California, Los Angeles, CA, 2015.

[6] J. F. Keffer and W. D. Baines, "The Round Turbulent Jet in a Cross-Wind," *Journal of Fluid Mechanics,* vol. 15, no. 4, pp. 481-496, 1963.

[7] L. K. Su and M. G. Mungal, "Simultaneous Measurements of Scalar and Velocity Field Evolution in Turbulent Crossflowing Jets," *Journal of Fluid Mechanics,* vol. 513, pp. 1-45, 2004.

[8] L. Gevorkyan, T. Shoji, D. R. Getsinger, O. I. Smith and A. R. Karagozian, "Transverse jet mixing characteristics," *Journal of Fluid Mechanics,* vol. 790, pp. 237-274, 2016.

[9] S. Samuelson, "Rich Burn, Quick-Mix, Lean Burn (RQL) Combustor," in *The Gas Turbine Handbook,* National Energy Technology Laboratory, Retrieved 2018, pp. 227-233.

[10] J. A. Wagner, "Experimental Studies on Flow Field and Flame Stabilization of a Premixed Reacting Jet in Vitiated Crossflow," Ph.D. Dissertation, Dept. of Mechanical Engineering, University of Connecticut, Storrs, CT, 2016.

[11] D. A. Feikema, D. Everest and J. F. Driscoll, "Images of Dissipation Layers to Quantiy Mixing Within a Turbulent Jet," *AIAA Journal,* vol. 34, no. 12, pp. 2531-2538, 1996.

[12] R. S. Barlow and A. N. Karpetis, "Measurements of Scalar Variance, Scalar Dissipation, and Length Scales in Turbulent Piloted Methane/Air Jet Flames," *Flow, Turbulence and Combustion,* vol. 72, no. 2-4, pp. 427-448, 2004.

[13] R. J. Balla and J. L. Everhart, "Rayleigh Scattering Density Measruements, Clustor Theory, and Nucleation Calculations at Mach 10," *AIAA Journal,* vol. 50, no. 3, pp. 698-707, 2012.

[14] J. A. Sutton, "Mixture Fraction and Scalar Dissipation Rate Imaging in Turbulent Nonpremixed Flames Near Extinction," Ph.D. Dissertation, Dept. of Aerospace Engineering, University of Michigan, Ann Arbor, MI, 2005.

[15] C. M. Arndt, M. J. Papageorge, F. Fuest, J. A. Sutton, W. Meier and M. Aigner, "The Role of Temperature, Mixture Fraction, and Scalar Dissipation Rate on Transient Methane

Injection and Auto-Ignition in a Jet in Hot Coflow Burner," *Combustion and Flame,* vol. 167, pp. 60-71, 2016.

[16] R. L. Gordon, A. R. Masri and E. Mastorakos, "Simultaneous Rayleigh Temperature, OH- and CH2O-LIF Imaging of Methane Jets in a Vitiated Coflow," *Combustion and Flame,* vol. 155, pp. 181-195, 2008.

[17] R. B. Barat, J. P. Longwell, A. F. Sarofim, S. P. Smith and E. Bar-Ziv, "Laser Rayleigh Scattering for Flame Thermometry in a Toroidal Jet Stirred Combustor," *Applied optics,* vol. 30, no. 21, pp. 3003-3010, 1991.

[18] J. W. Strutt, 3rd Baron Rayleigh, *On the Light From the Sky, its Polarization and Colour*, M. R. Luo, Ed., Bedford, MA: Cambridge Research Laboratories, 1870, Reproduced in 1966.

[19] R. B. Miles, W. R. Lempert and J. N. Forkey, "Laser Rayleigh scattering," *Measurement Science and Technology,* vol. 12, pp. R33-R51, 2001.

[20] D. A. Long, *The Raman Effect: A Unified Treatment of the Theory of Raman Scattering by Molecules*, West Sussex, UK: John Wiley & Sons, 2002.

[21] N. Soulopoulos, Y. Hardalupas and A. M. K. P. Taylor, "Mixing and Scalar Dissipation Rate Statistics in a Starting Gas Jet," *Physics of Fluids,* vol. 27, no. 12, id.125103, 2015.

[22] N. Peters, *Turbulent Combustion*, Cambridge, UK: Cambridge University Press, 2000.

[23] G. K. Batchelor, "Small-Scale Variation of Convected Quantities Like Temperature in Turbulent Fluid Part 1. General Discussion and the Case of Small Conductivity," *Journal of Fluid Mechanics,* vol. 5, no. 1, pp. 113-133, 1959.

[24] W. M. Pitts, "Resolution Requirements for Scalar Dissipation Measurements in Turbulent Jets and Flames," in *Annual Meeting, 52nd. Proceedings. American Physical Society/Division of Fluid Dynamics,* New Orleans, LA, 1999.

[25] J. H. Bell and R. D. Mehta, "Contraction Design for Small Low-Speed Wind Tunnels," JIAA Report TR-84, Dept. of Aeronautics and Astronautics, Stanford University, Stanford, CA, 1988.

[26] S. G. Tuttle, "Blowoff Behavior of Bluff Body Stabilized Flames in Vitiated and Partially Premixed Flows," Ph.D. Dissertation, Dept. of Mechanical Engineering, University of Connecticut, Storrs, CT, 2010.

[27] D. G. Goodwin, H. K. Moffat and R. L. Speth, *CANTERA: An Object-Oriented Software Toolkit for Chemical Kinetics, Thermodynamics, and Transport Processes,* http://cantera.org, 2017. Version 2.3.0. doi:10.5281/zenodo.170284Cantera.

[28] H. Wang, X. You, A. V. Joshi, S. G. Davis, A. Laskin, F. Egolfopoulos and C. K. Law, *USC Mech Version II. High-Temperature Combustion Reaction Model of H2/CO/C1-C4 Compounds,* 2007.

[29] L. A. El-Gabry, D. R. Thurman and P. E. Poinsatte, "Procedure for Determining Turbulence Length Scales Using Hotwire Anemometry," NASA, Cleveland, OH, 2014.

[30] J. A. Sutton and J. F. Driscoll, "Rayleigh Scattering Cross Sections of Combustion Species at 266, 355, and 532 nm for Thermometry Applications," *Optics Letters,* vol. 29, no. 22, pp. 2620-2622, 2004.

[31] W. C. Gardiner Jr., Y. Hidaka and T. Tanzawa, "Refractivity of Combustion Gases," *Combustion and Flame,* vol. 40, pp. 213-219, 1981.

[32] M. P. Bogaard, A. D. Buckingham, R. K. Pierens and A. H. White, "Rayleigh Scattering Depolarization Ratio and Molecular Polarizability Anistropy for Gases," *Journal of the Chemical Society, Faraday Transactions 1,* vol. 74, no. 0, pp. 3008-3015, 1978.

[33] J. D'Errico, "inpaint_nans," MATLAB Central File Exchange, 2012. [Online]. [Accessed 11 November 2017].

[34] C. Tomasi and R. Manduchi, "Bilateral Filtering for Fray and Color Images," in *Sixth International Conference on Computer Vision (IEEE Cat. No.98CH36271)*, Bombay, 1998.

[35] S. Megerian, J. Davitian, L. S. d. B. Alves and A. R. Karagozian, "Transverse-Jet Shear-Layer Instabilities. Part 1. Experimental Studies," *Journal of Fluid Mechanics,* vol. 593, pp. 93-129, 2007.

[36] G. L. Brown and A. Roshko, "On Density Effects and Large Structure in Turbulent Mixing Layers," *Journal of Fluid Mechanics,* Vols. 64, Part 4, pp. 775-816, 1974.

Appendix

The following instantaneous temperature fields were chosen at random instances in time from each data set. These are intended to provide visualization of the differences in the flow field dynamics for each test case in an effort to aid in the understanding of the differences in the average temperature fields shown in Sect. 5.1. Table A.1 is a list of all test cases performed and the corresponding figure number of instantaneous images.

Table A.1: List of test cases and corresponding instantaneous images figure number.

J	*s*	Velocity Profile	Fig. #	Page #
7.0	5.32	Pipe	Fig. 0.1	78
12.6	5.32	Pipe	Fig. 0.2	79
18.0	5.32	Pipe	Fig. 0.3	80
7.0	3.19	Pipe	Fig. 0.4	81
12.6	3.19	Pipe	Fig. 0.5	82
7.0	5.32	Top-Hat	Fig. 0.6	83
12.6	5.32	Top-Hat	Fig. 0.7	84
18.0	5.32	Top-Hat	Fig. 0.8	85
7.0	3.19	Top-Hat	Fig. 0.9	86
12.6	3.19	Top-Hat	Fig. 0.10	87
7.0	5.32	40% TI	Fig. 0.11	88
12.6	5.32	40% TI	Fig. 0.12	89
18.0	5.32	40% TI	Fig. 0.13	90
7.0	3.19	40% TI	Fig. 0.14	91
12.6	3.19	40% TI	Fig. 0.15	92

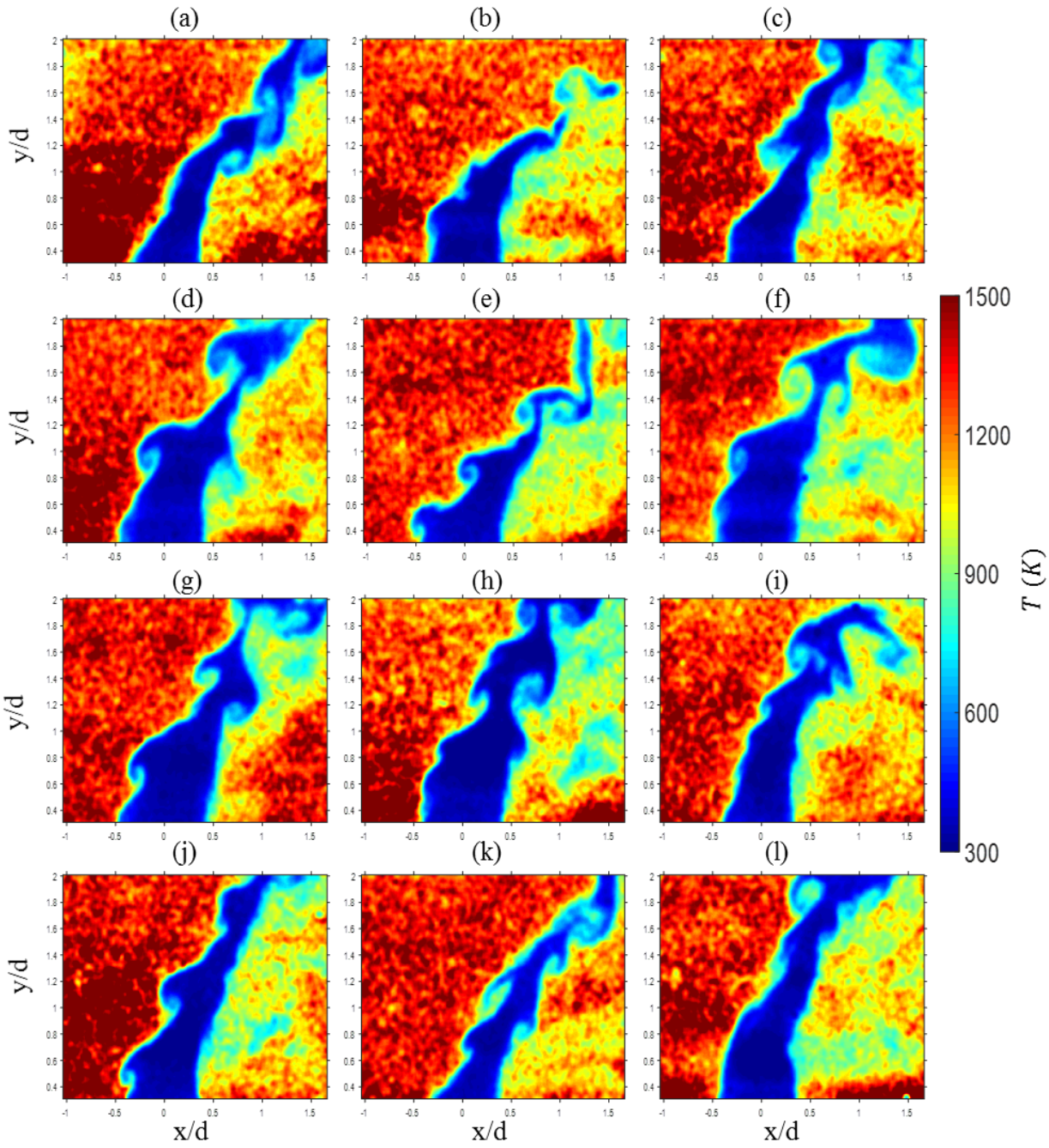

Fig. 0.1: Instantaneous temperature fields chosen at random instances in time for the turbulent pipe jet velocity profile with momentum flux ratio J = 7.0 and density ratio s = 5.32.

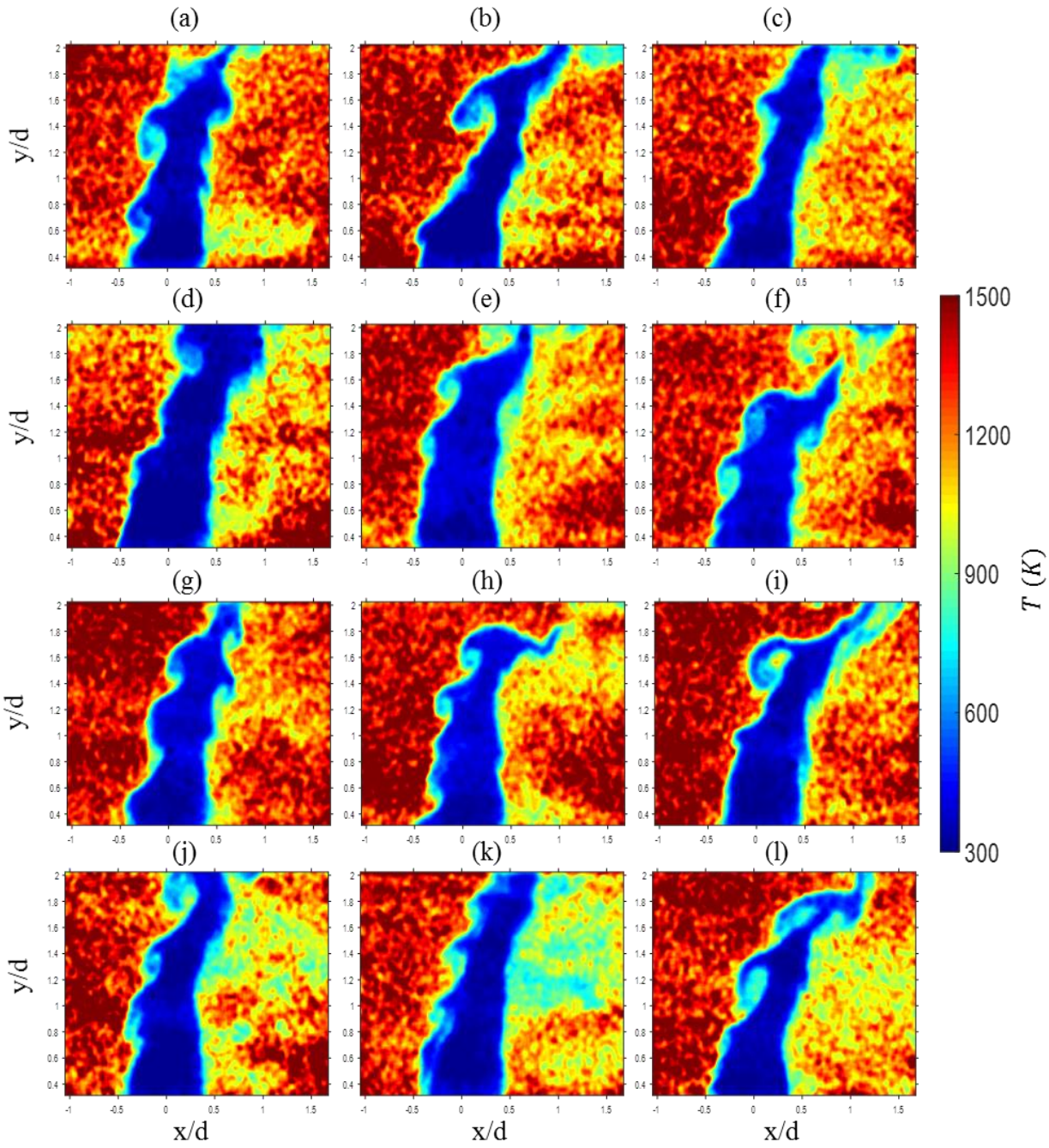

Fig. 0.2: Instantaneous temperature fields chosen at random instances in time for the turbulent pipe jet velocity profile with momentum flux ratio J = 12.6 and density ratio s = 5.32.

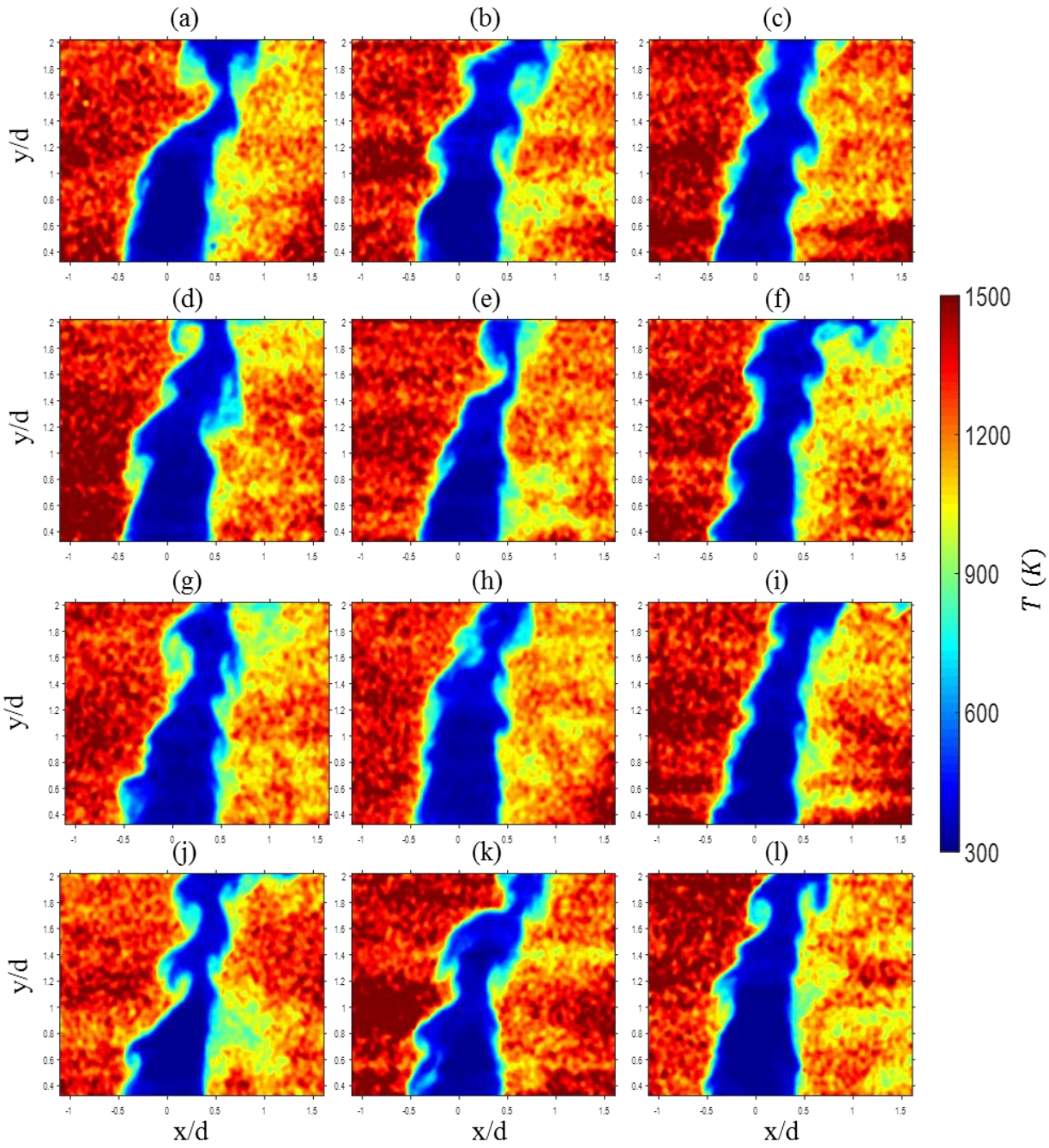

Fig. 0.3: Instantaneous temperature fields chosen at random instances in time for the turbulent pipe jet velocity profile with momentum flux ratio J = 18.0 and density ratio s = 5.32.

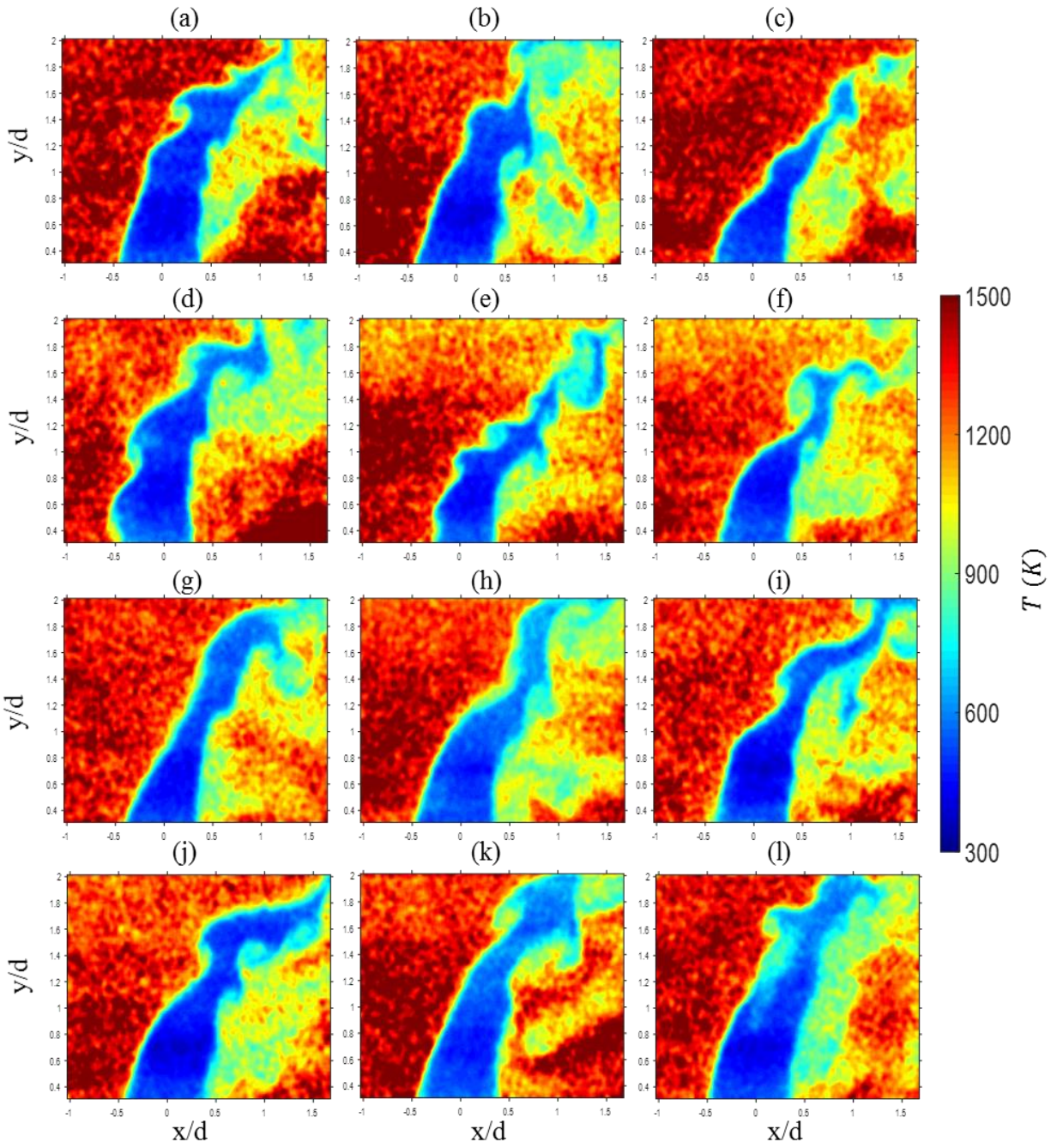

Fig. 0.4: Instantaneous temperature fields chosen at random instances in time for the turbulent pipe jet velocity profile with momentum flux ratio J = 7.0 and density ratio s = 3.19.

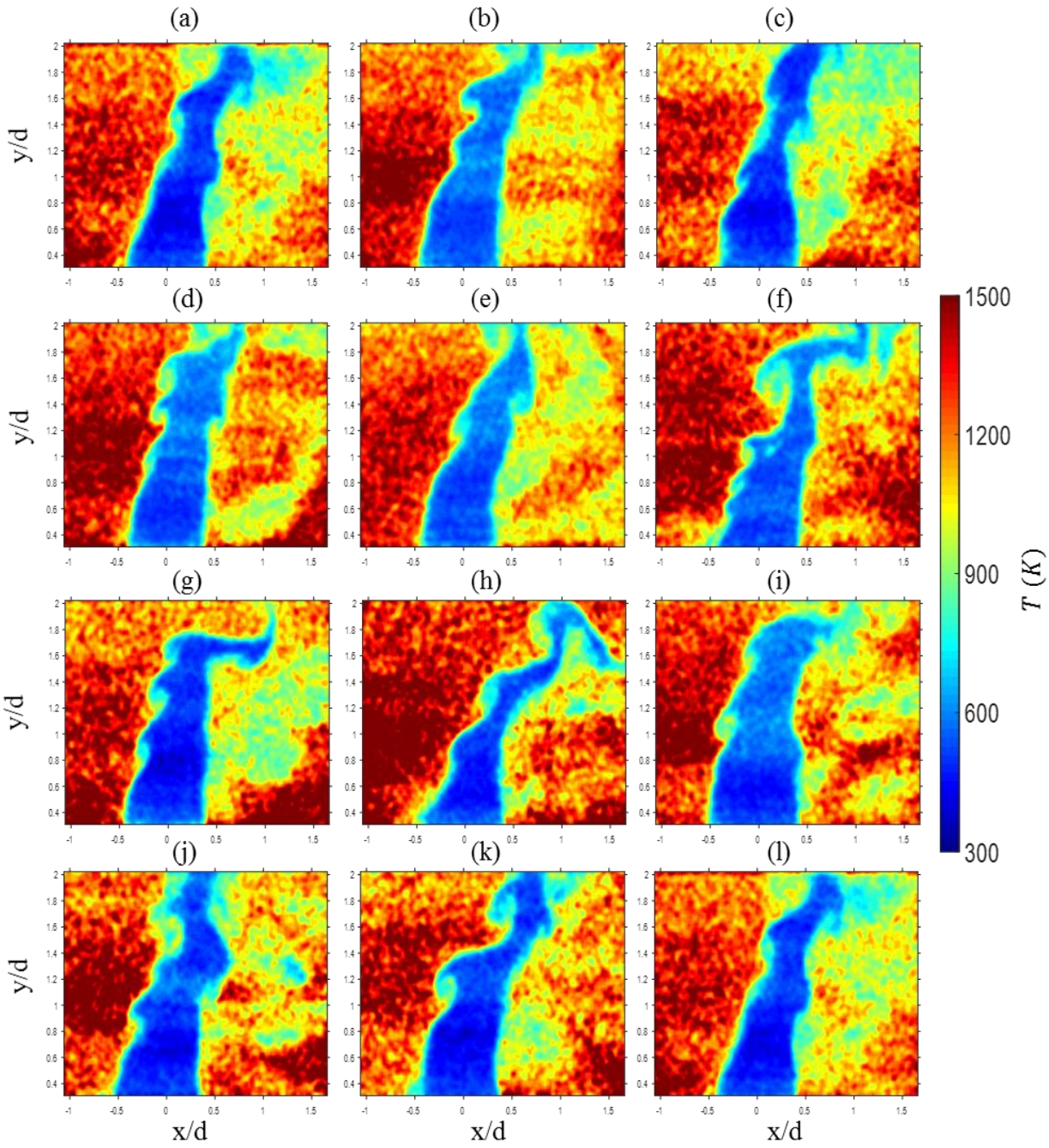

Fig. 0.5: Instantaneous temperature fields chosen at random instances in time for the turbulent pipe jet velocity profile with momentum flux ratio J = 12.6 and density ratio s = 3.19.

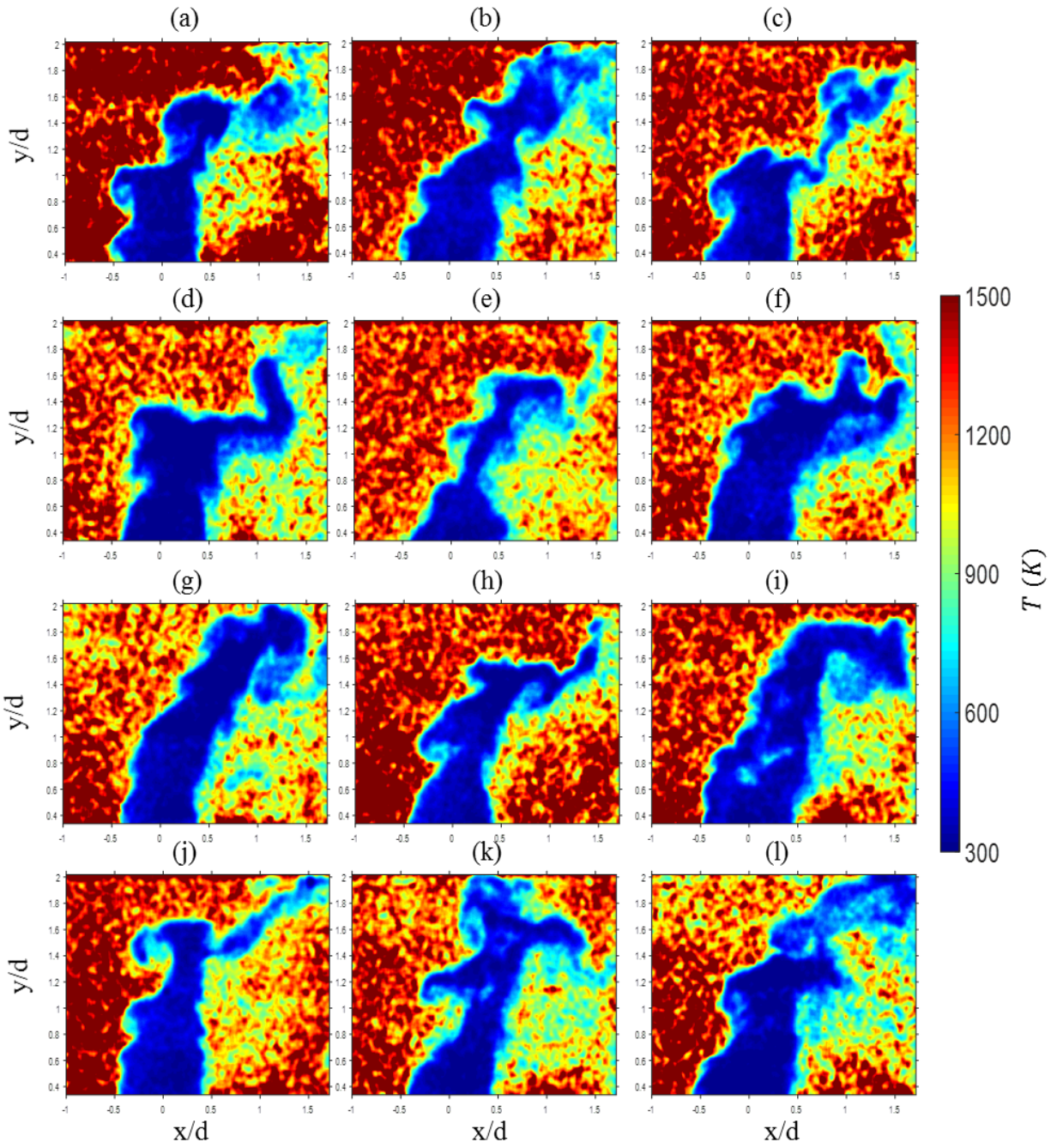

Fig. 0.6: Instantaneous temperature fields chosen at random instances in time for the top-hat jet velocity profile with momentum flux ratio J = 7.0 and density ratio s = 5.32.

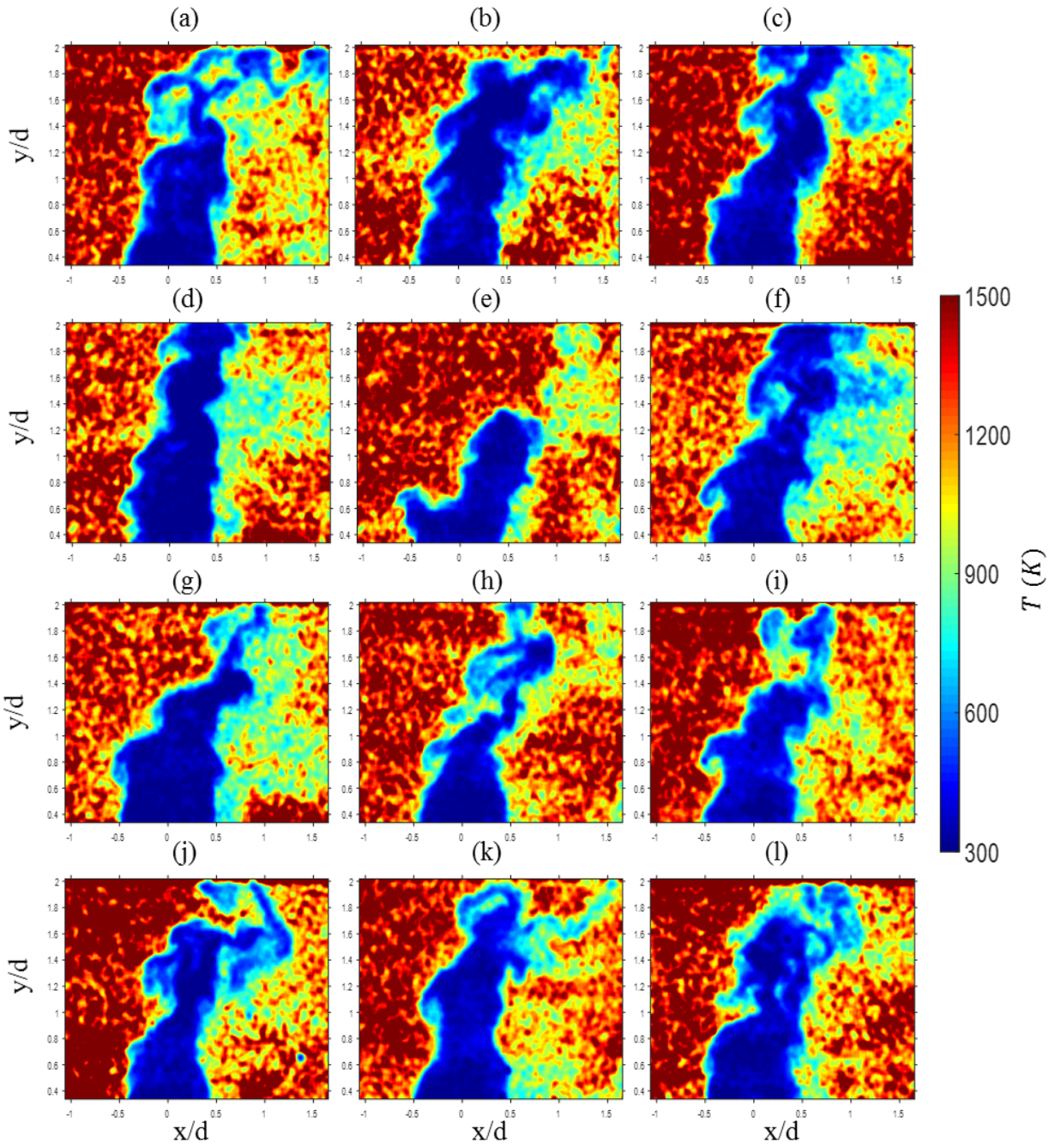

Fig. 0.7: Instantaneous temperature fields chosen at random instances in time for the top-hat jet velocity profile with momentum flux ratio J = 12.6 and density ratio s = 5.32.

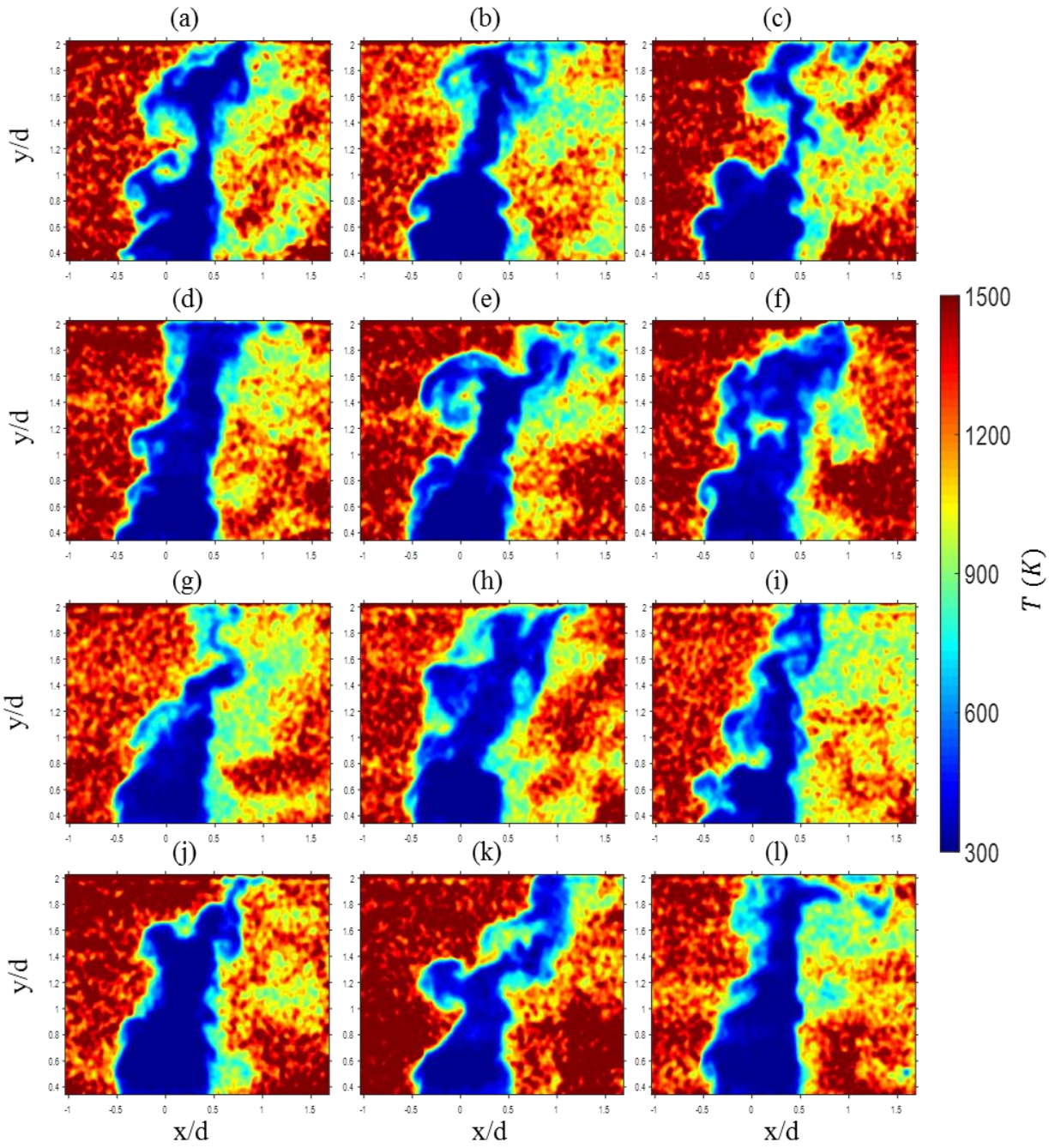

Fig. 0.8: Instantaneous temperature fields chosen at random instances in time for the top-hat jet velocity profile with momentum flux ratio J = 18.0 and density ratio s = 5.32.

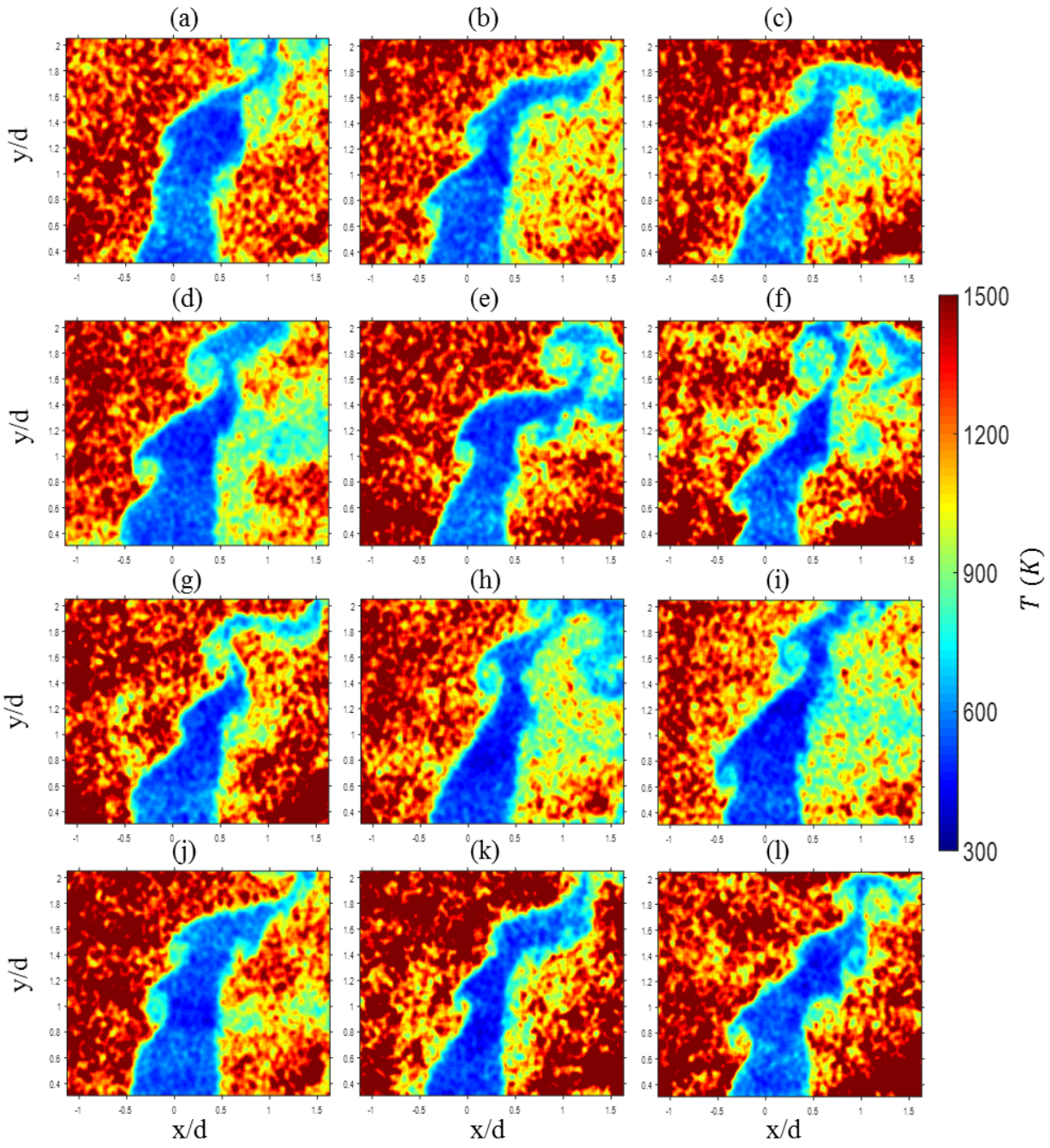

Fig. 0.9: Instantaneous temperature fields chosen at random instances in time for the top-hat jet velocity profile with momentum flux ratio J = 7.0 and density ratio s = 3.19.

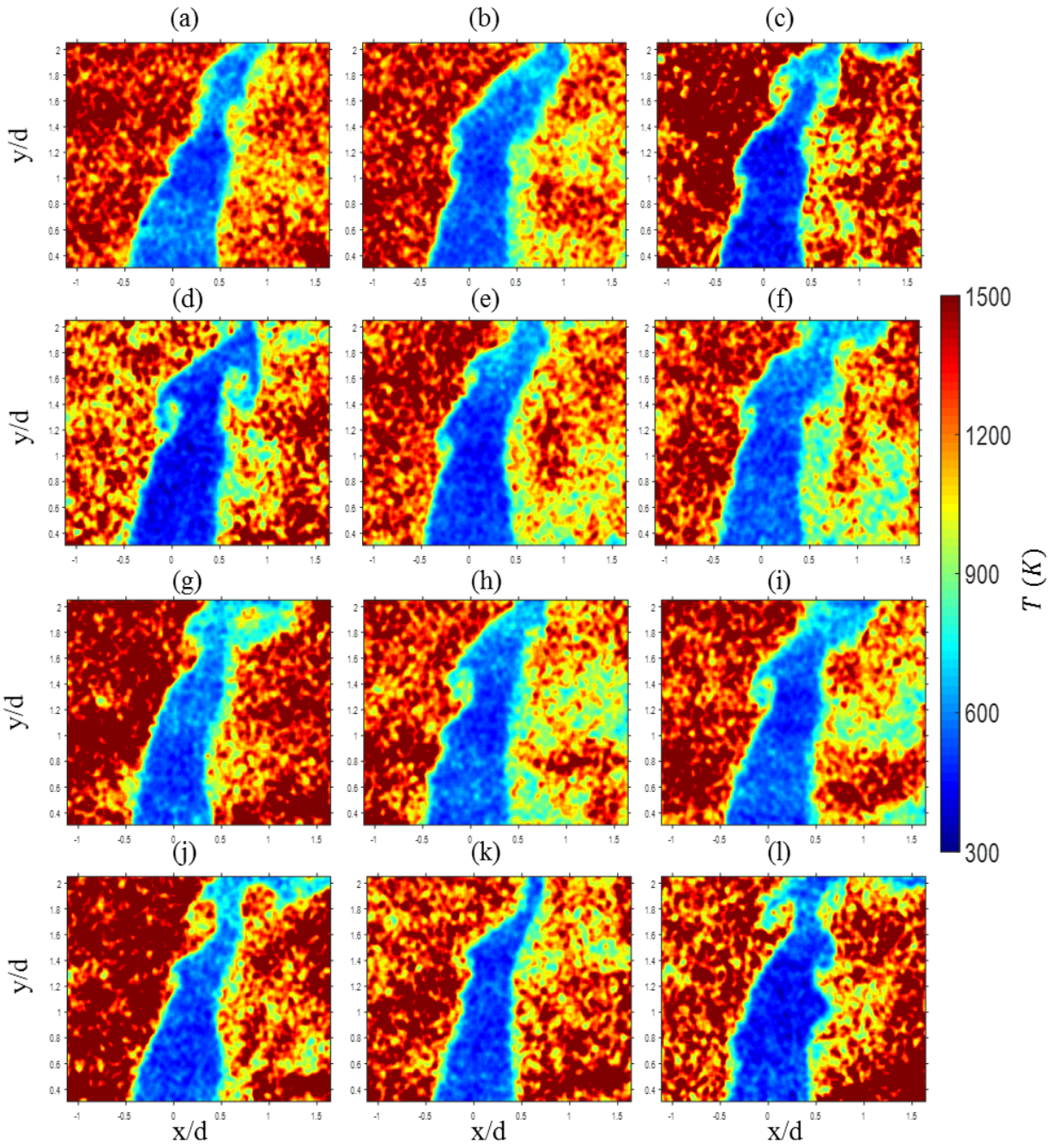

Fig. 0.10: Instantaneous temperature fields chosen at random instances in time for the top-hat jet velocity profile with momentum flux ratio J = 12.6 and density ratio s = 3.19.

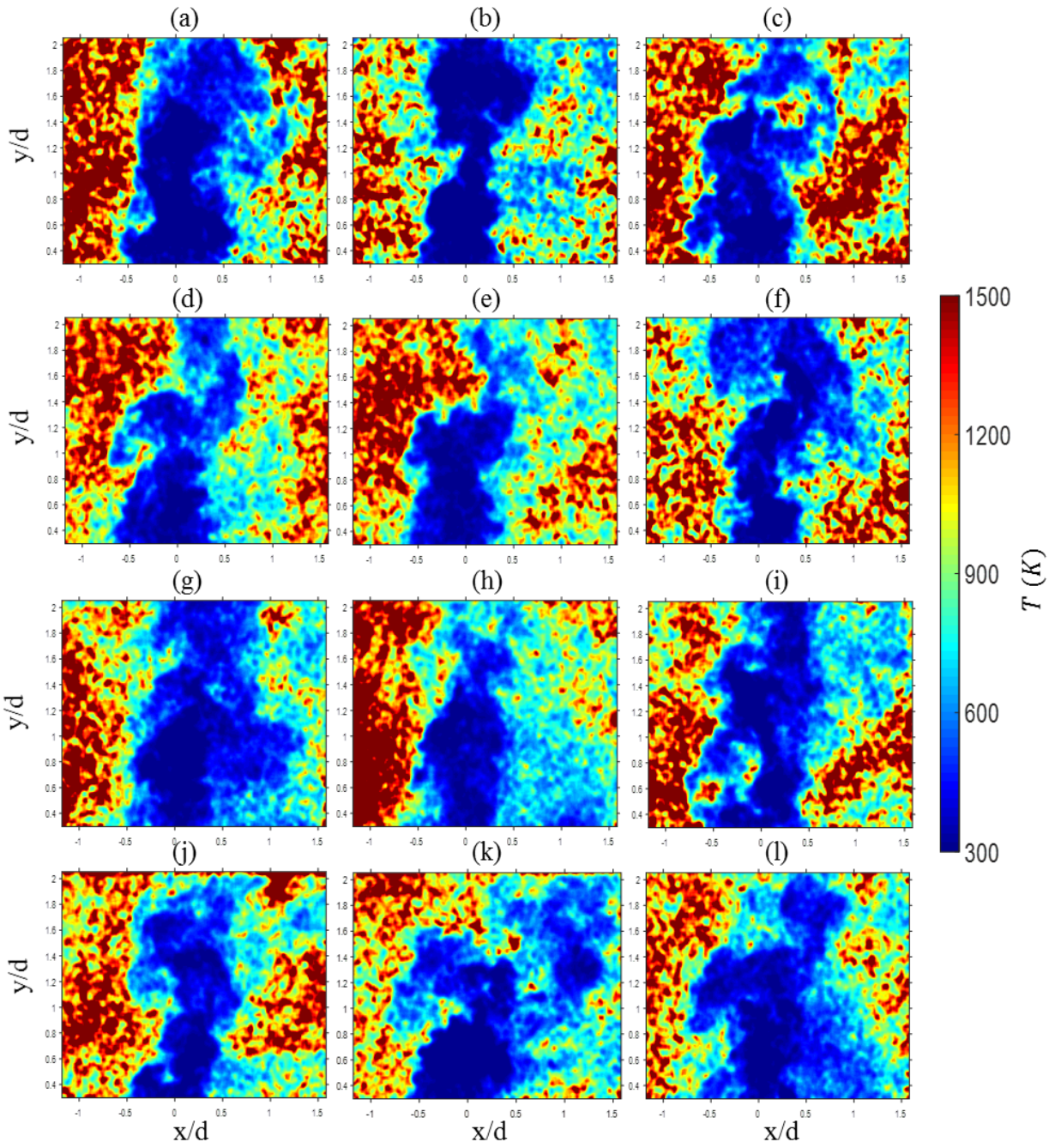

Fig. 0.11: Instantaneous temperature fields chosen at random instances in time for the 40% turbulence intensity jet velocity profile with momentum flux ratio J = 7.0 and density ratio s = 5.32.

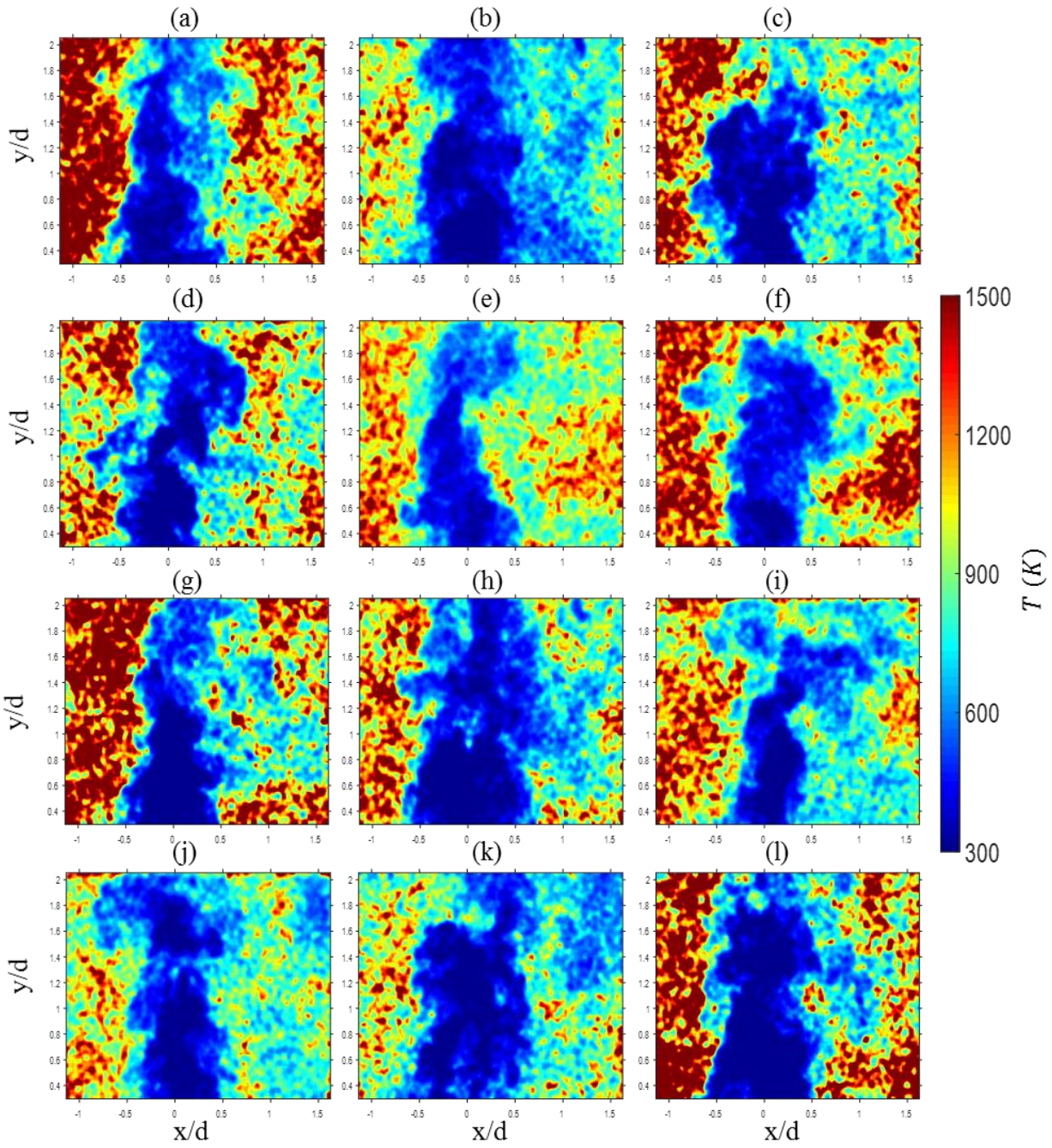

Fig. 0.12: Instantaneous temperature fields chosen at random instances in time for the 40% turbulence intensity jet velocity profile with momentum flux ratio J = 12.6 and density ratio s = 5.32.

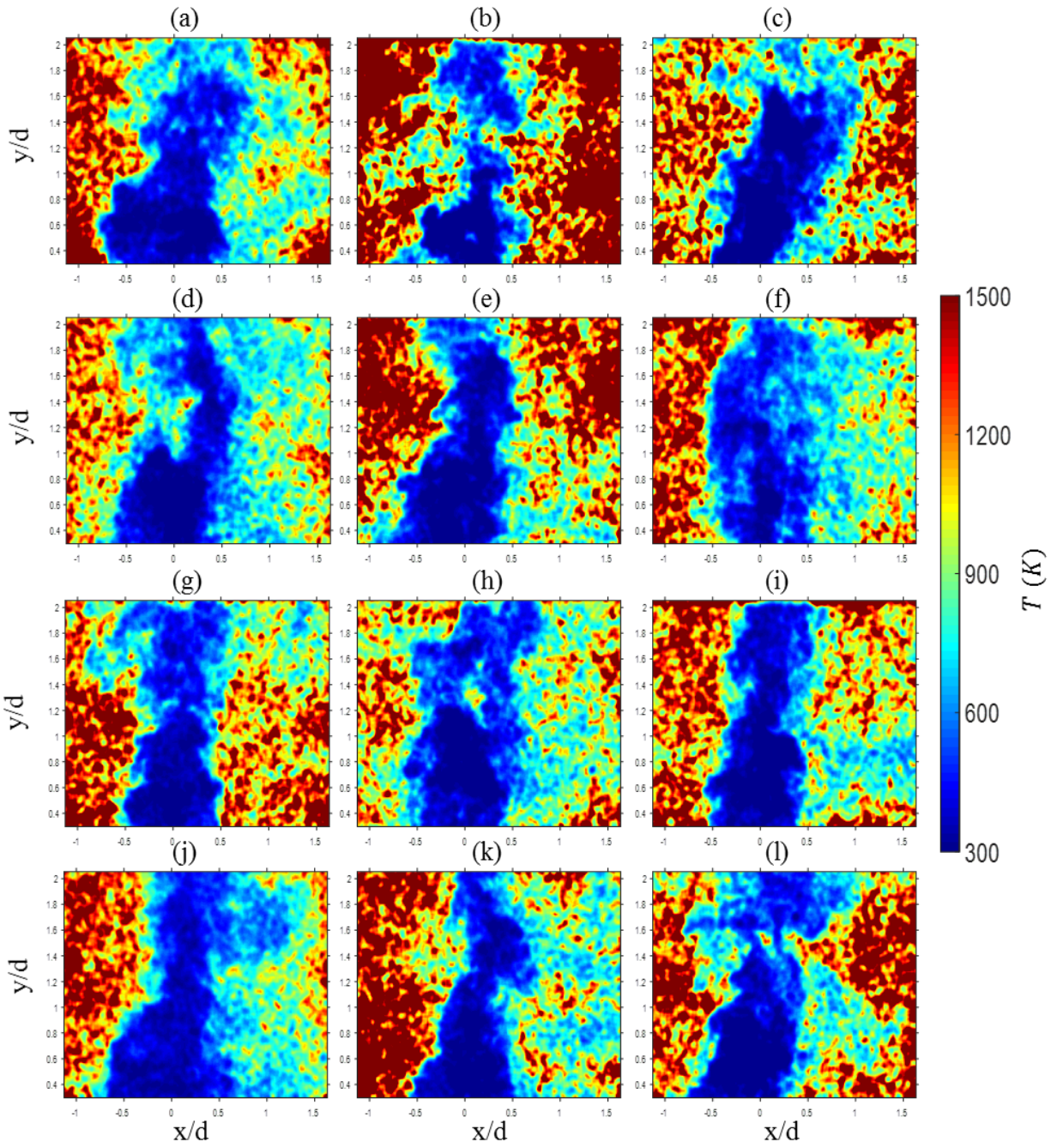

Fig. 0.13: Instantaneous temperature fields chosen at random instances in time for the 40% turbulence intensity jet velocity profile with momentum flux ratio J = 18.0 and density ratio s = 5.32.

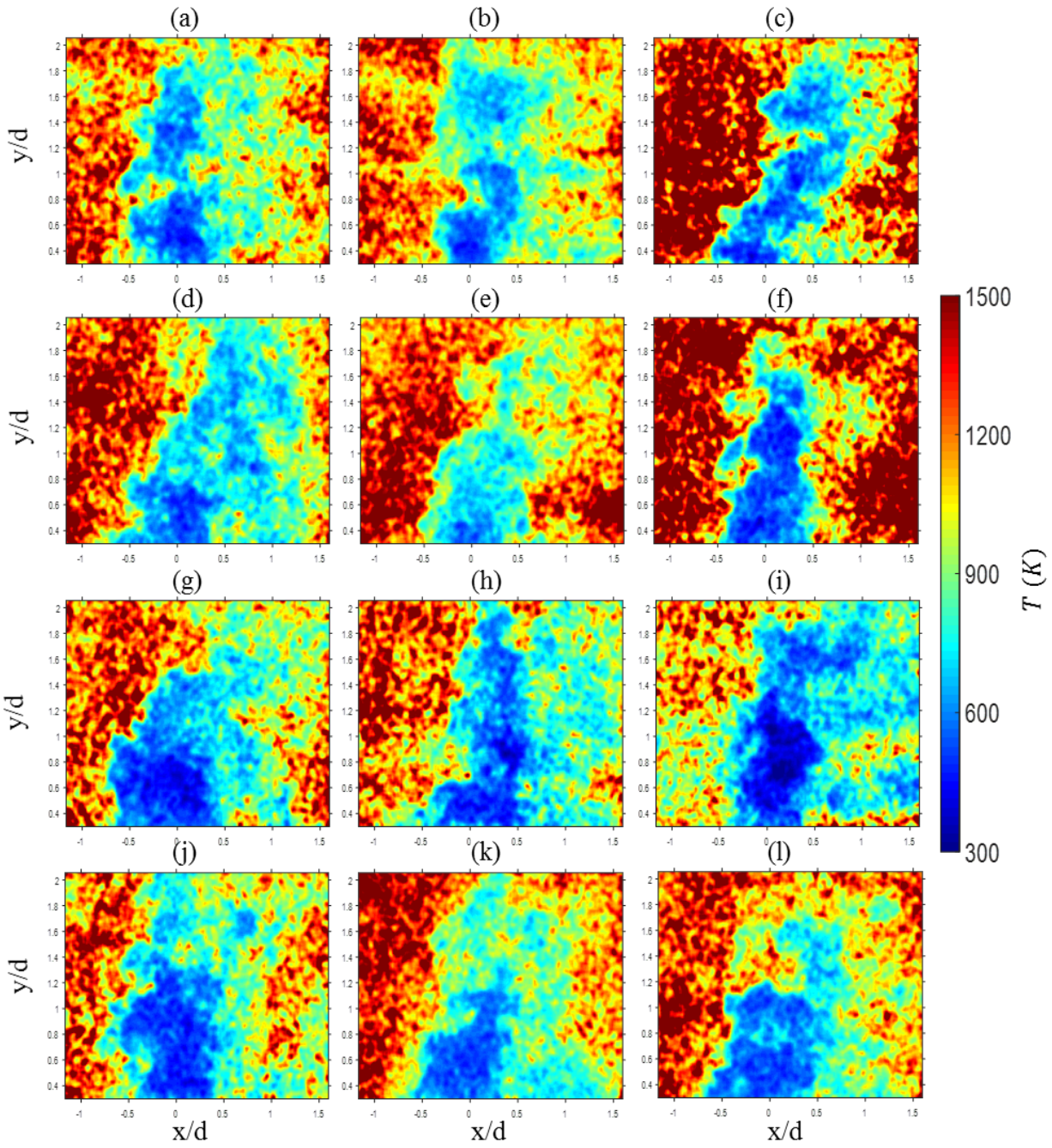

Fig. 0.14: Instantaneous temperature fields chosen at random instances in time for the 40% turbulence intensity jet velocity profile with momentum flux ratio J = 7.0 and density ratio s = 3.19.

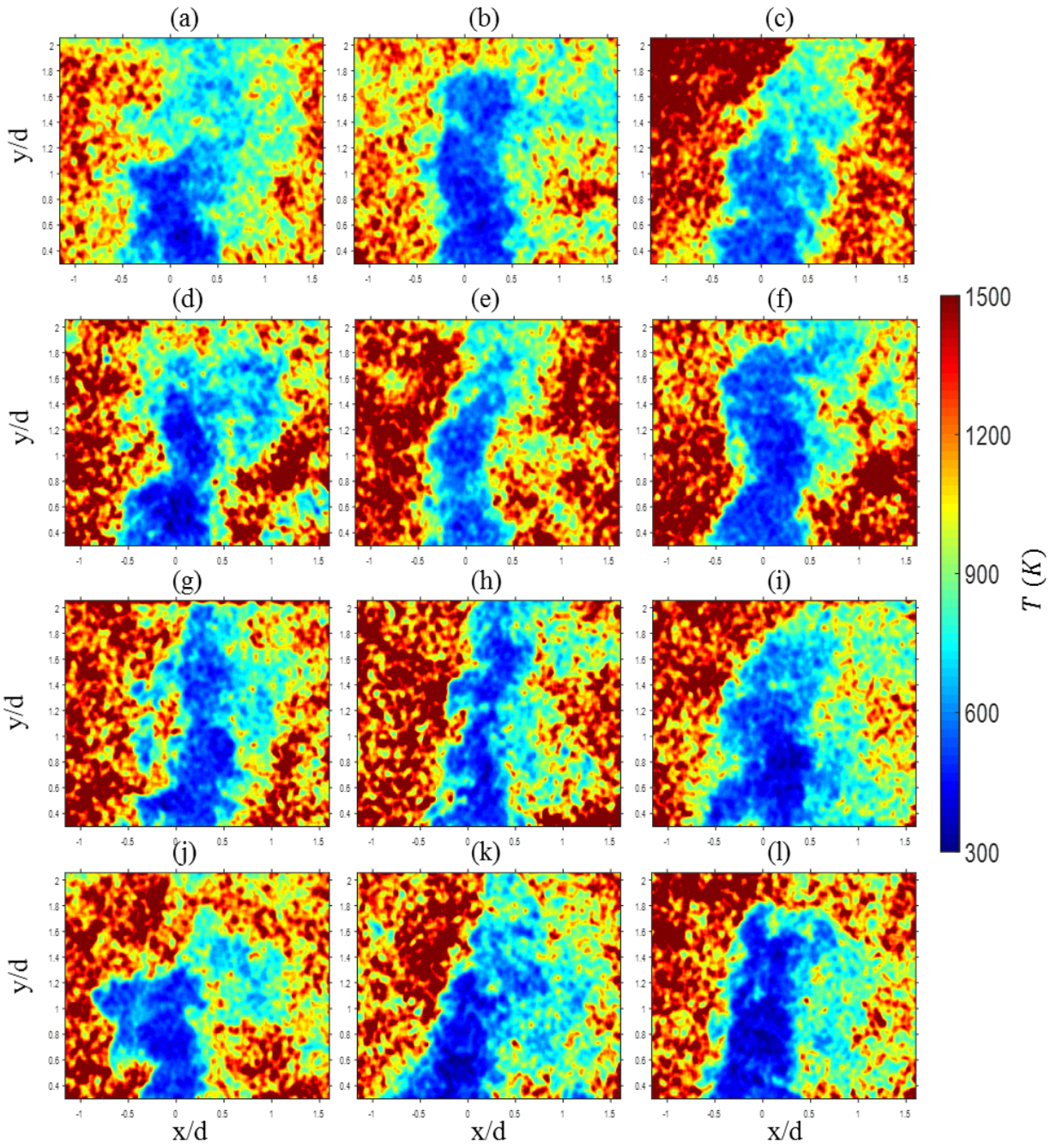

Fig. 0.15: Instantaneous temperature fields chosen at random instances in time for the 40% turbulence intensity jet velocity profile with momentum flux ratio J = 12.6 and density ratio s = 3.19.